NASA Contractor Report 4437

A Study of Aluminum-Lithium Alloy Solidification Using Acoustic Emission Techniques

Daniel P. Henkel
Lehigh University
Bethlehem, Pennsylvania

Prepared for
Langley Research Center
under Grant NGT-50417

National Aeronautics and
Space Administration

Office of Management

Scientific and Technical
Information Program

1992

Acknowledgements

I would like to express my gratitude to my advisor, Dr. John D. Wood, for his support during the course of this work. His patience, especially at the beginning of the program, helped to transform a production-oriented engineer into a research-oriented scientist. Special thanks are also due to Dr. William Prosser of NASA Langley Research Center and to Dr. Adrian Pollock of Physical Acoustics Corporation for their limitless assistance in many technical and personal aspects of this program. The interest and suggestions of the remainder of my committee: Provost Alan Pense, Dr. John Ochs, and Dr. David B. Williams, have been indispensable and are truly appreciated.

During the course of my graduate program I have had the good fortune to be associated with many fine people. Among those, I would like to extend special thanks to: Dr. John Fisher, Dr. Joseph Heyman, Dr. Douglas Granger, and Dr. Eric Kaufmann for sharing their expertise and providing many useful suggestions. Also, special thanks are due to Bill and Karen Prosser for their hospitality during my visits to Langley.

The support of my family throughout this midlife "crisis" requires more than just thanks and can never be fully repaid. Above all, the professional and personal sacrifices of my wife, Julie, have been the most important ingredients for the successful completion of my graduate studies. Her drive kept me moving at a steady pace, her understanding showed me the importance of optimism, and her altruistic support was often the decisive catalyst to finish. We have worked equally hard on this project and the rewards should be equally shared.

Grateful acknowledgement is given to the following organizations that made this dissertation possible: The Alcoa Technical Center for supplying materials; Physical Acoustics Corporation, NASA Langley, and Lehigh University's NSF supported ERC for Advanced Technology Center of Large Structural Systems (ATLSS) and the Department of Materials Science and Engineering for providing equipment. A special word of thanks is due to ATLSS and the Graduate Students Research Program (GSRP) of NASA Langley Research Center for providing financial support.

Table of Contents

List of Figures

List of Tables

List of Nomenclature

AE - acoustic emission

Al-Li - aluminum lithium

δ - Al_3Li phase

δ'- AlLi cubic phase

BN - boron nitride

CA-DTA - computer-aided differential thermal analysis

C_E - composition of eutectic

C_L - composition of liquid

C_o - initial composition

C_P - specific heat

C_s - composition of solid

D.S.O. - digital storage oscilloscope

Db - decibel

DIC- differential interference contrast

EMI - electromagnetic interference

f - frequency (Hz)

f_E - fraction of eutectic

FFT - fast Fourier transform

f_s - fraction of solid

GPa - gigapascals

HDT - hit definition time (ms)

k - equilibrium partition ratio

L - length of rod (m)

L' - latent heat of solidification at time, t

LC - inductive-capacitive

LiH - lithium hydride

L_{TOTAL} - total latent heat of solidification

MARSE - measured area under the rectified signal envelope

MPa - megapascals

n - wave number

NDE - non-destructive evaluation

p-wave - longitudinal mode acoustic wave

PAC - Physical Acoustics Corporation

ppm - parts per million

S-T - short transverse rolling direction

SCC - stress corrosion cracking

STP - standard temperature and pressure

α_{ss} - supersaturated solid solution of phase

t - time (seconds)

T_1 - Al_2CuLi hexagonal phase

TC - thermocouple

T_E - equilibrium temperature

TiB - Al-10w%Ti-0.4w%B alloy grain refiner

T_M - melting temperature

T_N - undercooling temperature

UHP- ultra-high purity

v - velocity of solidification front (m/s)

Abstract

Physical phenomena associated with the solidification of an aluminum-lithium alloy, an aluminum-copper alloy, and ultra-pure aluminum have been characterized using acoustic emission (AE) techniques. This study has shown that repeatable patterns of AE activity may be correlated to microstructural changes that occur during solidification.

The acoustic emission approach is based on the measurement of strain energy that is released as a material transforms from a liquid to a solid. If the source moves rapidly enough, stress waves will be generated with sufficient energy to reach a free surface of the specimen and develop detectable vibrations. A transducer coupled to this surface converts the displacements of the vibrations to voltage signals which may be amplified, filtered, or stored for post-acquisition processing. These signals have been analyzed to relate periods AE activity to the fraction of solid, or stage of solidification.

The influence of the experimental system on generated signals has been examined in detail. Time and frequency domain analysis of the response of a boron nitride waveguide materials and three transducers has been performed. The analysis has been used to show how an AE signal from a solidifying metal is changed by each component of the detection system to produce a complex waveform.

Acoustic emission during solidification has been studied using two methods: conventional and individual waveform analysis. Conventional analysis has shown that a period of high AE activity occurs in ultra-pure aluminum, an Al-Cu alloy and an Al-Li alloy as the last fraction of solid forms. A model is presented which attributes this activity to internal stresses caused by grain boundary formation. Another period of AE activity occurs in the two alloys as the first fraction of solid forms. This activity was not

observed in the non-porous ultra-pure aluminum. A model is presented which attributes this activity to interdendritic porosity. A mixture of low and high intensity signals occurred during each period but specific trends in waveform characteristics were not identified. The waveform is dominated by resonant effects from the waveguide or, if high-pass filtering is used, the transfer function of the transducer controls the waveshape.

I. Introduction

Material scientists are as interested in developing new methods of evaluating material properties as they are in developing new materials. One relatively new method of evaluation, approximately forty years old, which has been receiving substantial research interest is acoustic emission (AE). A new class of metals which has also evolved over this same time period is aluminum-lithium (Al-Li) alloys. The popularity of both topics has gone through simultaneous peaks in the early 1960's and 70's and troughs towards the end of those same decades. The current consensus is that a conservative approach is required to identify specific applications for each with the understanding that neither is an absolute replacement for conventional methods or materials.

Acoustic emission has a combination of features which no other materials evaluation method can provide. Its range of detection extends from the movement of microscopic dislocations in metals to the movement of massive platelets below the earth's surface. Applications as diverse as railroad car proof-testing and magnetic transformation detection are commonly practiced. AE can also detect, in real-time, the formation of a defect and locate its position. One major research effort has been source characterization or the ability to distinguish one type of defect from another by their acoustic emission signals. However, to date, removing effects of signal convolution during its propagation to a detector has been an unsolvable problem except in simple laboratory experiments. Many believe that the full potential of AE will only be realized when this inherent problem is overcome and defects can be identified as well as located by their AE signals. In addition

to acoustic emission, which is itself an interesting topic, the present research investigates the solidification of Al-Li alloys, another field attracting attention today.

Aluminum-lithium alloys offer lower density and higher modulus than conventional aluminum alloys. Demands from the aerospace industry for improved damage tolerant, weight efficient structures have been the incentive for their development. The major technical problems confronting the producers have been: (1) porosity during primary processing and (2) low toughness and stress corrosion cracking resistance in the finished product. As with acoustic emission, the full potential of Al-Li alloys cannot be achieved until such inherent problems have been resolved.

This study evaluates the solidification of Al-Li alloys using acoustic emission technology. Emphasis has been placed on the mechanisms of solidification, defect development during solidification, and the characterization of those defects using acoustic emission. One strategic initiative was improvement of aluminum-lithium solidification technology by providing an understanding of defect formation and real-time detection. Another was the evaluation of AE source characterization techniques that could distinguish sources generated during Al-Li solidification. Through comparisons of material microstructures and acoustic emission data, two sources of AE have been distinguished. The knowledge base of evaluation methods to reduce casting defects in metal has thereby been broadened by this study.

II. Background

2.1 Acoustic Emission

2.1.1 History

Earthquakes, magnetic transformations, and micro-fracture in metals have at least one thing in common - they generate acoustic emission. Although on much different scales, all of the above mechanisms radiate energy in the form of elastic waves as a result of applied stress.

Acoustic emission history has been arbitrarily divided into four general periods [1]. The "Tin-Cry" period, beginning around the turn of this century, included investigations in which audible sounds were reported as observations during experiments on metals. An example is Czochralski's work which found an association between twinning of tin or zinc and the simultaneous sound emitted which has been termed "cry" [2].

The second period or "Age of Discovery" involved major research efforts to understand the acoustic emission phenomenon. The first instrumented experiment, conducted in Germany, was published in 1936 by Forster and Schiel [3]. They recorded noises caused by martensitic transformation in 29% Ni-steel. Joseph Kaiser's doctoral thesis [4] is considered the first comprehensive investigation specifically on acoustic vibrations originating from within stressed polycrystalline metals. The phenomenon was termed acoustic emission (AE) since the stress waves came from within the material in response a release of strain energy. Although Kaiser's first paper examined polycrystalline aluminum, some of his later research involved studies of AE during solidification in metal alloys such as Sn-Bi [5].

Many definitions of AE have since been formulated. The following is a generalized definition developed by the author that takes into account theories and models brought forth in the course of this research:

Acoustic emission is a transient elastic wave or set of waves generated by a rapid release of energy from localized sources within a material.

The description specifically excludes the limiting terms solid, metal, strain, and non-destructive which are used in the traditional definitions. The reasons will be explained throughout this paper. The term acoustic emission is also applied to the evaluation method used to detect and analyze the elastic waves.

The level of sound associated with the emission process is very low, being at least an order of magnitude smaller than that produced by the stroking of a specimen with the end of a frayed cotton thread [6]. In the present study it was necessary to amplify the signals 90 Db (100,000x) for reliable data acquisition. Although AE has been observed and recorded for almost forty years, no unified explanation of its source mechanisms has been achieved. Only in the simplest cases of point sources in infinite and thick plates has a complete analytical description of the stress waves in the vicinity of the source been made [7].

In 1960, Tatro [8] listed several reasons for studying acoustic emission:
(1) the phenomenon exists, (2) it is subject to measurement, (3) it is related to structure-sensitive properties of materials about which there is well-established information, (4) it may develop into a direct NDE method for structure-sensitive properties, (5) science will develop faster by probing new methods than by continuing to use only the established

methods. Thirty years may have passed but these reasons, particularly the third, could again be used as the incentive to study solidification in aluminum and its alloys by the acoustic emission method.

Reviews have been well documented for many AE topics including source characteristics [9], signal processing [10], instrumentation [11], history [12], and applications [13]. From an acoustic emission perspective, the present dissertation is mainly concerned with the characteristics of acoustic signals generated by solidification and how these signals may be processed after their waveforms and frequency spectra have been altered by the detection system.

Sources of acoustic emission during the solidification of aluminum have been proposed by others. Feurer and Wunderlin [14] showed that, as the fraction of porosity increases from the release of supersaturated hydrogen in solidifying Al-4.5%Cu-0.2%Ti aluminum, the AE activity increases proportionally. Their experiments, however, were not atmosphere-controlled and did not take into consideration oxidation, gas absorption, thermal cooling rates, micro-cracking, crucible friction or grain size. The only source of AE was assumed to be pore formation and the only analyzed parameter was the cumulative number of AE events.

They also discussed two stages of acoustic emission activity during solidification. The first, at the beginning of solidification, was attributed to smaller pores forming between dendrite arms and the second, at the end of solidification, to larger pores in the liquid between dendrites. A similar two stage pattern was observed in Al-Li and Al-Cu alloys during the present study. A model is proposed for this behavior and will be

compared with Feurer and Wunderlin's model in Sections IV and V, Results and Discussion.

Kumar and Prabhakar [15] examined the acoustic emission during the casting of Al-11.6% Si and Al-4.0% Cu alloys. The copper-containing alloy had a tendency for hot tearing, the silicon-containing alloy did not. Their efforts were concentrated on the embedded waveguide that was designed to maintain contact after the melt solidifies. They concluded from plots of cumulative AE events versus amplitude that a different pattern exists when hot tearing is present. However, they did not give an explanation other than the Al-11.6%Si alloy had a higher AE energy than the Al-4.0%Cu alloy.

Sharma, et al.[16] induced hot tearing in three aluminum alloys (commercial purity aluminum, Al-3.0%Cu, and Al-4.0%Cu) by using increasing degrees of specimen restraint. Their results indicated that the total acoustic energy increases as a visible tear develops in the final stages of solidification. They concluded that AE signals arise from hot tearing but conceded that AE signals are also detected in castings without visible tears. They suggested this is due to breaking of contacts between dendrites which are subsequently healed by the surrounding liquid. In castings solidified under no restraint, a certain level of AE was also observed. Their explanation was that it is probably due to the formation of pores as observed by Feurer and Wunderlin. In the present study AE was recorded from castings that were neither restrained nor porous.

A much different model by Xiufang, et al.[17] proposes grain formation as an acoustic emission source. Using the transparent organic compound maleic anhydride ($C_4H_2O_3$) they observed AE signals corresponding to its nucleation and growth during

solidification. They state that if the grain structure is equiaxed, then the number of grains is directly proportional to the number of AE signals per unit time, the count rate. No bubbles or hot tears were seen during the solidification period and signals from such sources were discounted. Their second experiment with an eutectic Al-Si alloy demonstrated an increase in the AE count rate during the primary stage of solidification as the number of grains in the primary stage increased.

The Xiufang model of acoustic emission, generated by nucleation, begins by addressing the change from atomic short range to long range order as a process of energy liberation. The release of latent heat of crystallization is one form. Acoustic emission is another which, they wrote, "results from a variation in the speed of various parts of interior matter causing a wave". They are implying that the growing solid nuclei generate waves in the surrounding liquid which are detected at the surface as AE signals. They concluded that the greater the number of nuclei, the stronger the acoustic emission signal. AE was also observed during the dendritic growth period in the form of weaker continuous signals.

2.1.2 AE - The NDE Method

2.1.2a General

Acoustic emission, in addition to a physical phenomenon, is also a term applied to a relatively new nondestructive evaluation (NDE) technique. While looked upon as an interesting subject for almost twenty years, its usage was limited by instrumentation speed and sensitivity until the late 1970's [18]. Today, however, it is gaining acceptance as an important materials evaluation method with features shared by no other technique.

AE is a passive technique that uniquely depends on the material to produce its own stress wave sources. It may be used to continuously monitor a material and may do so globally or within a limited zone. Applications are diverse. They have included fracture analysis [19], corrosion monitoring [20], deformation studies [21], machinery diagnostics [22], geotechnical applications [23], pressure vessel monitoring [24], and materials characterization [25], among others.

Two of the most significant features of AE from the standpoint of this paper include:

1. Detection of energy released from within the system rather than that supplied to the system.

2. Detection of dynamic degradation of the system thereby permitting real-time monitoring of system changes.

Any material under stress and containing internal defects has elastic strain energy. This energy may be released by an event such as crack propagation, volumetric changes, or diffusionless phase transformations. While most of the stored energy is converted to heat or surface area changes, a small percentage (approximately 1%) is released as

acoustic stress waves with some residual stored elastic energy [26]. As the waves propagate to boundaries of the material, small surface vibrations are generated (Figure 2.1). A transducer coupled to the surface will convert the displacements of these vibrations to proportional voltages. If these signals are properly amplified and processed, they may be used to analyze the material change which activated the acoustic emission sources.

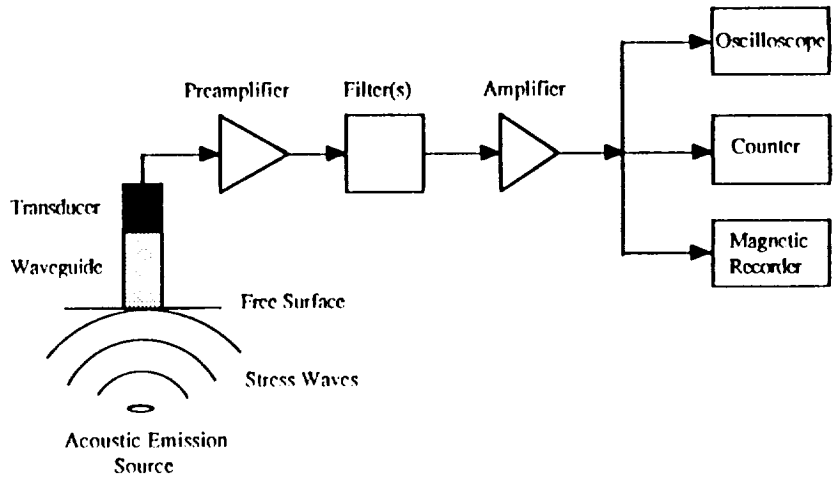

Figure 2.1 Generation and detection of acoustic emission.

Information about both the location and characteristics of the source may be derived from the processed signals, although the latter is much more difficult. The development of acoustic emission as a viable NDE method has been impeded by the inability to determine the source characteristics, poor data interchangability due to nonstandard detection systems, and a lack of mathematical and physical understanding of the acoustic emission waves. Until recently, the signals have been regarded as the output of a black box consisting of the structure, transducer, and coupling.

In general, AE is a transient non-repeatable phenomenon sensitive to the geometry, composition, and stress condition of the material, as well as orientation of the source to the transducer [27]. Although the acoustic emission monitoring equipment is non-destructive to the material, the technique cannot be applied unless the material releases strain energy.

2.1.2b Conventional Analysis

Conventional acoustic emission analysis is the term used in the present study to describe data interpretation based on parameters of the AE signal exceeding a preset threshold. It was used throughout most of the testing in this study to characterize burst signals during solidification. As shown in Figure 2.2, these signals have amplitudes above the background noise and are of short duration (a few microseconds to a few milliseconds). Parameters derived from the bursts include the "hit" which rises rapidly to a peak amplitude during the "rise time" and decays exponentially to the background noise level. The total time of the hit is defined as the "duration" and the number of times that the damped sinusoid exceeds the threshold are the "counts". Also, a pseudo-energy term known as the "measured area under the rectified signal envelope (MARSE)" is electronically calculated by integrating the area above the threshold of a rectified AE signal [28].

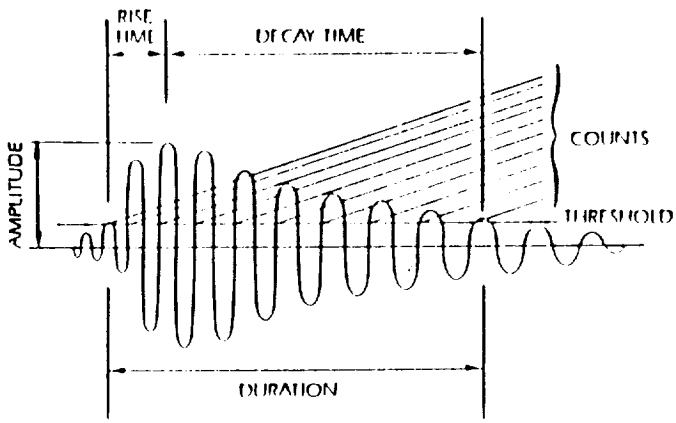

Figure 2.2 Definition of AE waveform parameters in conventional analysis.

The data may be displayed in many forms depending on the objective of the application. Common methods of plotting used in this study include, among others:

1. Cumulative hits or counts v. time to display rates or periods of strong AE activity. The independent variable may be changed to applied load or temperature to correlate the AE with mechanical or thermal changes (Figure 2.3a).
2. Cumulative hits or counts v. amplitude to indicate in histogram format trends in signal intensity (Figure 2.3b). For example, a large number of hits at a specific amplitude may be indicative of a particular type of signal.
3. Non-cumulative point plots which may show clustering as an indicator of common sources (Figure 2.3c). Two clusters of hits with long and short durations in a common amplitude range may indicate two types of sources.

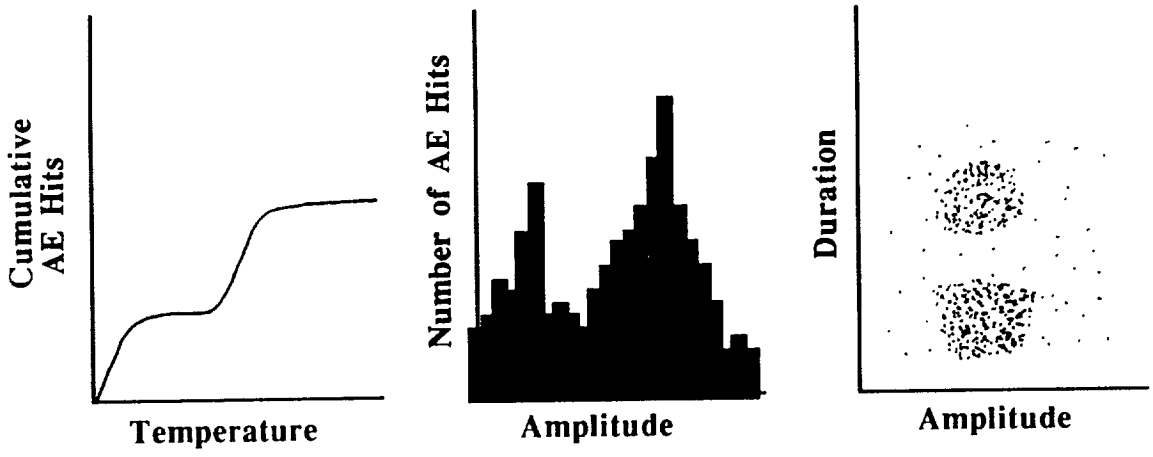

(a) (b) (c)

Figure 2.3 Typical acoustic emission plotting formats:

(a) cumulative line plot, (b) histogram, and (c) non-cumulative point plot.

There are limitations of the conventional AE method. One is that the data is strongly dependent on the magnitude of the selected threshold. If it is set too high, potentially significant data which may be above the background noise, yet below threshold, will not be recorded. At the other extreme, a low threshold may record background noise as viable signals. Voltage signals generated by electromagnetic interference, inductive motor noise, or line voltage fluctuations may appear as periods of strong AE activity. Lowering the threshold on a specific signal has the effect of increasing the measured duration, rise time, and energy. It may also increase the number of counts. The only parameter which is not affected by the threshold is the peak amplitude. However, this too may be altered by changing the gain. A higher gain will increase the amplitude and,

if the threshold is held constant, may also increase the duration, number of counts, rise time and energy.

A second limitation, although not generally a problem, is based on the hit definition time (HDT). If the time allocated for hit detection is too short, one signal may extend into the next HDT and be recorded as two events. A long HDT, on the other hand, may combine two short duration events into one hit [29].

Finally, the conventional method is a digitizing procedure which converts an analog waveform into approximately eight discrete data fields. Once recorded, the original waveform is lost along with valuable characteristics related to frequency. This may not be a problem in applications involving thousands of events in a short period of time. However, in research where the waveform may hold the key to source characterization the conventional AE analysis method must be supplemented by waveform recording techniques and processing.

2.1.2c Waveform Analysis

Waveform analysis of acoustic emission signals is the expression applied in the present study to describe the examination and comparison of individual waveforms from AE signals. The intent is to find characteristics of the waveforms(s) in either the time or frequency domain that may identify the source(s). Another objective is to compare many signals for trends of these characteristics and, thereby establish statistical confidence in the source identification. This section will present an overview of signal and spectral processing as it was applied to the solidification experiments.

Figure 2.4 depicts a system for measuring and recording an acoustic emission signal during solidification. It illustrates the functional blocks found in most signal processing systems. The source, which occurs during cooling of the molten metal, has produced an *analog* signal in the input transducer. It is called this because the continuously varying voltage signal is similar or *analogous* to the surface displacements of the waveguide and crucible which are in contact with the liquid metal. The input processor prepares the electrical information for transmission to the output processor and transducer. At the destination it may be displayed as a chart record, or video image, among others.

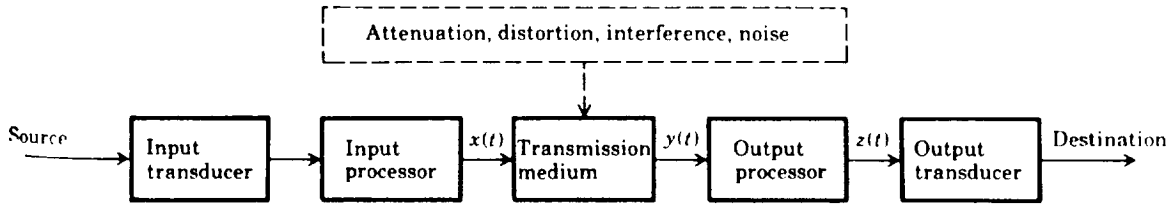

Figure 2.4 Functional elements of a signal processing system.

The goal of perfect signal transmission is hampered by attenuation, distortion, interference and noise. The contributions of these effects in each component of the measurement system will be reviewed in Sections IV, Results and Discussion - AE Signal Analysis. It should be noted that they occur during mechanical transmission of the acoustic signal from the melt to the transducer as well as during electrical transmission to the recording destination.

Attenuation, caused by energy losses within the system, reduces the signal intensity or amplitude. Distortion is any alteration of the waveform due to nonlinearities. Interference is contamination by extraneous signals, while noise comes from natural sources internal to the system. Successful transmission requires signal processing to correct these problems at the input and output. Examples are: amplification to compensate for attenuation, filtering to reduce interference and noise, and frequency translation or modulation to obtain a signal that better suits the characteristics of the system.

In addition to these four effects, a fifth is loss of signal fidelity by analog-digital conversion. By nature of the measurement equipment and for speed of computational signal analysis, the continuous-time analog waveform is sampled at equally spaced or Nyquist intervals to produce a discrete-time signal. This is further processed by quantizing the amplitude to generate a digital signal. The digital signal may then be considered either as a graphical display of points on an x-y coordinate plot or as a binary array. Figure 2.5 illustrates the conversion of a 100 KHz $1V_{p-p}$ (peak-to-peak) sine wave to an 8-bit (2^8=256) single dimension 1x17 integer array which is also shown numerically.

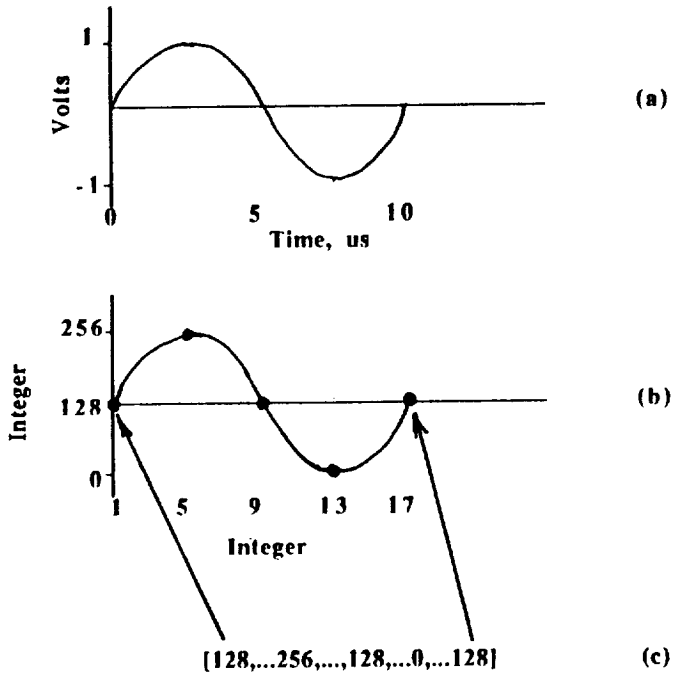

Figure 2.5 Conversion of (a) an analog signal to (b) a digital plot and (c) a numerical array.

Two primary concepts should be understood after examining Figure 2.5. The first is that the true waveform has not been recorded in the digital signal. As the sampling rate decreases the reproducibility of the original signal also decreases. The second is that, although some of the waveshape is lost, the signal has been converted to a form which is easily processed as a mathematical array.

The integer array may be multiplied or shifted by constants to recreate the original signal format of time-voltage or to produce an amplified or expanded version of the signal. It may also be integrated, differentiated, convolved or catenated with other signals, or converted to the frequency domain using a fast Fourier transform (FFT) algorithm.

The FFT algorithm of the ASYSTANT-GPIB program [30] requires that the data be a power of two in length (maximum = 4096 bits) and is defined as

$$f(k) = \sum_{j=0}^{n-1} f(j)e^{-j2\Pi i(jk/n)} \qquad (k = 0,1,...,n-1) \qquad \text{(Equation 2)}$$

For real signals the magnitude of the FFT returns a symmetrical spectrum showing both real and aliased frequencies. However, it is conventional to display only the real frequencies and to scale the x-axis for frequency in Hertz. The power spectrum is defined to be the squared magnitude of the Fourier transformation. A typical acoustic emission signal generated during solidification is shown in Figure 2.6. The upper plot is the time domain representation and the lower plot is the power spectrum.

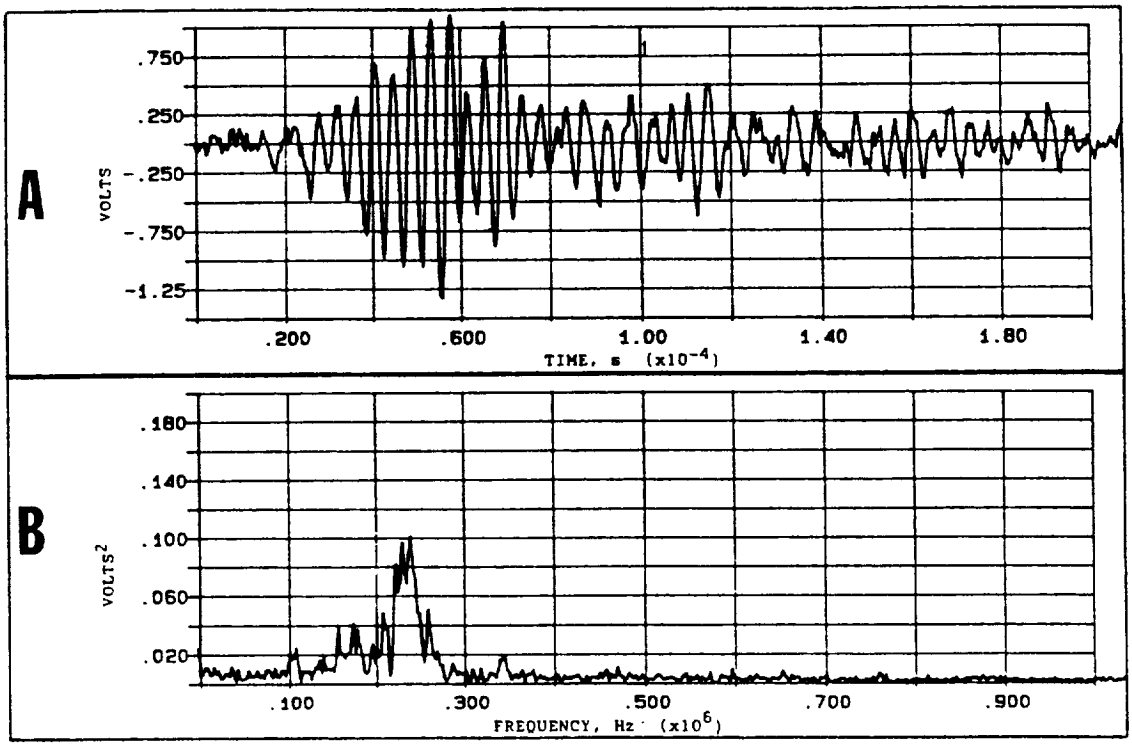

Figure 2.6 A typical acoustic emission signal generated during solidification as shown in (a) the time domain and (b) the frequency domain (power spectrum).

The experimental system of the present study uses many of the ideas just presented. Waveform processing is accomplished using:

(a) a piezoelectric crystal as the input transducer to provide an analog voltage representation of the acoustic emision signal,

(b) an analog amplifier with frequency filtering to boost the signal intensity and remove interference before transmission,

(c) coaxial cables to transmit the signals to the first output processor, the main amplifier,

(d) coaxial cables to transmit signals to the second processor, the digital storage oscilloscope, where the signal is sampled and digitized,

(e) an IEEE-488 bus to transmit the digitized signals to the third output processor, the waveform processing software and

(f) the destinations are computer storage, a video display, and an x-y plotter.

In many cases the waveform processing was done in parallel with conventional acoustic emission recording. While the number of hits, durations, et cetera, were being continuously monitored, individual waveforms were recorded at regular intervals throughout the solidification process. These were stored as single dimension arrays, typically 1-2 Kbytes long, that could be converted to both time and frequency domain representations at a later time. To do so, information such as sampling rate (points/sec) and voltage sensitivity (V/div) was recorded for each waveform and stored with the arrays.

2.1.3 AE - The Physical Phenomenon

2.1.3a General

Acoustic emission waves are, in most materials, ultrasonic, but some are audible. They are also known to be of wide-band nature [31]. The energy of the wide-band excitation emitted by the source is disseminated among the natural modes of vibration of the specimen. Therefore, any measured AE signal at the surface reflects mainly the frequency characteristics of the transmission path, eg. medium and transducer, rather than that of the event. The bandwidth limitation of the transducer further modifies the frequency content of the measured surface displacement. Because of these factors and reverberation within the transmission medium, a recorded AE signal is a poor facsimile of the original event at the source.

Two types of AE signals have been recognized and classified [32]: burst and continuous (Figure 2.7). A burst is a short duration (50 -500 μs) transient signal in the form of a complex decaying oscillation. A continuous signal is low level activity with an appearance similar to band-limited noise.

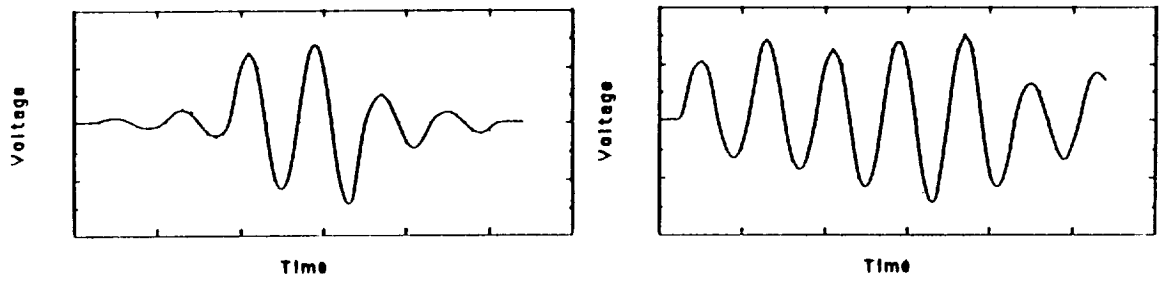

(a) (b)

Figure 2.7 Classification of acoustic emission signals: (a) burst and (b) continuous.

Kaiser [4] believed that the acoustic vibrations originated in the grain boundaries of polycrystalline metals as the result of boundary movements under applied stress. He noted that for a given metal there exists a characteristic spectrum of frequency and amplitude related to the stress level. In 1955, B.H. Schofield [33] disproved Kaiser by observing emissions from single crystals without finding any characteristic spectra of frequency or amplitude. In 1962, Kroll [34] studied simulated AE in order to select the proper frequency range to monitor. Three distinctive frequencies were found to be excited: (1) the fundamental longitudinal resonance frequency of the specimen, (2) the first harmonic frequency of the transducer crystal, and (3) the fundamental frequency of the transducer crystal.

The bandwidth of acoustic emission events at the source extends much beyond that of a conventional transducer [35]. High frequency components are severely attenuated and the spectrum of the AE signal is dominated by the resonant response of the specimen due to its boundary conditions. Therefore, it has been very difficult to identify differences in frequency spectra from a finite thickness specimen using a band-limited transducer. An important fact is that the transducer has a finite mass and size which changes the measured signal due to mechanical impedance. It is also difficult to compare spectra from different experiments since they vary with changes in specimen shape, transducer type, and coupling between the transducer and specimen [36].

2.1.3b Source Characteristics

The detected surface motion due to an AE source contains information about both the location and the characteristics of the source. Although the sources can be detected and located with a high degree of accuracy, their characterization is much more difficult. Because of this, a significant part of today's research has been directed towards the so-called inverse problem which is concerned with distinguishing AE sources based on analysis of the recorded voltage waveforms. Fortunately, in any given application there is interest in finding only one or two major AE sources rather than all those present.

The deconvolution method of solving the inverse problem has received considerable research interest during the past twenty years. It is a filtering technique which may be performed electronically or mathematically depending on the state of the signal. Kishi [37] described the linear response theory as a detected signal, V(t), being the convolution (indicated by *) of the system transfer function, S(t), the dynamic Green's function, G(t), and the source function of the AE signal D(t).

$$V(t) = S(t)*G(t)*D(t) \qquad \text{(Equation 1)}$$

Deconvolution suggests that if the transfer functions of the system (including transducer) and medium are determined by pencil lead breaks or computer simulation, then the effects of measurement may be filtered, leaving the acoustic emission source function.

Park and Kim [38], on the other hand, have shown that calculations based on Green's functions under elastic assumptions lead to erroneous results in a highly attenuating or dispersive medium. The elastic restriction does not consider attenuation and dispersion which leads to an unrealistic source function. Kline and Ali [39] demonstrated that the

dispersion effects are small in comparison to attenuation. For aluminum, the actual result of moving the transducer farther from a calibrated source is a small increase in rise time along with the expected decrease in surface displacement.

Ohtsu [40] showed that deconvolution analysis only provides information on the time dependency of the AE source. The orientation of a dipole source: e.g. a crack, also affects the results. Therefore, it must be determined for each source before deconvolution is performed. His proposed source inversion procedure involved four steps. The first was waveform collection on at least five channels. Using longitudinal or "p-wave" arrival times, each wave was located. Moment tensor analysis then distinguished the crack type and orientation based on p-wave amplitudes. The final step was the deconvolution analysis to determine the source-time function.

Another method of quantifying acoustic emission signals was proposed by Yu and Clapp [41]. Based on previous work by Sato [42] and Savage [43], they provide evidence that the first node frequency of the amplitude spectra of an acoustic emission signal is proportional to the final radius of the expanding source. They also develop formulae on the source growth velocity in terms of the rise time of the p-wave. In other words, the first node frequency and the rise time of the p-wave, in theory, may be used to determine the final size and average growth velocity of an AE source. This would, of course, be very useful if the source during solidification were thought to be an expanding nucleus or pore. Each has a growth velocity that may be estimated and a measurable final size.

It can be seen that there are many ways to distinguish one signal from another. In addition to the above, a study [44] has used homomorphic filtering which uses the inverse log of the fourier transform, the Hilbert Transform, of each signal rather than deconvolution. Pattern recognition based on clustering of statistical parameters has also been implemented [45]. The present study takes all of the previous work into consideration; but without the goal of determining the original source waveforms. The assumption throughout the experiments was that, if the system does not change, it will have the same effect on every signal. If two signals are different at the source, they will be different at the detector. If they are similar at the source, they will be similar at the detector. Therefore, trends in detected signals should indicate major sources which may be substantiated by thermal or metallographic analysis.

2.2 Solidification

2.2.1 General

Solidification is the transformation of a metal or alloy from a non-crystallographic to a crystallographic state. The mechanisms that are involved in this transformation affect parameters such as cooling rate, and alloying and ultimately, the mechanical properties of the casting. It is the intent of this section to provide some of the concepts of solidification modelling so that correlated models of acoustic emission sources that occur during this transformation may be developed in Section V - AE During Solidification.

Under suitable conditions, where liquid metal is supercooled below its equilibrium melting temperature, there exists a driving force for solidification. One might expect that this would occur spontaneously. However, the transformation must first begin by the formation of solid nuclei. In pure metals, growth of the solid nuclei is controlled by the rate at which latent heat of solidification can be conducted from the solid into the liquid. Depending on the degree of supercooling, a spherical nucleus may continue to grow with a planar solid/liquid interface or may become unstable and form arms known as dendrites.

Primary dendrite arms will develop in preferred crystallographic directions and break up into secondary and tertiary arms. The commonest dendrite is equiaxed with similar dimensions in all directions (Figure 2.8a). If a steep thermal gradient exists, dendrites will grow perpendicular to the gradient and are known as columnar dendrites (Figure 2.8b) [46].

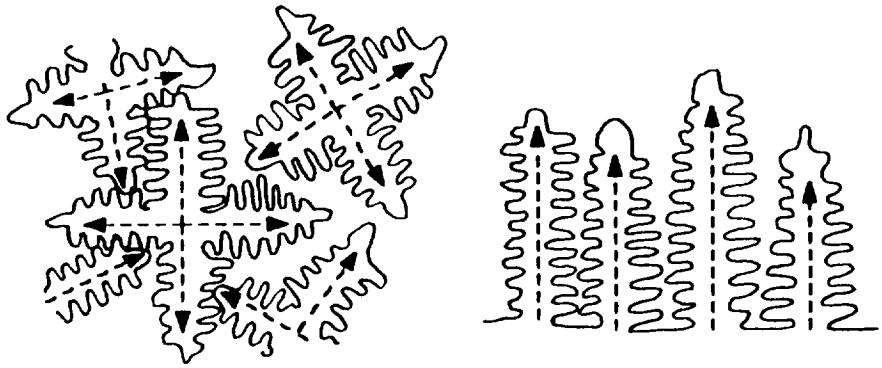

(a) (b)

Figure 2.8 Types of dendritic structures: (a) equiaxed and (b) columnar.

While a pure metal freezes at a specific temperature over a range of time, an alloy freezes over a range of temperature and time. When it occurs over a relatively wide range of temperature and the thermal gradient of the metal from outside to inside is not steep, the fully liquid zone disappears early in solidification and a fully solid zone does not appear until the solidification is almost complete. During most of the process, liquid and solid coexist throughout the casting although the compositions of both phases change during cooling.

During solidification, one also encounters two types of inclusions. One type is trapped by growing dendrites; the other has a tendency to be pushed by the growing metallic solid into the spaces between the dendrites. The pushed inclusions are free to move and, therefore, collide with each other forming clusters. Small vacant spaces, known as microporosity, also form as a result of shrinkage or the evolution of gas during solidification or a combination of the two. Figure 2.9 illustrates these microscopic inhomogeneities.

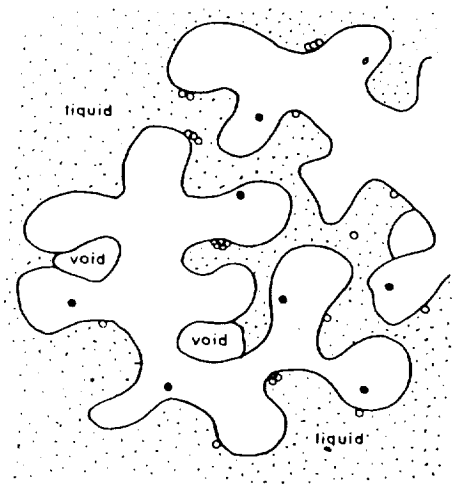

Figure 2.9 Microscopic inhomogeneities that develop during solidification: trapped inclusions (black circles), pushed inclusions (white circles), and microporosity (voids).

Whereas, the solidification rate of pure metals is controlled only by heat conduction, alloy solidification is controlled by solute diffusion and conduction. The simplest description of a solidifying alloy is based on equilibrium solidification where the process is presumed to proceed at such a rate that there is complete diffusion in both the solid and liquid states. A more practical description of the process is given by the non-equilibrium lever rule or Schiel model [47]. It predicts the solute concentration as a function of solid fraction

$$C_s = kC_o(1-f_s)^{k-1} \qquad \text{(Equation 3)}$$

where C_s is the composition of the isoconcentrate enclosing a weight solid fraction f_s. C_o is the initial average composition and k is the equilibrium partition ratio derived from the phase diagram (Figure 2.10). This ratio is defined as:

$$k = C_s / C_L \qquad \text{(Equation 4)}$$

where C_L is the composition of the liquid.

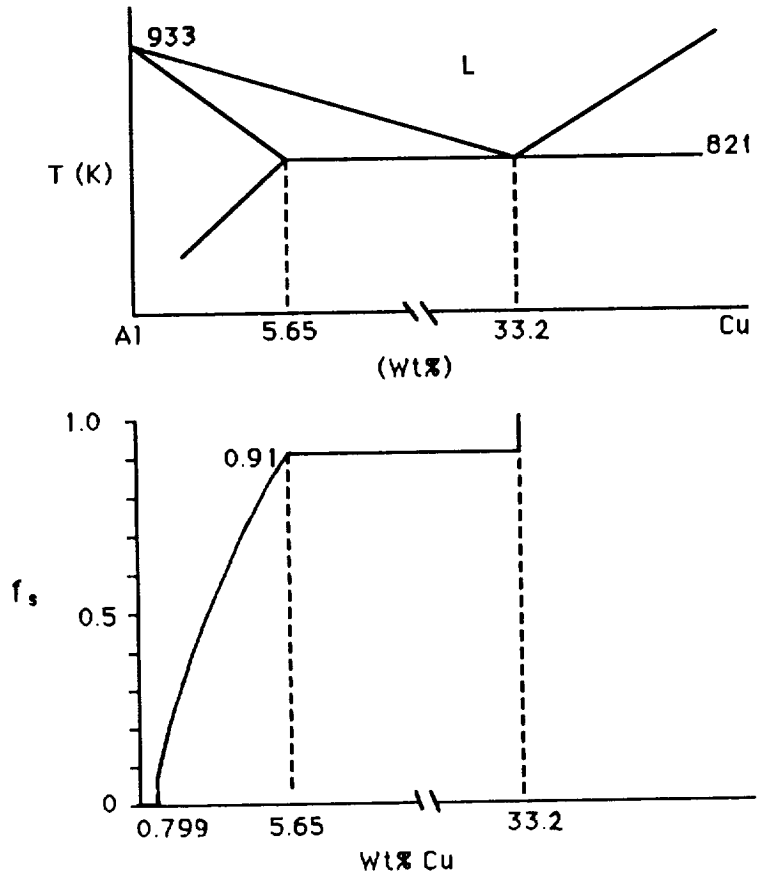

Figure 2.10 Schiel plot for Al-4.7%Cu derived from phase diagram.

Important assumptions of this model are local equilibrium at the interface, negligible supercooling before nucleation, no mass flow in or out of the volume element, and negligible solid diffusion. The equation may be used from 0 to 5.65 wt% Cu, the maximum solubility of copper in solid aluminum. It predicts that the first solid to form (the centers of the dendrites) will have a composition of 0.799 wt% Cu increasing to 5.65 wt% Cu at f_s=0.91 (near the edge of the dendrites). The remaining fraction (0.91-1.00) freezes as an interdendritic eutectic with an average composition of 33% Cu. The volume fraction of eutectic, f_E, in a casting may be predicted by

$$f_E = (C_E / C_o)^{1/(k-1)} \qquad \text{(Equation 5)}$$

where C_E - eutectic composition

C_o - initial composition

k - partition coefficient

for Al-4.7 wt% Cu the volume fraction of eutectic is:

$$f_E = (33/4.7)^{1/(0.17-1)} = 9.56\% \qquad \text{(Equation 6)}$$

This segregation leads to constitutional supercooling which is responsible for dendrite formation (perturbation of advancing planar solidification front) in aluminum-copper alloys.

Eventually the metal is completely solid as the dendrites collide and form grains. At the scale of crystal grains, ranging from millimeters to centimeters, one finds that each grain is composed of tens to tens of thousands of dendrite arms. All of the arms within a grain, however, developed from the same initial growth point, the nucleus, and their crystallographic orientation is approximately the same (Figure 2.11). It is customary to say that the grain consists of a single dendrite [48].

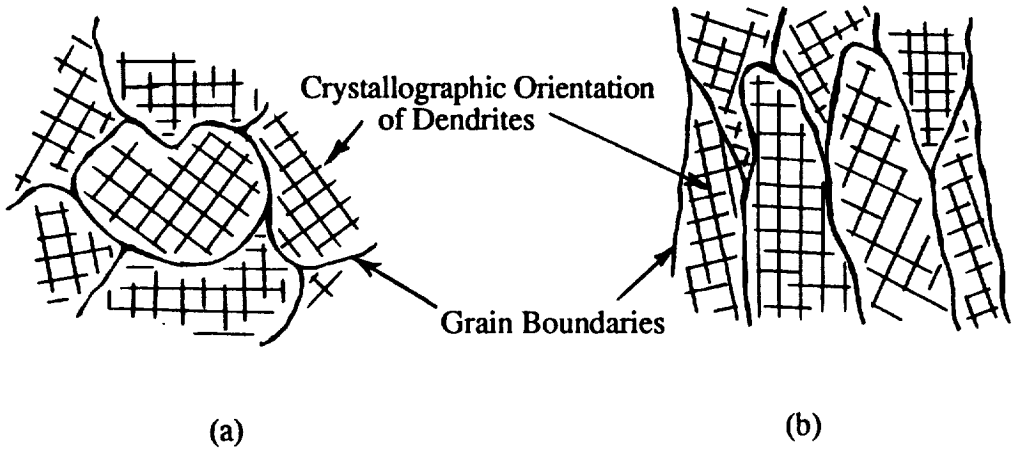

Figure 2.11 Types of grain structure: (a) equiaxed dendritic and (b) columnar dendritic.

2.2.2 Thermal History Curves

The general behavior of the thermal history or cooling curve obtained during solidification of an alloy of finite freezing range is well known [49]. Generally, initial undercooling is observed. Then, recalescence is followed by a period of temperature arrest. Finally, continuously descending temperature occurs during the remainder of growth of the primary solid phase. After some undercooling the growth of non-equilibrium eutectic occurs at constant temperature.

Typically, in a thermal history curve (Figure 2.12a) obtained from a casting having a fully columnar structure, initial cooling is usually followed by a relatively long plateau period. In a columnar-equiaxed or fully equiaxed structured ingot, a well defined recalescence following the initial thermal undercooling (Figure 2.12b) is characteristic of the thermal behavior.

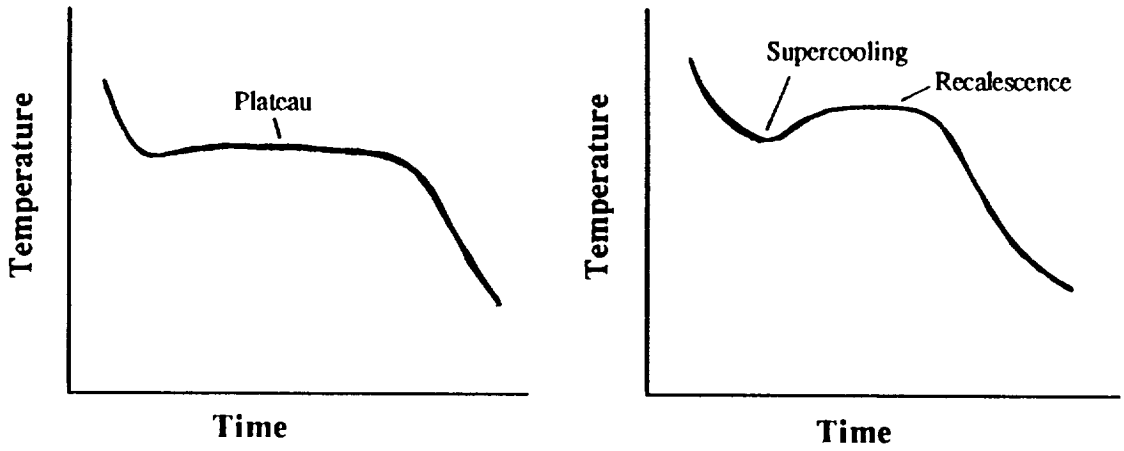

(a) (b)

Figure 2.12 General cooling behavior of (a) fully columnar and (b) fully equiaxed grain structure.

Thermal arrest on a cooling curve is the stage of the solidification process at which the instantaneous rate of release of latent heat of fusion exceeds the instantaneous heat withdrawal rate from the metal. Thermal arrest occurs during the period of nucleation. The plateau periods correspond to the growth period of columnar dendrites in a fully columnar structured casting. The nominal rate of advance of the dendritic solidification front can be estimated by dividing the growth distance by the plateau period on the corresponding thermal history curve. [50] The dendritic solidification front advances at a higher rate with increasing solute content and cooling rate under comparable casting conditions.

The nominal growth velocity of the solidification front, v, is given by

$v = \text{constant} \times t^{-1/2}$ where t = time of grain growth (Equation 6)

Therefore, by measuring the time of grain growth from the thermal history curve and the average grain size from metallography, the velocity of the dendrite and grain growth may be determined. It will be discussed in Section V - AE During Solidification how this is useful in modelling acoustic emission sources during solidification.

2.2.3 Porosity Development

Porosity has been proposed by others [14] to be a source of AE during solidification. Therefore, it has critically been evaluated in the present study. Its development is a complex interaction of gas content in the metal and cooling rate during solidification. A short review will now be presented to understand the role of porosity in the mechanisms of liquid to solid phase transformations. Special emphasis will be placed on current theories of porosity development in aluminum-lithium alloys.

The low ductility and fracture toughness of aluminum-lithium alloys as compared with conventional aluminum alloys have been primary areas of research during their product development history. Most of this research has been directed towards designing alloys and processes that inhibit planar slip, the factor generally considered responsible for low ductility in these alloys. Other research suggests that it may be caused by the formation of a stable lithium hydride (LiH) phase during ingot casting, not planar slip [51]. A later investigation [52] found no evidence of the hydride phase but did find

significant improvement in fracture toughness and ductility when the hydrogen content decreased.

The behavior of hydrogen in aluminum-lithium alloys differs in several respects from other aluminum alloys [53]. These differences will be discussed below after a review of its solubility in pure aluminum and a survey of porosity development and morphology.

Except for hydrogen, common elemental gases and elements of the halogen group do not exhibit detectable liquid solubility in aluminum, although they do readily form compounds. In fact, hydrogen is appreciably soluble in both solid and liquid aluminum with the latter being much higher. Ransley and Neufeld [54] have reported solubilities of liquid and solid aluminum to be 0.04 cc/100g at NTP (20°C and 760 mm pressure) and 0.004 cc/100g, respectively. Figure 2.13 shows the solubility of hydrogen in aluminum from 500-800°C (930-1470°F) [55].

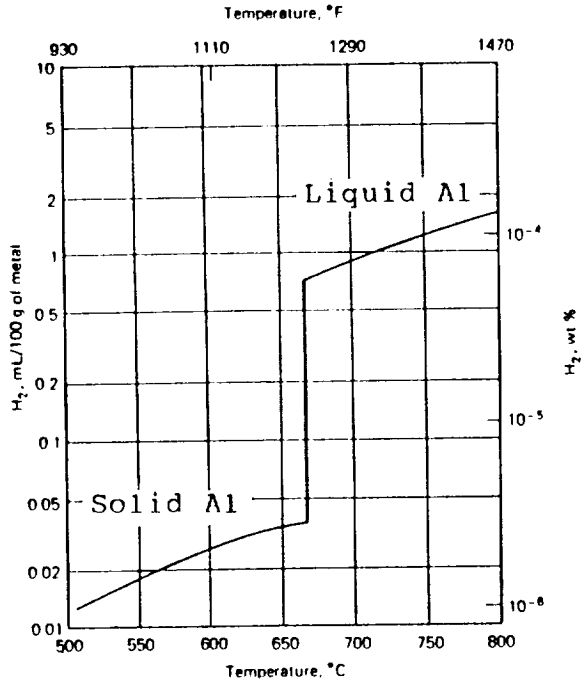

Figure 2.13 Equilibrium solubility of hydrogen at atm. pressure in UHP aluminum [55].

The amount of hydrogen found in solid aluminum can be greater than the equilibrium amount either because of excess amounts present during solidification or because of reactions of moisture on the surface of the metal with subsequent diffusion of hydrogen into the body of the solid [56]. This excess hydrogen along with solidification shrinkage are two factors which interact with each other to promote pore formation in aluminum castings.

Although porosity has been virtually eliminated in ingots of wrought aluminum alloys by the introduction of degassing during the continuous casting process, interdendritic porosity still occurs, particularly in the central regions of the ingots. Investigators suggest that this too can be eliminated if the hydrogen content of the melt is sufficiently reduced before casting. [57]. Therefore, interdendritic porosity is a casting defect of immediate concern.

Interdendritic porosity is generated by the rejection of hydrogen nucleated in the liquid fraction during solidification. As the solidification proceeds hydrogen is rejected from the growing solid crystals into the adjacent liquid as a consequence of the difference of solubility between the solid and liquid metal. The hydrogen content in the liquid rises until it reaches a value sufficient to nucleate gas bubbles. Since this condition is reached near the end of solidification the gas bubbles are restricted to occupy the spaces between the growing dendrites, and the bubbles become irregular gas-filled cavities.

Entwistle, et al. [58] examined porosity types, distributions, and the influence of hydrogen content in aluminum alloys. Their major conclusion was that porosity follows a definite pattern until gas concentrations become abnormally high. In fine grain castings

with lower amounts of porosity a fine interdendritic morphology was found (Figure 2.14a). As the grains coarsen, the porosity becomes intergranular which is more continuous and more irregular in nature (Figure 2.14b). Intergranular porosity occurs on a scale larger than the size of a dendrite and is caused by a combination of thermal contraction and improper feeding. At high hydrogen concentrations the pores are of a spherical gas bubble shape (Figure 2.14c). For the latter case, it is the gas level, rather than interdendritic feeding which determines the type of porosity.

(a) (b) (c)

Figure 2.14 Types of microporosity in aluminum: (a) interdendritic, (b) intergranular, and (c) free gas pores [58].

Entwistle, et al. also plotted porosity profiles as shown in Figure 2.15 for 10 cm x 10 cm ingots of an Al-4.5 wt% Cu alloy. Figure 2.15a shows an ingot containing a refined equiaxed grain structure. The iso-pores, lines of equal volume percent of

porosity, show that the greatest percent of porosity is concentrated at the top center of the casting. For a coarse columnar-equiaxed dendritic structure formed in refined grains, the distributions became more concentric (Figure 2.15b). Finally, the irregular profile of a coarse-grained ingot in Figure 2.15c reflects the difficulty of feeding long interdendritic channels.

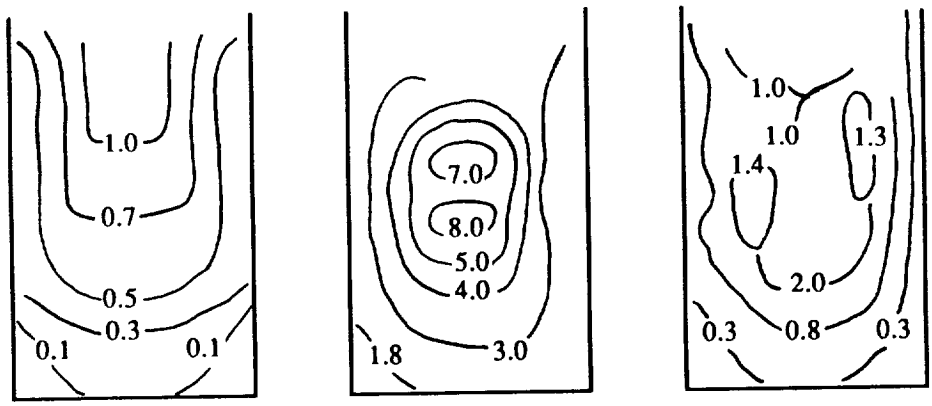

(a) (b) (c)

Figure 2.15 Microporosity profiles in aluminum ingots: (a) equiaxed, grain refined, (b) columnar-equiaxed, grain-refined and (c) columnar, coarse grained [58] illustrating lines of equal volume percent of porosity.

Their results indicate that over a range of hydrogen concentration of 0.19 to 0.46 ml H_2(STP)/100g Al in Al-Cu alloys that the dissolved gas content is not an important variable in determining porosity distribution or mean porosity. The solidification

conditions, rather than the hydrogen content itself, have the major influence in microporosity formation. If the gas level is too high, shrinkage is of little importance in determining porosity formation. If the gas level is too low, the solidification shrinkage is itself ineffective in producing pores. The interesting feature of porosity is that in the intermediate range, although both gas and shrinkage act together, it is the shrinkage (the solidification mechanism) which determines where pores form and their total volume.

Another conclusion of Entwistle, et al is that there is a dependence of the volume percent of porosity on the local solidification time at lower superheats (50°K) where interdendritic porosity is found. At higher superheats (175-300°K) where much coarser porosity is found, there is no dependence of the amount of porosity on local freezing time. The amount of microporosity increases as the freezing time increases, ie., as the cooling rate decreases. Greater microporosity is associated with more slowly cooled and somewhat coarser structures.

2.3 Aluminum-Lithium Alloys

2.3.1 General

Research on the alloying of lithium with aluminum began in Germany in the 1920's [59]. The first commercially available aluminum-lithium (Al-Li) alloy, x2020, was used in 1957 in the wings and horizontal stabilizers of an experimental Navy aircraft. It contained about 1.1 wt% lithium. In 1969, the alloy was removed from production because of segregation effects, low toughness and ductility, and problems during casting because of the high reactivity of lithium. The stimulus to again produce aluminum-

lithium alloys was the emergence of fiber-reinforced composites as possible substitutes for conventional aluminum in aircraft.

Besides beryllium, which forms an extremely toxic oxide, lithium is the only alloying element that both decreases the density and increases the elastic modulus of aluminum. The low solubility of beryllium in aluminum (less than 0.03 wt%), however, leads to massive segregation of the beryllium-rich phase upon solidification.[60] and poor mechanical properties result.

For each 1 wt% lithium addition, the density decreases by about 3% and Young's modulus increases by about 6% for lithium additions up to 4 wt% [61]. It is not possible to continue to simply increase the lithium content beyond a level of about 3 wt% in production since deleterious effects are observed on the toughness and ductility.

Some of the original industrial and military goals of Al-Li research have included:

a) an alloy to replace fracture-tough 2024-T3x,

b) an alloy to replace high strength 7075-T6x and

c) an alloy to replace moderate-strength, stress corrosion-resistant 7075-T73x.

Currently, there is still no commercial Al-Li alloy having a significant reduction in density that has both the strength and toughness of conventional 7075-T6x or the strength and stress corrosion resistance of conventional 7075-T73x. The major technical problem, only recently recognized by the aluminum producers, is that commercial aluminum-lithium alloys are not direct substitutes for conventional aluminum alloys. The difference between Al-Li and conventional aluminum alloys has been compared to that of carbon steels and stainless steel alloys.[62]

The reduction in density of commercially available aluminum-lithium alloys is not as great as researchers originally anticipated. Current alloys have 7-9 % lower densities than 7075. The promotional claim of the early 1970's that Al-Li alloys may offer a 10% reduction is now almost forgotten. Several newly developed Al-Li alloys have been produced with better toughness and stress corrosion cracking resistance than 7075 but with equivalent mechanical properties [62].

There many reasons for the developmental problems of aluminum-lithium alloys. They are harder to cast without experiencing cracking because of the segregation and porosity which are difficult to control. There is also a decrease in toughness and stress corrosion cracking (SCC) resistance with increasing lithium content. Al-Li alloys usually delaminate along the normal short-transverse (S-T) direction (Figure 2.16) during fracture. As the toughness is increased by aging, the SCC resistance decreases, particularly in the S-T direction.

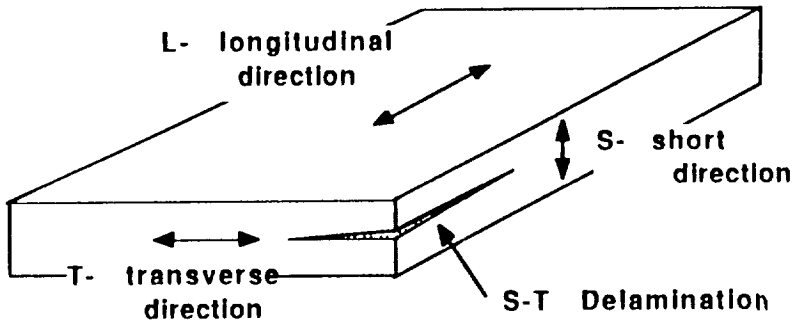

Figure 2.16 Definition of short transverse direction.

The commercial Al-Li alloy that was selected for testing contains major constituents of copper and zirconium in addition to the lithium. The following review of its physical metallurgy explains the purpose of each constituent, some basics of how the commercial alloys achieve their desired properties, and an introduction to the microstructural development in cast Al-Li alloys.

2.3.2 Physical Metallurgy

Precipitation-hardened aluminum-lithium alloys obtain their strength from the formation of a large volume fraction of a meta-stable, ordered and coherent δ' (Al_3Li) phase having a $L1_2$ type superlattice structure. [63] The $L1_2$ lattice structure consists of eight shared corner sites occupied by lithium and six shared faces occupied by aluminum similar to the Cu_3Au structure. In Al-Cu-Li alloys additional strength is achieved by the co-precipitation of copper-rich phases independent of the δ' precipitation. For example, in high lithium-low copper alloys (>2wt% Li, <2wt% Cu) the decomposition of the supersaturated solid solution (α_{ss}) occurs by the reaction:

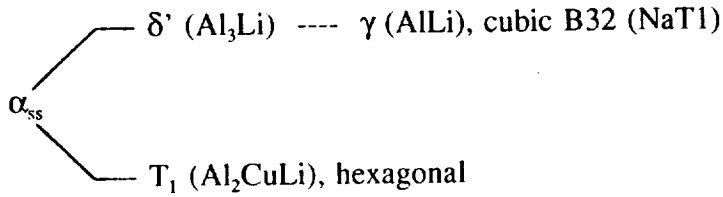

The less than optimal deformation and fracture behavior of Al-Li type alloys has been attributed to one or several of the following:

a) strain localization that results from planar slip of shearable precipitates,

b) formation of coarse intermetallics during slow solidification,

c) high levels of trapped hydrogen and

d) grain boundary segregation of tramp elements such as sodium, potassium, and sulfur.

Unlike lithium, these tramp elements have virtually no solid solubility in aluminum and may lead to grain boundary segregation.

During plastic deformation of Al-Li the coherent δ' precipitates are sheared by dislocations. The planar slip associated with δ' shearing leads to heavy localized dislocation pile-ups at grain boundaries which, in turn, generate stress concentrations across grain boundaries.

Al-Li alloys have been reported to contain over ten times the amount of hydrogen normally found in high strength, non-lithium aluminum alloys [64]. This has been attributed to a large increase in the solubility of hydrogen in the lithium-alloyed matrix, and to the formation of a hydrogen-rich phase during solidification. Investigators have suggested that the poor ductility of Al-Li alloys might be caused by the formation of a stable hydride of either lithium as LiH or of aluminum and lithium as Li_3AlH.

Some of the approaches for improving toughness in Al-Li-X alloys involve [65]:

a) encouraging dislocation cross-slip or precipitate by-passing in the alloy by modification of the lattice parameters to increase mismatch in the Al-Al_3Li system,

b) introducing secondary precipitation systems and

c) using a dispersion hardening system in addition to the precipitation system.

Other approaches include grain refinement via additions of Mn, Zr, Cr or Co and minimizing the presence of tramp elements (potassium, sodium, and sulfur).

Zirconium has been found to be the most effective element for inhibiting recrystallization in Al-Li alloys [66]. An addition of 0.2 wt% Zr is sufficient to completely prevent recrystallization. The benefit is that unrecrystallized alloys have much higher strengths than either partially or fully recrystallized alloys.

The close match between the lattice parameters of the precipitate and matrix in Al-Li alloys results in a small misfit strain and leads to a homogeneous distribution of coherent, spherical δ' precipitates [67]. This particular precipitate mechanism is analogous to the δ-δ' ($Ni-Ni_3Al$) system which gives nickel-based superalloys their high temperature ductility.

The improvements in elastic modulus and density in the alloy occur whether the lithium is present in solid solution or as δ' precipitates. However, improvement in strength accompanies the nucleation and growth of δ' and the magnitude of the effect increases with the volume fraction and size of δ '[68]. Copper is added to increase the strength and aid in homogenizing deformation since it co-precipitates to form T_1 with δ'. Table 2.1 illustrates changes in strength and ductility accompanying these alloy additions. The last alloy listed in the table is similar to the commercial alloy used in the present experiments.

Table 2.1 Effect of alloy additions on mechanical properties of Al-Li alloys.

Alloy	Elastic Modulus	Yield Strength	Tensile Strength	Ultimate Elongation
(wt %)	(GPa)	(MPa)	(MPa)	(%)
Pure Al	68.0	12	47	60
Al-1.5 Li	76.5	46	94	30
Al-2.3 Li	80.5	195	278	7
Al-2.5 Li-2.5 Cu-0.1 Zr	79.4	455	504	4

2.4 Summary of Background

Acoustic emission and aluminum-lithium alloys are two ostensibly unrelated subjects which have evolved over the same time periods with a common lack of acceptance. Both have immense potential yet both have inherent problems that have not been overcome. The present research uses one topic to study the features of the other with the intent of improving the value of both.

A short history of each subject has been presented including discussions of previous investigations. The physical metallurgy of Al-Li alloys was summarized to emphasize the purpose of each alloying element. The current status of research in AE signal characterization was reviewed. The two methods of acoustic emission monitoring that were used in the experiments, conventional and waveform processing, have also been described.

A more detailed discussion of solidification kinetics and mechanisms will be given in Section V, Results and Discussion - AE During Solidification as it applies to aluminum alloys. More specific information on the interpretation of acoustic emission signals, including the effects of noise, the transducer, and transmission media, will be presented in Section IV, Results and Discussion - AE Signal Analysis.

III. Experimental Procedures

3.1 Materials

Three materials were used in this investigation, each from a single heat obtained from the Alcoa Technical Center [69]. They include ultra-high purity aluminum, an Al-4.7wt% Cu binary alloy, and a commercial grade aluminum-lithium alloy (AA2090). The sample materials were received in the form of a 2.5x3.8x96.5 cm extruded bar, a triangular notch bar ingot, and a 2.5x25x25 cm ingot slice, respectively. Elemental and impurity analyses are listed in Table 3.1.

The as-received materials were saw cut into bars approximately 10x10x150 mm, then machined on a lathe and cut into cylindrical pellets approximately 9 mm diameter x16 mm long. The nominal weights, volumes, and densities are listed in Table 3.2.

Table 3.1 Chemical Analysis of Experimental Materials

Element	Ultra-pure Al	Al-Cu Alloy	Al - Li Alloy
	wt %	wt %	wt%
Li	$< 1.3 \times 10^{-7}$		1.82
B	4.0×10^{-7}		.0002
Mg	8.1×10^{-5}		.01
P	7.0×10^{-5}		
Ti	2.5×10^{-4}		.021
V	1.8×10^{-5}		
Cr	4.2×10^{-5}		
Mn	1.2×10^{-7}		
Fe	6.4×10^{-5}	.11	
Ni	$< 2.2 \times 10^{-6}$	.01	
Cu	1.3×10^{-4}	4.70	2.52
Zn	3.2×10^{-5}		.02
Zr	1.1×10^{-5}		.10
Si	3.9×10^{-4}	.11	

Table 3.2 Nominal Physical Properties of Experimental Specimens Prior to Solidification.

	Aluminum	Al-Cu Alloy	Al-Li Alloy
Density (g/cc)	2.70	2.98	2.60
Mass (g)	2.70	3.00	2.70
Volume (cc)	1.00	1.00	1.02

3.2 Casting

The materials listed in Table 3.1 were typically cast by placing a machined pellet, as described in Section 3.1, into the boron nitride crucible and heating to a temperature above the liquidus of the material in a resistance furnace. As shown in Figure 3.1 the temperature of the furnace was controlled by a variable power supply. The atmosphere surrounding the casting was controlled by placing the crucible inside a 15 mm diameter fused quartz tube approximately one meter long which was sealed with a rubber plug at the top and silicone sealant at the bottom. Inlet and outlet vents were provided to allow the controlled atmosphere of argon or Ar-4.1%H_2 to flow through the tube and, therefore, blanket the casting with a continuous flow of low pressure gas. A type-J (iron-constantan) thermocouple was inserted through the top seal and into the tube so that the T.C. bead would maintain contact with the pellet and monitor direct temperature of the melt. Methods of maintaining contact are described in Section 3.3.1, Temperature.

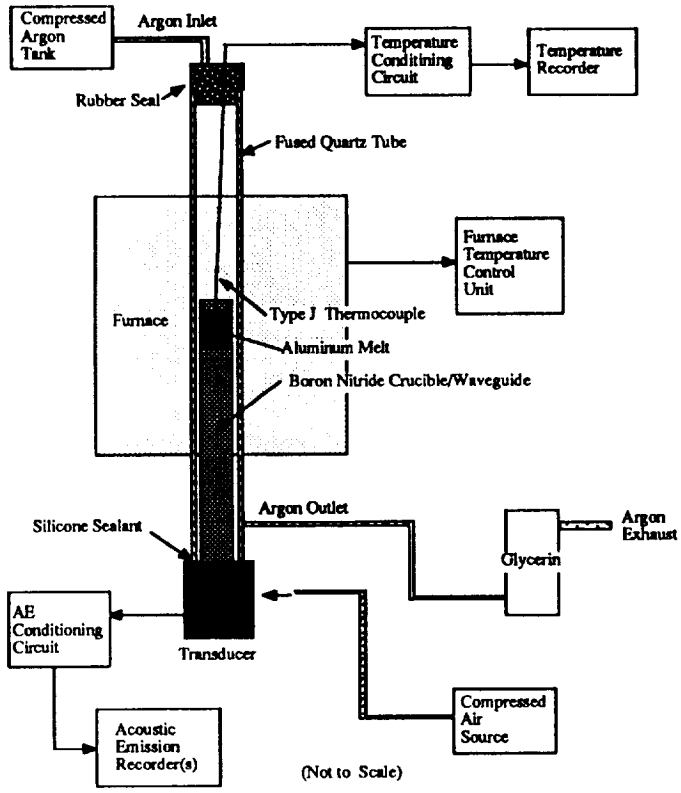

Figure 3.1 Experimental resistance furnace casting system.

When the temperature of the pellet exceeded its liquidus, the pellet melted. A temperature of 40°C above the liquidus was maintained to ensure a uniform liquid state and the melt was permitted to soak for 30 minutes. This was intended to allow diffusion of the grain refiner or hydrogen gas, if used, within the casting. The power supply was then turned off and the system permitted to slow cool in the controlled atmosphere. Cooling rate was regulated by a controlled application of compressed air on the waveguide at the base of the furnace. The casting was removed from the furnace after being cooled to room temperature and then placed in a dessicated chamber until metallographic analysis was performed. No post-solidification chemical analysis was performed.

At the suggestion of metallurgists in the primary processing division of the Alcoa Technical Center, a grain refining chemical additive was used in a series of tests. A 0.03 wt% concentration of Al-10wt%Ti-0.4wt%B, more commonly known as TiB, was added to the melt. In a 3 gram pellet, for instance, the TiB addition would be a 0.0009 gram particle. The intended effect of the TiB addition was a 1000:1 reduction in grain size without changing the transformation temperatures or cooling rate. It was added by drilling a small hole in the top of the pellet, inserting the TiB, and peening the hole closed.

In another series of tests the ultra-high purity argon atmosphere was replaced by a 95.9% Ar- 4.1% H_2 mixture during the melting and solidification processes. The intent was to permit additional hydrogen to diffuse into the melt and produce castings with increased porosity. The procedure was done to help identify whether or not acoustic emission signals are generated by the formation of porosity.

The last series of tests involved larger castings than the standard sizes listed in Table 3.2. The larger castings ranged in volume up to four times the standard sizes. By using a few pellets in a larger crucible, the diameter and volume of the casting increased as well as the number of grains. This permitted distinguishing acoustic emission signals as functions of volume as well as number of grains.

3.3 Data Acquisition

3.3.1 Temperature

The temperature of most interest in the present study was that of the casting itself. Therefore, a Type J thermocouple (T.C.) was initially positioned such that the bead was in contact with the top of the specimen. As the molten metal exceeds its liquidus the thermocouple is pressed into the molten aluminum. A high temperature glass sheathing was surrounded the 24 gauge iron-constantan T.C. wires which have a maximum operating temperature of 704°C. The furnace was carefully monitored to prevent going above this temperature. A Type J was selected for compatability with an available temperature controller.

The thermocouple junction was formed by welding using a micro-torch which had a maximum pinpoint temperature of 2857°C (5200°F) developed from burning a mixture of butane and nitrous oxide. The other end of each thermocouple wire was connected to an Omega Model 310 temperature controller (Figure 3.2) to provide a linearized temperature output. The parabolic relationship of T.C. junction voltage to temperature was electronically converted by the controller to a 1 mV/°C output.

The output of the Model 310 was connected to an Omega Omni-Amp III (Figure 3.2) which amplifies the voltage by a factor of 10x, 100x, or 1000x depending on an internal switch position and has an input impedance of 16 Mohm. It was set throughout all of the tests to 10x which provides an output of 0 to 7 VDC for 0 to 700°C.

Initially, the full scale temperature range (0-700°C) was displayed on the Phillips Model PM3335 digital storage oscilloscope (D.S.O.) which has an eight bit vertical resolution, ie., 256 points. Since 700°C divided by 256 points only provides a

2.75°C/point temperature resolution, this was inadequate for identifying critical changes in cooling rate, such as recalescence. Therefore, in the interest of improving the resolution it was determined that the critical temperature range was 500-700°C. All phase transformations of interest in the present study are in this range (Figure 3.3).

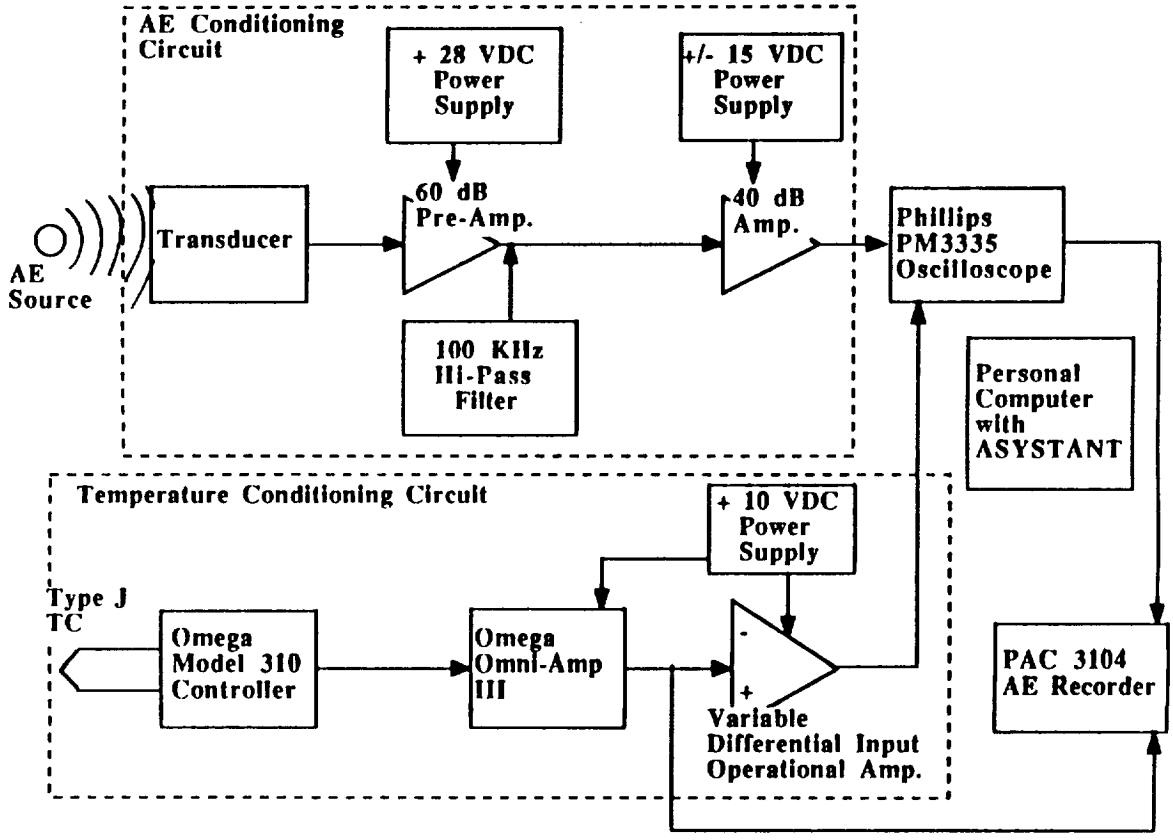

Figure 3.2 Temperature and AE conversion and conditioning circuits.

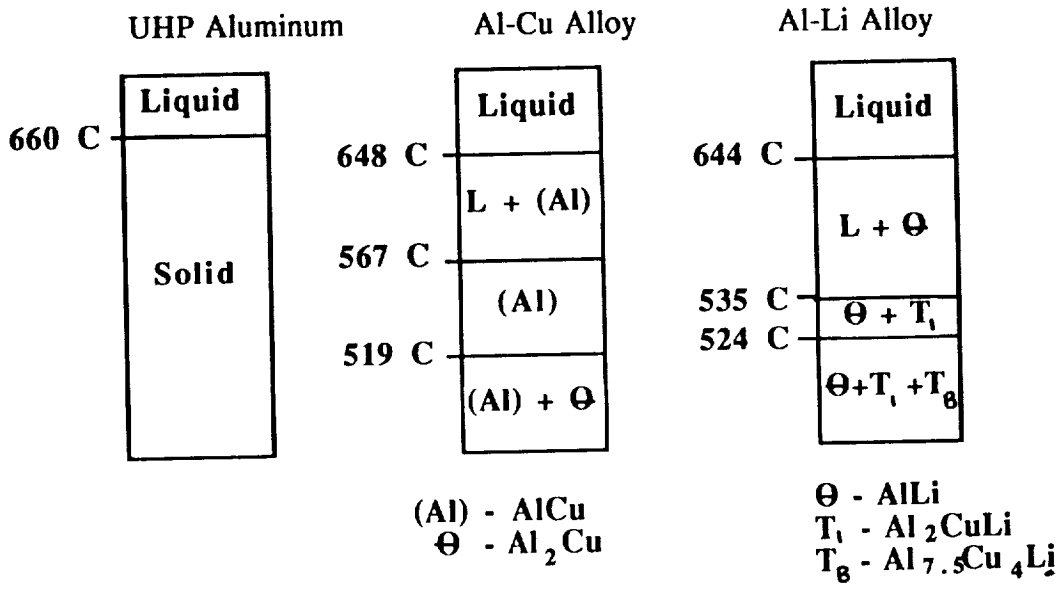

Figure 3.3 Temperature-phase relationships for experimental aluminum alloys [70].

Changing the full scale temperature range from 0-700°C to 500-700°C was accomplished with an operational amplifier in the differential input mode (Figures 3.2 and 3.4).

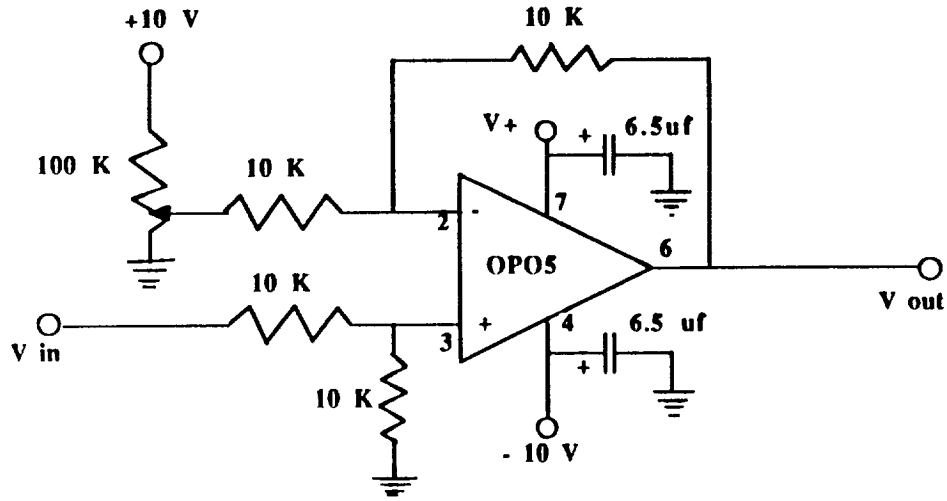

Figure 3.4 Circuit diagram of variable differential input operational amplifier.

By adjusting the variable input to remove 5 VDC from the Omni-Amp III's output, the full scale voltage output is reduced from 7 to 2 VDC. This corresponds to a change in full scale temperature range from 0-700°C to 500-700°C. In other words, a 500°C temperature at the input will produce 0 VDC at the amplifier output, whereas, a 700°C input will produce 2 VDC. Therefore, the range was 0-2 VDC displayed over 256 points on the D.S.O.'s vertical scale. The resolution, which improved from +/- 2.75°C to +/- 0.78°C, was adequate for detecting small changes in temperature. The output from the PM3335 D.S.O. was connected by an IEEE 488 bus to a microcomputer provided with ASYSTANT GPIB software from ASYST Software Technologies, Inc. A temperature versus voltage plot was made to determine potentiometer adjustments on the differential operational amplifier for temperature calibration. To accomplish this, the temperature was increased to 680°C then cooled to 500°C. Measurements were taken during both heating and cooling and it was found that the offset should be increased by 0.055 VDC to give 0 VDC at 500°C. Figure 3.5a illustrates the negative offset (-0.55 V DC = 500 C) before adjustment and Figure 3.5b shows the calibrated voltage-temperature relationship which provides between 0 V DC @ 500 C and 2.0 V DC @ 700 C.

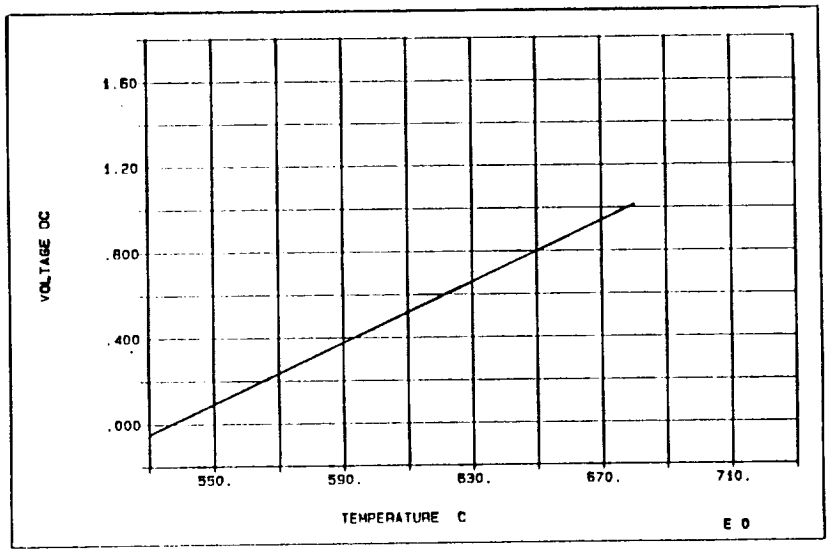

A

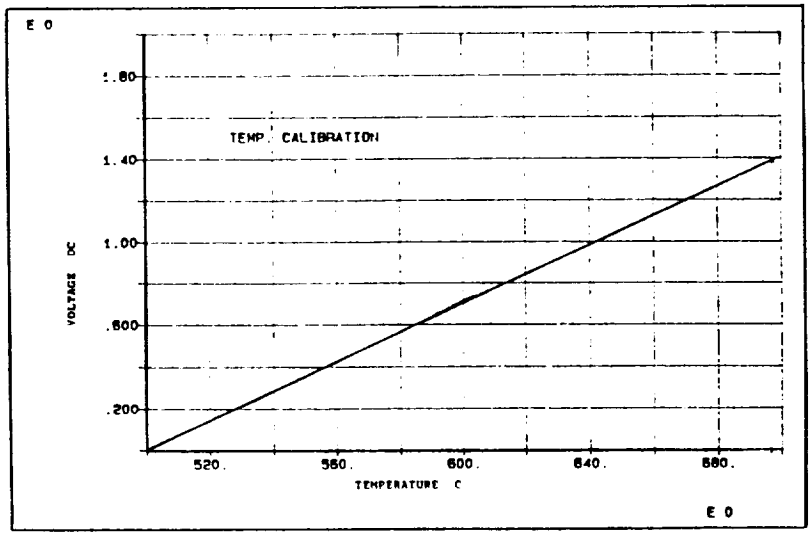

B

Figure 3.5 Temperature-voltage calibration plots (a) before and (b) after adjustment to 0 VDC at 500^{0}C illustrating the elimination of a -0.55 V DC offset by potentiometer adjustment.

The vertical resolution setting on the D.S.O. was also adjusted to 0.15 V/div. This provided a 1.2 V/ scan which, by refering to either Table 3.3 or Figure 3.5 permits a temperature range of 500-680°C to be displayed on the screen. A flow diagram using two example input voltages and their corresponding temperatures is shown in Figure 3.6.

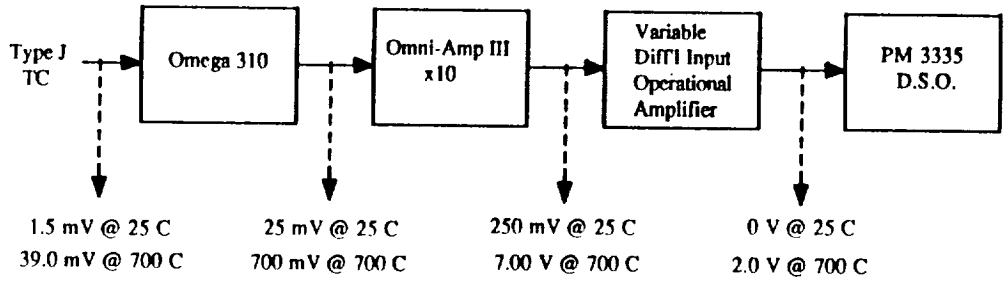

Figure 3.6 Flow diagram of voltage conditioning circuit to display thermocouple temperatures on a digital storage oscilloscope.

To insure that the thermocouple maintained contact with the casting as the machined aluminum pellet changed shape during melting, a stainless steel weight, an alumina sheath, and a boron nitride spacer were arranged as shown in Figure 3.7. As the metal melted and conformed to the shape of the crucible walls the boron nitride spacer maintained pressure on the melt thereby providing good coupling from the casting through to the transducer.

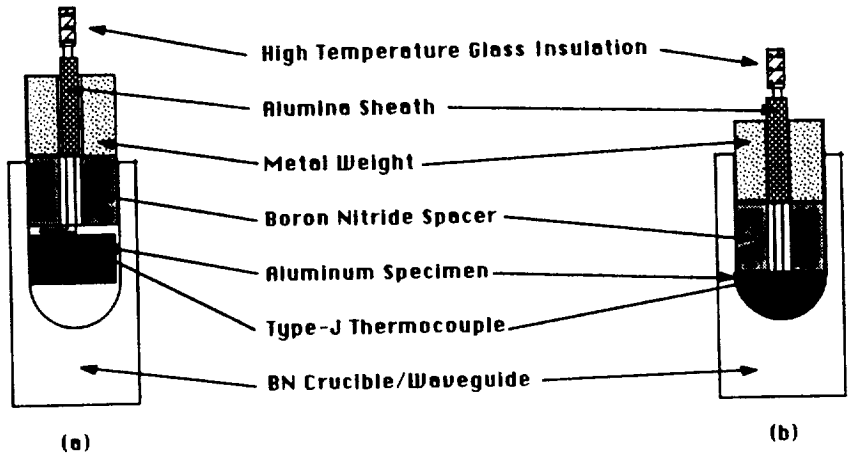

Figure 3.7 Thermocouple positioning (a) before and (b) after melting of the experimental aluminum alloy.

The use of a thermocouple to monitor the melt temperature caused problems in addition to requiring the new circuitry for improved resolution. A primary one involved selection of the proper wire gauge. When a thin gauge was used it was difficult to form a bead with the micro-torch without vaporizing the constantan prior to melting the iron. On the other hand, a heavy gauge thermocouple formed a large bead which remained on the top of the melt because of surface tension and, therefore, was not in full contact with the melt. As the furnace cooled the rigidity of the heavy gauge wires caused the casting to pull away from the crucible by tilting, thereby reducing acoustic emission coupling.

Since the cooling rates of the three materials were closely controlled it was decided that only a few of the tests would be temperature-monitored; the others were time-monitored. The time-monitored tests could then be plotted as a function of temperature, if necessary, using the time-temperature relationship of the cooling curve.

3.3.2 Acoustic Emission

The purpose of the rod, in addition to support for the crucible, was to act as an acoustic wave transmitter. Signals generated within the melt propagated through the crucible and rod to a cool region outside the furnace where heat would not damage the transducer. The maximum operating temperature of the transducers was 250^{0}C.

In early tests an alumina crucible was cemented using a high temperature silicate cement to various 12.7 mm diameter by 0.9 m long rods. Three rod materials were evaluated: 304 stainless steel, fused quartz, and copper. The fused quartz worked best since the coefficient of expansion was low and comparable to the alumina. The cemented interface, therefore, remained intact with the fused quartz but fractured during heating with the metal rods.

The transducer was coupled to the bottom of the rod using silicone adhesive. Surface displacements at the bottom of the rod, corresponding to AE signals in the melt, were converted by the piezoelectric transducer to low amplitude voltage signals. Depending on the transducer selected, a separate preamplifier, set at 60 dB, was sometimes necessary with either a 100 Khz high pass filter or a 1μf shunt capacitor added at the output of the preamplifier (Figure 3.8).

The final stage before digitizing the signals was the main amplifier. After several tests failed to show any acoustic emission signals during solidification the gain of the main amplifier was increased to 30 dB with the preamplifier set at 60 dB.

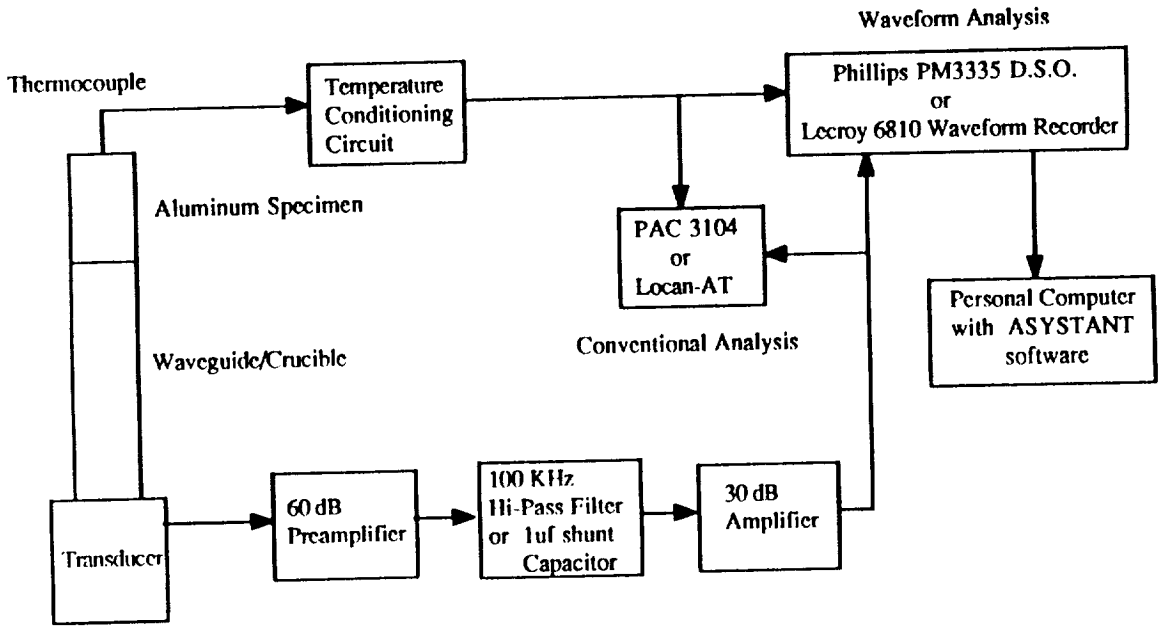

Figure 3.8 Diagram of experimental AE data acquisition system.

Conventional AE analysis was performed as discussed in Section 2.1.3b using only one of the four channels in a Physical Acoustics Corporation (PAC) Model 3104 AE Computer. The thumbwheel threshold setting was 0.5 V for most of the tests and the reasons will be described in detail later. The output of the Omni-Amp III amplifier was connected to the main parametric input of the PAC 3104 to record temperature. The conversion was 1.0 VDC/1000°C +/-20°C. This would permit plotting of acoustic

emission as a function of temperature although the resolution was not small enough to identify phase changes.

The following acoustic emission data was recorded for each test:

1. Hit Number,
2. Event Time,μs,
3. Duration, μs,
4. Counts, per hit,
5. Energy, V-s,
6. Peak Amplitude, dB,
7. Rise Time, μs,
8. Temperature, V/ ^{0}C.

The computer is capable of post-acquisition plotting of any combination of the above parameters in point, line, or histogram format and as either cumulative or non-cumulative plots. A numerical printout of all data, known as a dump, was another option.

Waveform analysis was performed by storing individual AE waveforms on the Phillips PM3335 D.S.O. and transferring them as digital arrays to the ASYSTANT GPIB waveform processing program through an IEEE 488 connection. A discussion of the digitizing method and its implications in frequency spectrum analysis was given in Section 2.1.3c, Waveform Analysis.

Typical settings of the PM3335 for the solidification tests are as follows.

1. Vertical Scaling - 0.5 V/div (eight division vertical scale permits display of full signal since signals do not generally exceed 4 V p-p).
2. Sweep Speed - 0.5 ms/div (twenty division horizontal scale permits fast fourier transformation to a 1 MHz bandwidth frequency spectrum).
3. Pre-trigger display - -2 div (shows 2 divisions of signal prior to triggering).
4. Trigger Level - 0.5 VDC (corresponds with threshold setting of PAC 3104; equivalent to one division).
5. Coupling - AC (removes any DC offset such as that caused by the 28 VDC phantom power required for the transducer with an integral preamplifier).
6. Mode - Digital (permits auto-, multiple, or single trigger and holds signal in memory until cleared).

Approximately ten signals were recorded for each solidification experiment at regular intervals during periods of strong AE activity. As described in Section 2.1.3c Waveform Analysis, the ASYSTANT GPIB program was used to calculate the power spectrum of each signal.

3.4 Metallographic Procedures

Preparation of specimens for metallographic examination included diamond saw cutting the small castings along the longitudinal axis, in most cases, but along the radial axis of a few other castings. One half of the specimen was then mounted in a catalytic-hardening epoxy resin. Before the resin cured, the specimen was placed in a vacuum chamber for ten minutes to extract air bubbles. After initial curing of eight hours, it was heated at 75°C for an additional two hours to ensure complete hardening. The mounted specimen was rough polished consecutively with 120, 240, 320, 400 and 600 grit silicon carbide papers. Intermediate polishing was done with 6 and 3 μm diamond paste in oil slurries for ninety seconds each. Final polishing was accomplished on stationary wheels with 1 and 0.3 μm alumina and 0.03 μm silicon dioxide in water slurries. At each of these three stations, the specimen was rotated clockwise for two minutes with reduced pressure during the last ten seconds. The specimen was cotton-swabbed in a water rinse, sprayed with alcohol, and hot air dried to prevent water spots. Vibratory polishing with cerium oxide was attempted in place of the silicon dioxide but resulted in corrosion, in the form of pitting, in all three aluminum materials. Magnesium oxide was also tried in place of the alumina, but scratching of the specimen face resulted.

Final preparation for optical metallography involved placing the specimen face up (Al-Cu and Al-Li alloys) or facing side (pure aluminum) in Keller's etch for five seconds, followed by a water rinse, alcohol spray, and hot air dry. The five second procedure was repeated until the desired microstructural surface relief was achieved. This included observation of dendrite arms, porosity, and second phases, if present. Overetching

resulted in a pitted and blackened surface that required repolishing. Specimens prepared for microstructural analysis were placed in a desiccator immediately after etching and were examined and photographed within hours of the preparation.

Optical metallographic analysis was performed on a Reichert-Jung MeF3 metallograph using cross-polarization and Normarski differential interference contrast (DIC). This provided exceptional resolution of microcracks and secondary phases. X-ray microprobe analysis was accomplished with a JEOL Model 733 Microprobe and a Tracor Model 5000 Digital Computer.

IV. RESULTS & DISCUSSION - ACOUSTIC EMISSION SIGNAL ANALYSIS

4.1 Introduction

A general objective of the present study was to monitor acoustic emission during the solidification of aluminum and aluminum-lithium alloys. More specifically, the intent was to develop models of the sources of AE and to characterize these signals so that the sources may be distinguished by their AE parameters. During the course of this work it was found, not unexpectedly, that the received signal at the detection network is a poor facsimile of the generated signal within the aluminum. The following discussion will describe in detail the causes for the variations in the signals and the methods that were undertaken to improve the repeatability.

Acoustic emission was found to be a useful tool in monitoring solidification. However, the key to its effective use is realizing that it should be a complementary rather than stand-alone method for solidification studies. In this study two other methods used were temperature monitoring and metallography. The first was critical in early tests to determine the solidification kinetics; the second provided post-facto information about possible acoustic emission sources. Results from both were correlated with the AE data to describe when the emissions were occurring and what the causes were.

The research was completed in three general, and many times overlapping, stages. The first was acquiring a thorough understanding of the effects of the experimental system on the recorded AE data. Changes in the AE data were found to be caused by electronic noise, mechanical impedances, and specimen geometries. The second stage involved experiments intended to induce suspected sources of acoustic emission,

specifically, grain formation, porosity and solidification cracking. The final stage compared metallographic and thermal data with the acoustic emission to identify the AE source mechanisms. The following sections are arranged in this pattern beginning with responses to known signals through known media and ending with practical models of AE sources from aluminum-lithium castings.

As stated, the intent of the first stage of research was to examine each major component in the AE signal path from generation to recording and to determine its effect in time and frequency domain on the original signal. The components included the transducer, waveguide, and amplification and data acquisition systems. Four transducers, three waveguides, two amplification and two data acquisition systems are discussed and compared. The purpose of the analysis was to develop an optimum combination of components for measuring acoustic emission during solidification of aluminum-lithium alloys. The effects of the transducer will be the first to be discussed.

4.2 Transducer Response

4.2.1 General

Acoustic emission transducers detect dynamic motion from AE events and convert these surface displacements to voltage-time signals. All subsequent analysis of the events are based on this converted signal. Therefore, a thorough understanding of changes that occur during this energy conversion is critical to AE source, ie., material defect characterization.

Although several types of transducers will be discussed, all those used were piezoelectric having a construction similar to Figure 4.1. All of the transducer networks include a preamplifier and a main amplifier. In one case the preamplifier is termed integral, within the housing, to preamplify the signal before subsequent noise is imposed. A 28 V DC voltage powers the preamplifier and AE signals from the transducer are superimposed on this DC offset as they travel to the main amplifier. There, the DC component is filtered out and the AE signal is amplified a second time. Frequency filtering may also be done at the preamplifier by adding a simple LC (inductive-capacitive) or shunt capacitive circuit. The usefulness of both a 100 kHz high-pass (100-H) filter and a 1 μf shunt capacitor will be discussed in a later section.

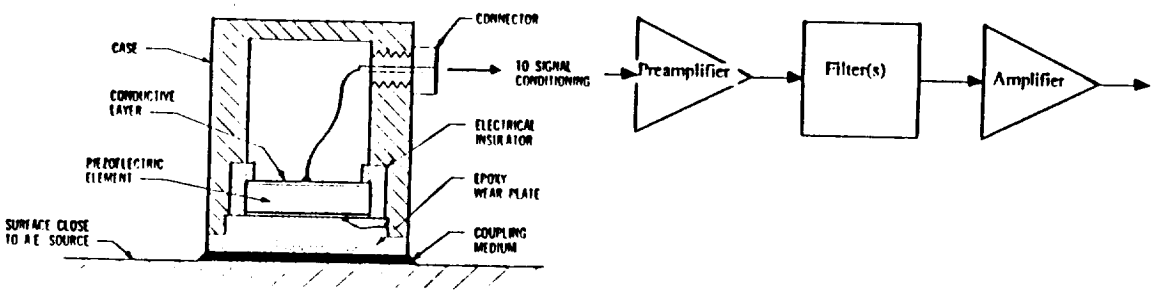

Figure 4.1 Schematic of piezoelectric transducer network coupled to a test specimen.

It has been suggested [71] that the coupling conditions strongly affect the reproducibility of the AE waveform. If the transducer coupling is poor or different couplants are used, the phase and amplitude components may be severely altered. Examples of changes in the frequency domain for different methods of coupling are shown in Figures 4.2 and 4.3. In an effort to reduce the number of variables, however, all present experiments were performed using silicone couplant with approximately 10 pounds of pressure and these effects were not considered.

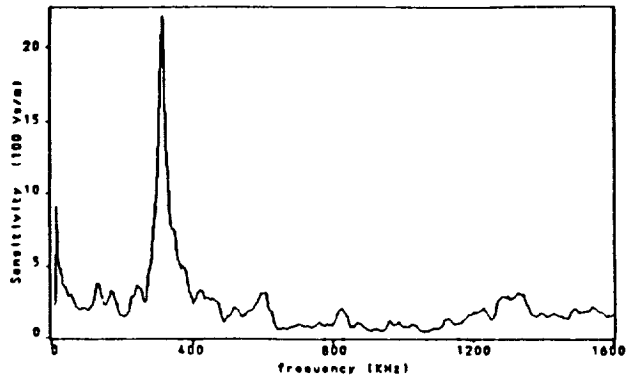

a

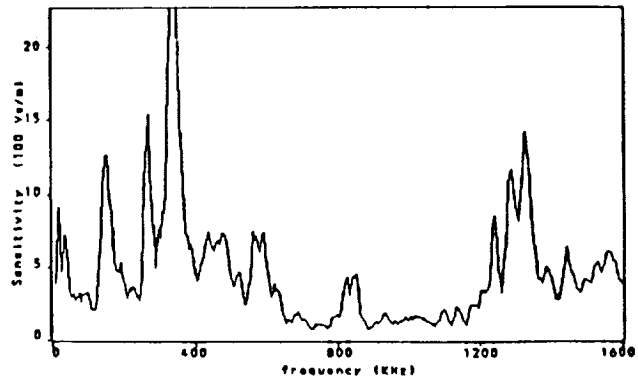

b

Figure 4.2 Frequency response from an AE signal by a (a) carefully and (b) loosely coupled transducer [71].

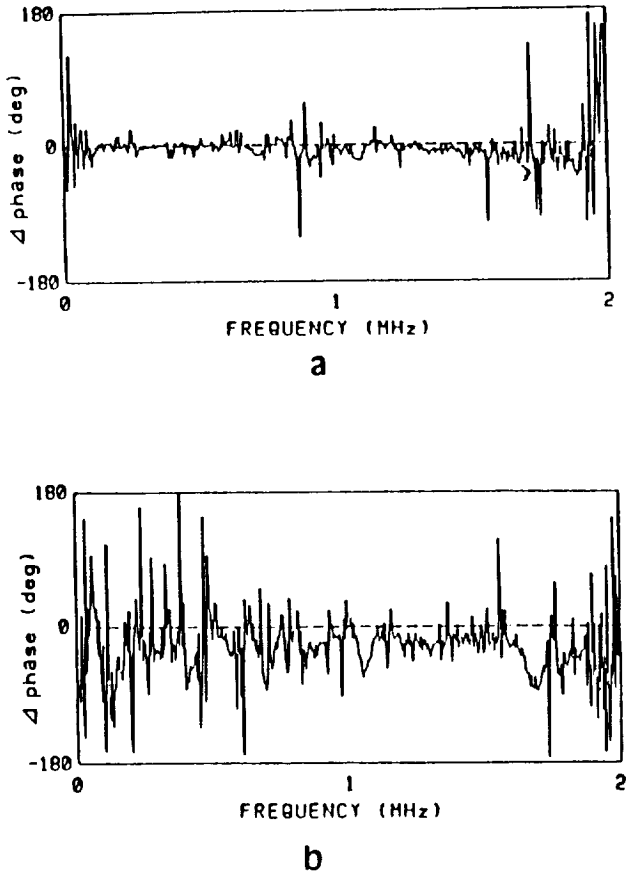

Figure 4.3 Frequency response from a common AE signal using (a) pine resin and (b) W400 couplant [71].

4.2.2 Transducer Characteristics

Three transducers were examined and compared to determine which would be most suitable for the solidification experiments.

1. The Model S2908, manufactured by Physical Acoustics Corporation (PAC), is classified as a broadband displacement-sensitive transducer. It has a typical operation range of 20-1000 kHz and a maximum operating temperature 121°C. Dimensions are 25.4 dia.x 25.4 Ht. mm. The housing and face materials are both 304 stainless steel.

2. The Model R15I, also a displacement-sensitive transducer from PAC, has a typical range of 100-450 kHz, an approximate resonant frequency of 160 kHz, an integral 40 dB preamplifier, and a maximum temperature of 110°C. Dimensions are 28.6 mm dia. x 31.1 mm Ht. The housing material is 304 stainless steel and the face plate is ceramic.

3. The Model VP-1093 Pinducer from Valpey-Fisher Corporation is described as a broadband velocity-sensitive transducer with a range of DC to 1.5 MHz. It has dimensions of 24 mm dia. x 33 mm Ht. with a small active crystal area of 13 mm dia. An internal brass barrel serves as a damping element behind the ceramic piezoelectric crystal. The housing is nickel-plated brass and there is no wear plate.

Figure 4.4 shows the time and frequency response of the S9208 to a constant amplitude 20 kHz-1.5 MHz swept sine surface vibration generated by an ultrasonic sending transducer coupled to the S9208 wear plate. The swept sine function is described in more detail in Section 4.2.3, Preamplifier and Filter Effects. A prominent

resonant peak is observed at 300 kHz on the fast fourier transform (Figure 4.4b) along with several other minor peaks. It should be noted that this is not the method of sensor calibration described in ASTM E1106 [72] but is simply a way of comparing sensor responses under similar conditions.

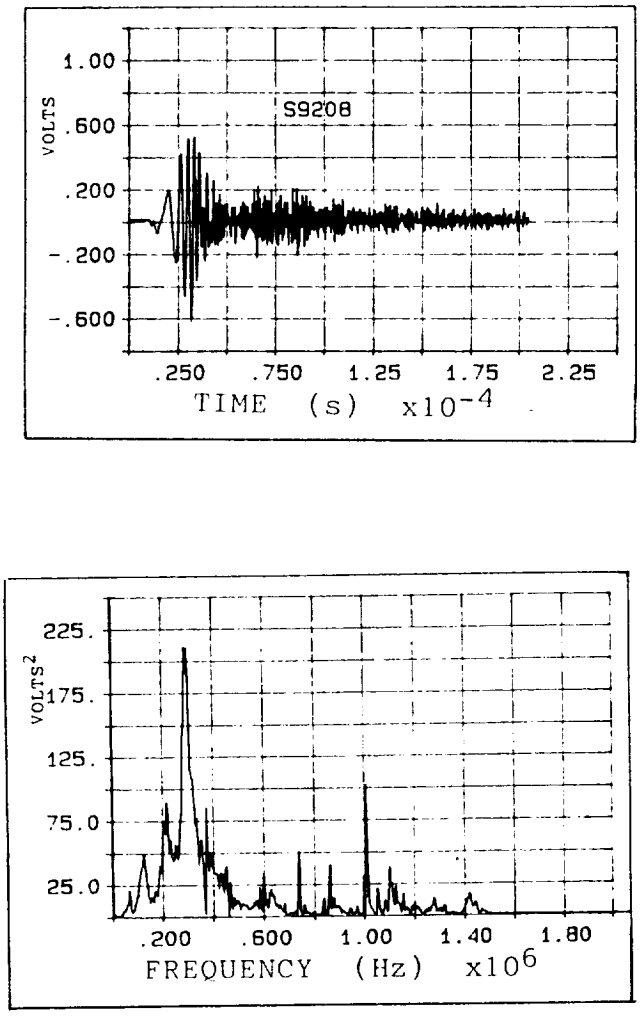

Figure 4.4 Time and frequency domain response of an S9208 broadband transducer to a 20 kHz - 1.5 MHz constant amplitude swept sine input function.

If the VP-1093 and R15I are analyzed in the same manner the latter can be seen in Figure 4.5 to have a strong resonant response at 160 kHz and the former (Figure 4.6) a virtually flat response up to 1.0 MHz. It should be remembered, however, that Figure 4.6 illustrates a power spectrum of a velocity-sensitive transducer. The amplitude response of the R15I is an order of magnitude higher than either the S9208 or the VP-1093 which are approximately the same. In all three tests, the total amplification of the signal was 40 dB with a 1 μf shunt capacitor at the output of the preamplifier.

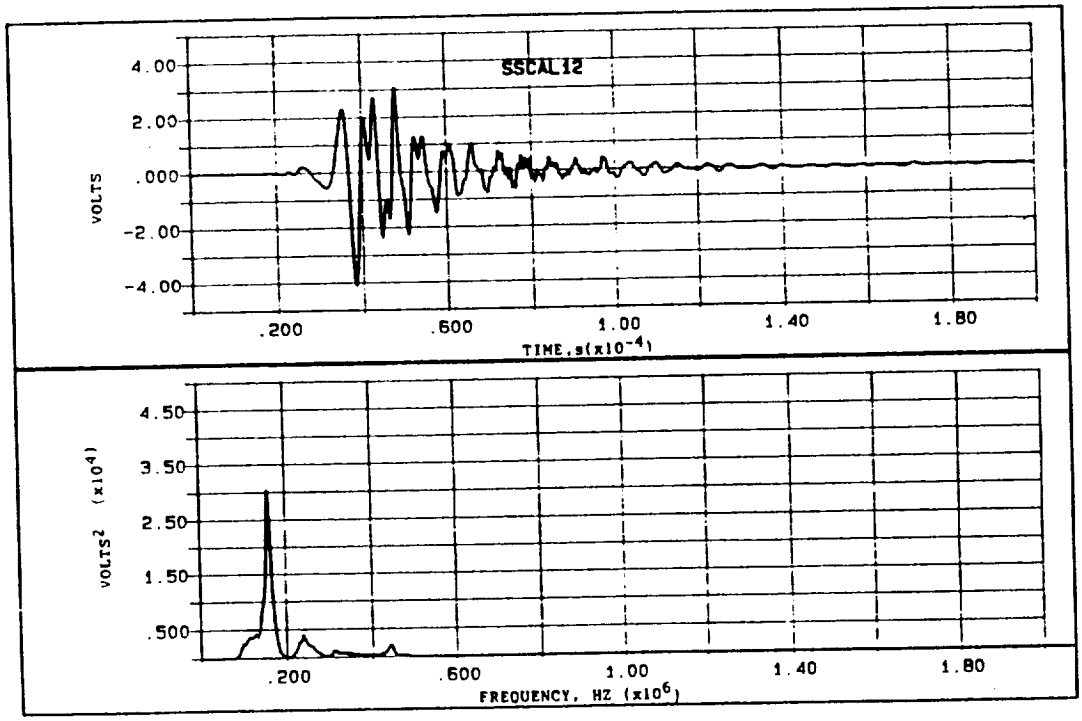

Figure 4.5 Time and frequency domain response of an R15I resonant to a 20 kHz - 1 MHz constant amplitude swept sine input function.

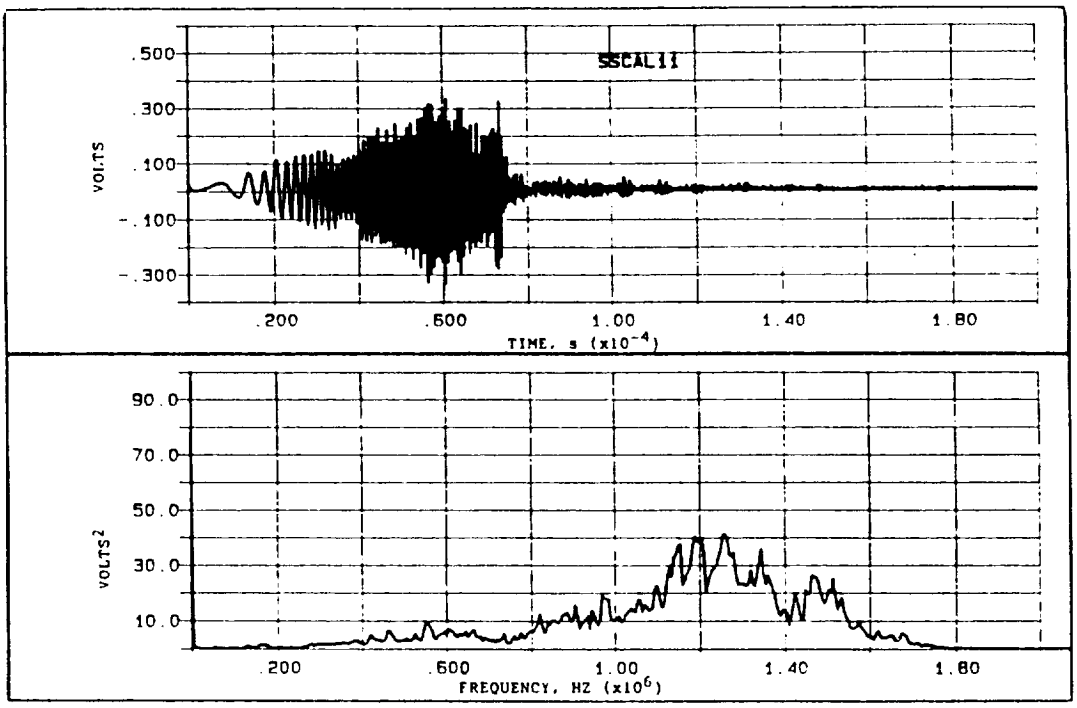

Figure 4.6 Time and frequency domain response of a VP-1093 broadband transducer to a 20 kHz - 2 MHz constant amplitude swept sine input function.

Sensor calibration was also done using pencil lead breaks as specified in ASTM E946 [73]on the free end of a round rod of compacted boron nitride powder having an HCP crystal structure. The other end of the rod was coupled to the transducer. For each of the three cases, two tests were done. The first used a 40 dB preamplifier with a 1 μf shunt capacitor; the second replaced the capacitor with a 100 kHz high pass filter, hereafter described as a 100-H filter.

Figure 4.7(a) is a plot in time and frequency domain of a pencil lead break transmitted through the BN rod to an S9208 transducer. Although Figure 4.4 shows it

to be a broadband sensor, the spectrum in Figure 4.7a is resonant at 8,000 Hz. As will be shown in Section 4.3, Waveguide Response, this is the resonant frequency of the BN rod. If the capacitor is replaced by the 100-H filter to suppress the resonance of the rod, then the 300 kHz resonant frequency of the transducer begins to appear (Figure 4.7(b)). No characteristic spectrum or waveform is apparent for the AE source. The plots are instead dependent on the geometry of the waveguide and the transfer function of the transducer.

A similar effect is seen using the VP-1093 pinducer. The plots in Figure 4.8(a) are from a system with a 1 μf capacitor in the preamplifier and those in Figure 4.8(b) with a 100-H filter. The resonance of the rod dominates in the former when the response is broadband. But as the low frequencies are suppressed in the latter, the response of the transducer appears. In the case of the resonant R15I transducer, the preamplifier is inside the sensor housing. No effect of the rod is seen (Figure 4.9) because of the strong resonant component at 160 kHz of the transducer.

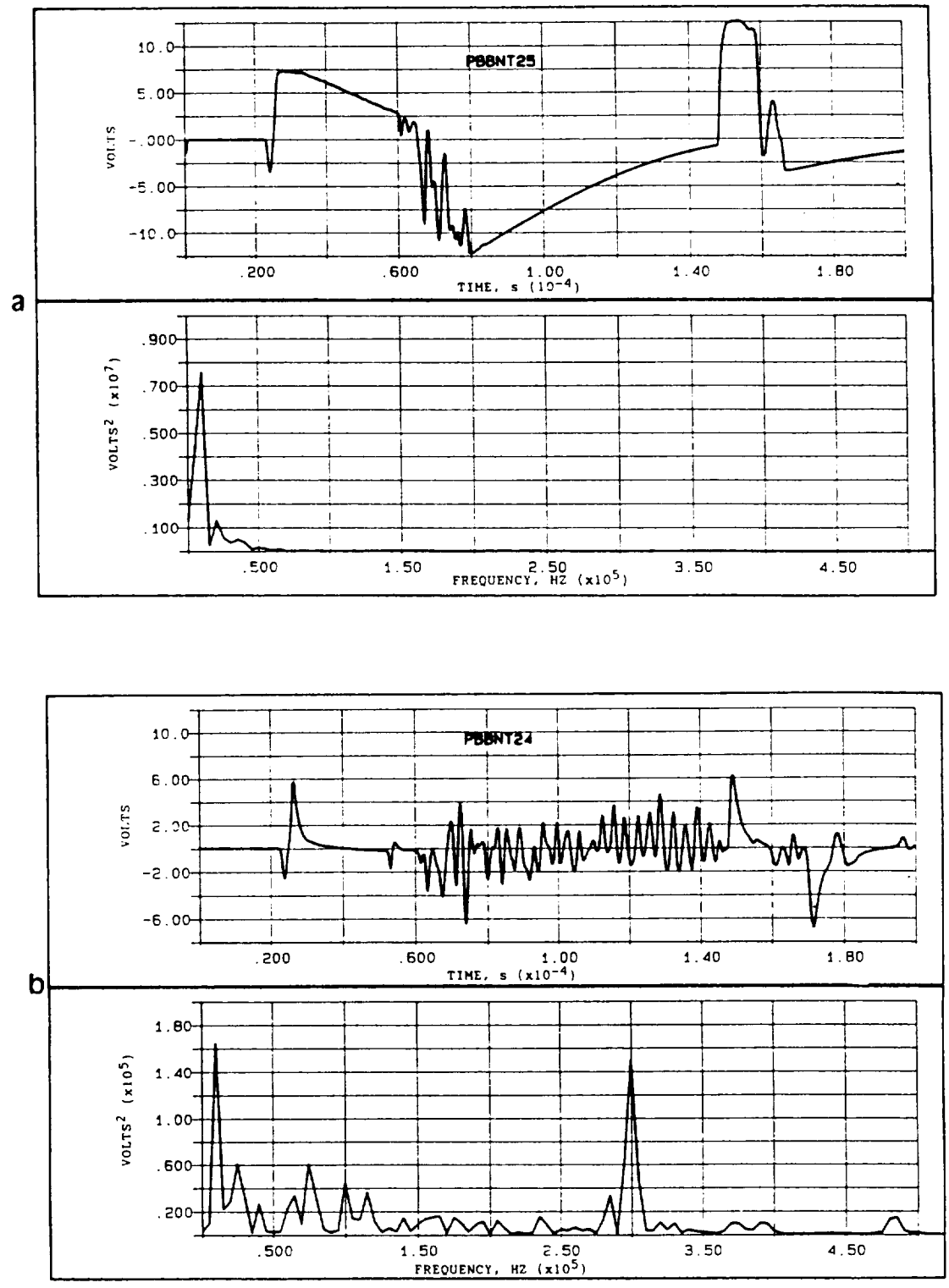

Figure 4.7 Time and frequency domain response to a pencil lead break of an S9208 transducer coupled to a BN rod using (a) a 1 μf shunt capacitor and (b) a 100-H filter.

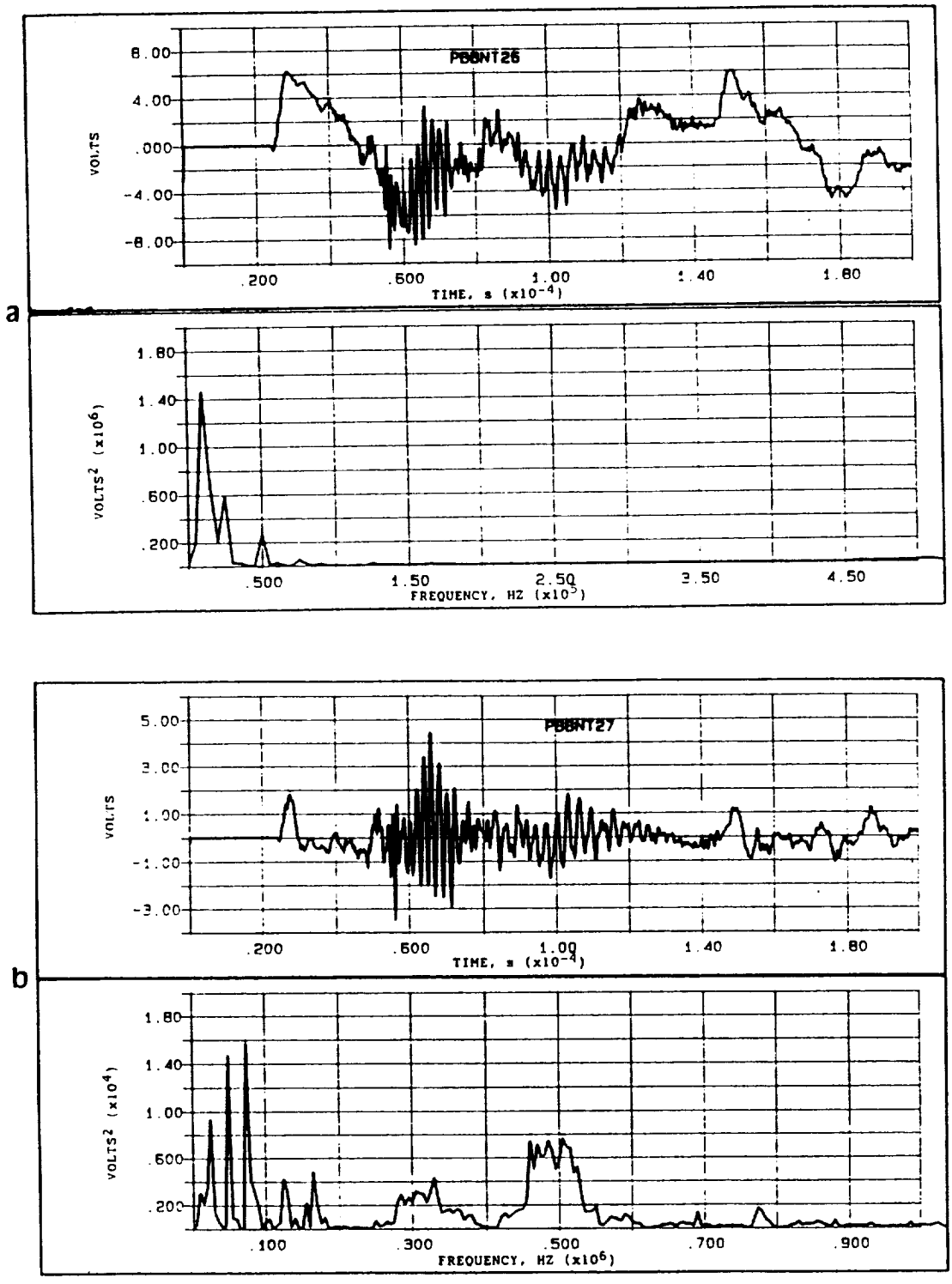

Figure 4.8 Time and frequency domain response to a pencil lead break of a VP-1093 pinducer coupled to a BN rod using (a) a 1 μf shunt capacitor and (b) a 100-H filter.

C-2

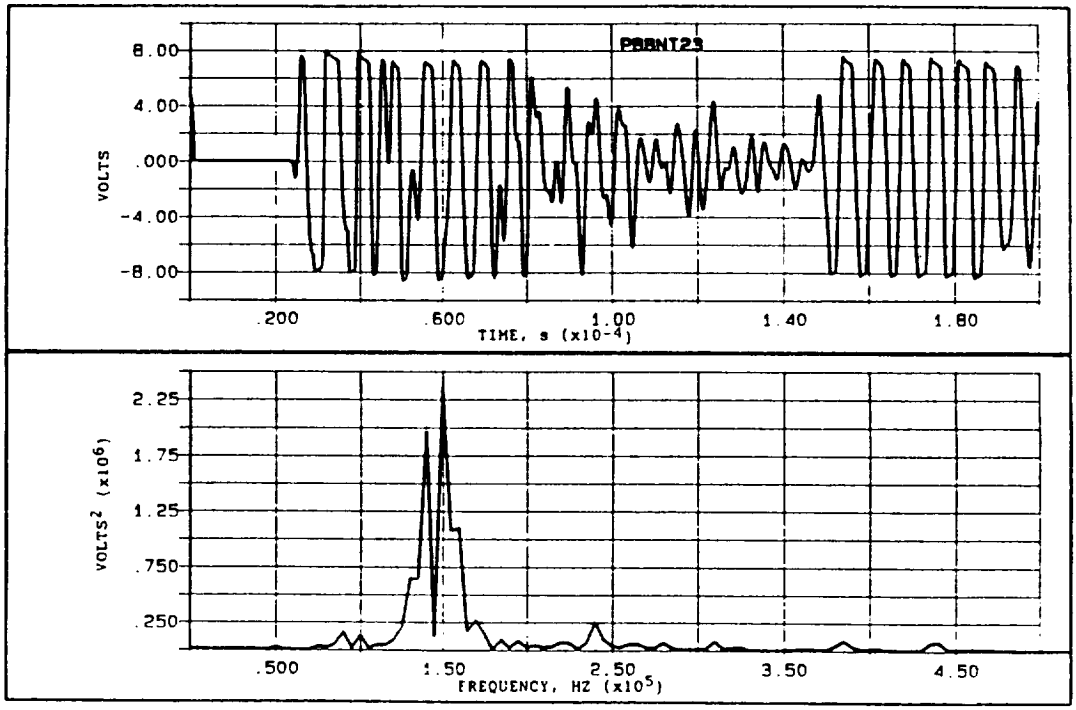

Figure 4.9 Time and frequency domain response to a pencil lead break of a R15I transducer coupled to a BN rod without filtering.

Although it may first seem as if each sensor responds differently to a common AE source and that all source characteristics are lost in the system transfer, a different examination reveals that this is not necessarily true. Recalling that the pinducer is velocity-sensitive and the S9208 is displacement-sensitive, the two responses may be compared by differentiating the S9208 response (Figure 4.10). Good agreement is shown during the initial part of the signal. A comparison in Figure 4.11 of the S9208 response versus a theoretical displacement, based on generalized ray theory [74], again shows

good agreement. Differences, however, are due to bandwidth limitations of the transducer since the large active area reduces high frequency response [75].

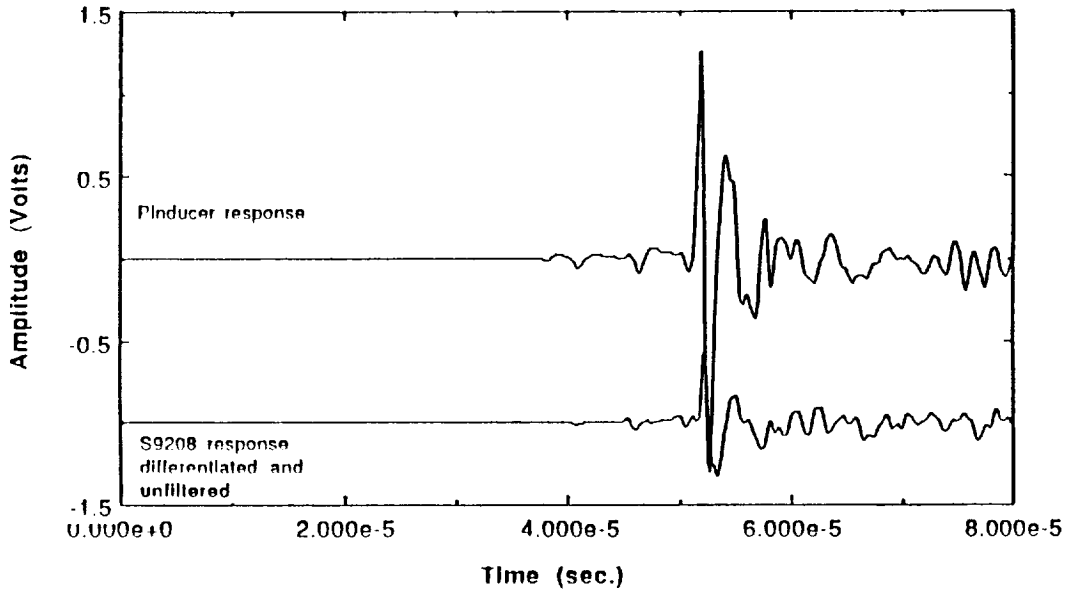

Figure 4.10 Comparison of an S9208 transducer and integrated VP-1093 pinducer response to a pencil lead break [75].

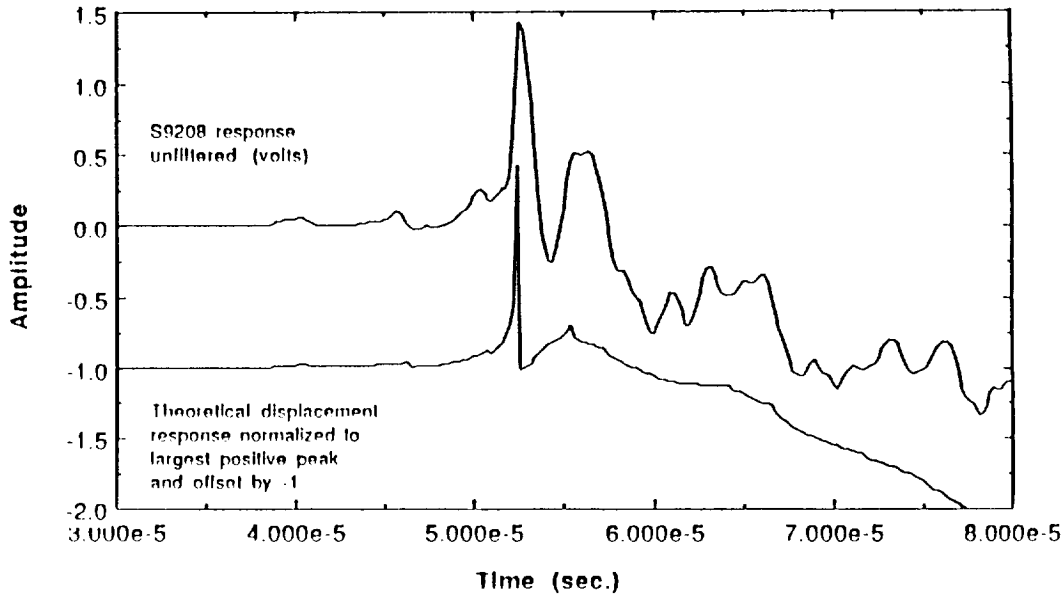

Figure 4.11 Comparison of an S9208 transducer response and a theoretical displacement response to a pencil lead break on the surface of a thick plate [75].

In summary, the choice of transducer for the solidification tests was reduced to the broadband S9208 and the VP-1093 pinducer. Although the R15I had a higher sensitivity, the frequency spectrum would consistently be a 160 kHz resonant peak with little useful information. The final choice was the S9208 since the signals would not have to be integrated and the mounting area of the crystal was the same as the waveguide.

4.2.3 Preamplifier and Filter Effects

The preamplifier and frequency filter, for this discussion, will be considered part of the transducer circuit. An effective method of measuring the response of these components to an input signal is the use of a swept sine function. This is a signal which increases linearly in frequency with time. In Figure 4.12 the rate of increase is 200 Khz/ms while the amplitude remains constant at 2 $V_{p\text{-}p}$. The time domain signal is shown in the center and the frequency domain in the lower left corner. The 10 Khz - 1 Mhz signal was generated with a Hewlett-Packard HP3314A function generator and recorded on a LeCroy 9400A digital storage oscilloscope. The frequency domain plot is a 25,000 point fast fourier transform (FFT) with a relative amplitude based on a LeCroy standard reference voltage. The horizontal scale is 200 kHz/div with the final frequency point at 6.25 div or 1.25 Mhz. Figure 4.12 shows that the result is an input signal that has a uniform amplitude with increasing frequency.

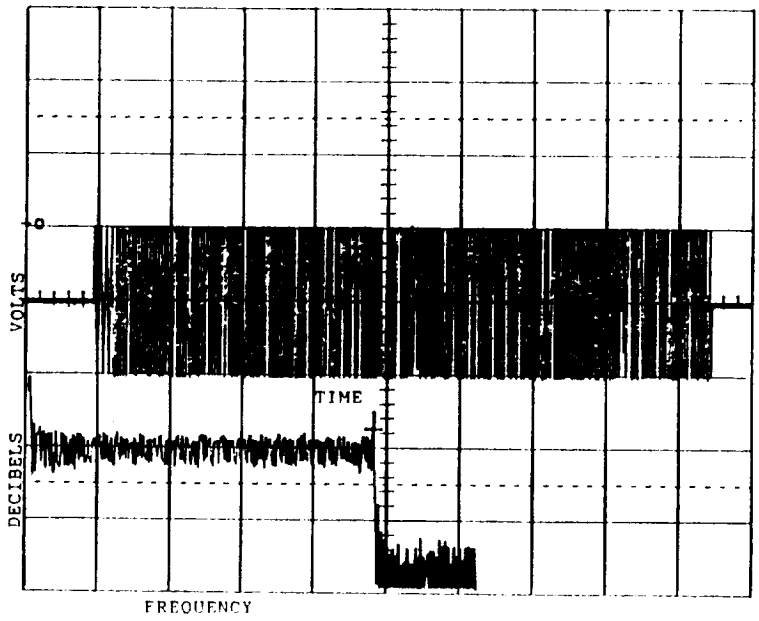

Figure 4.12 A constant amplitude swept sine function with a range of 10 kHz-1 MHz shown in time (center plot) and frequency (lower left plot) domains.

For direct comparison with Figure 4.12, the input signal was reduced in amplitude by a factor of 1,000 to 2 mV_{p-p} then coupled to a Physical Acoustics Corporation (PAC) Model 1220A pre-amplifier set at 60 dB (1,000x) with a 1 μf shunt capacitor. The output shown in Figure 4.13 shows that the preamplifier changes the flat input signal in two ways. Signal response below 100 kHz is distorted and approximately 0.6 V_{p-p} of electronic noise has been added. This is equivalent to 0.212 V_{RMS} or 46 dB. Therefore, although the frequency distortion is slight and is in a range typically below the bandwidth of AE transducers, the added noise requires that the threshold of the AE detection system be set above 46 dB or 0.25 V to avoid recording invalid signals.

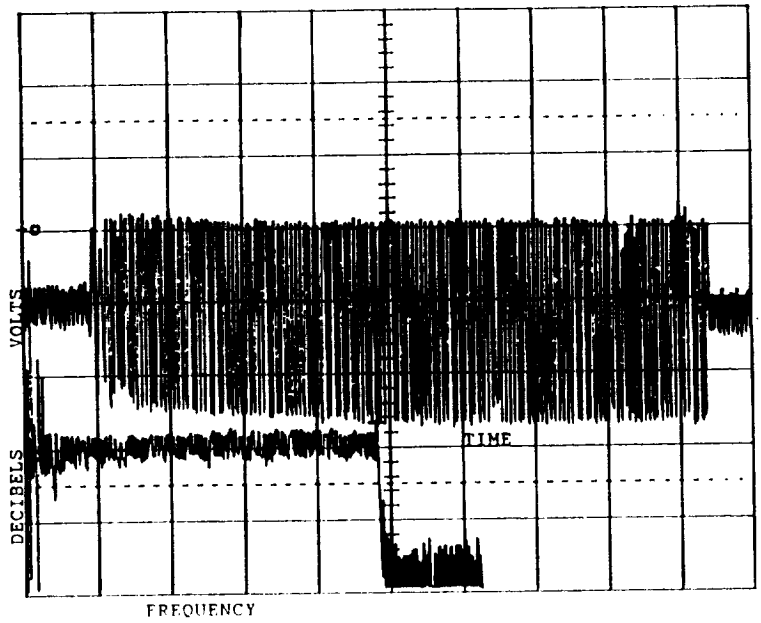

Figure 4.13 Time (center) and frequency (lower left) response of a 60 dB preamplifier with a 1 μf shunt capacitor to a 2 mV_{p-p} constant amplitude swept sine function in the range 10 kHz-1 MHz.

A 100-H high-pass filter was installed in place of the 1 μf capacitor to compare a filtered response of the preamplifier with the broadband response shown in Figure 4.14a. The filter was a two pole LC filter and a sharp cut-off was not expected. Figure 4.14b shows a flat response above 350 kHz with a gradual decrease in amplitude from 70 to 35 V at 100 kHz, ie., a 3 dB or 50% decrease, as required for a 100 kHz filter.

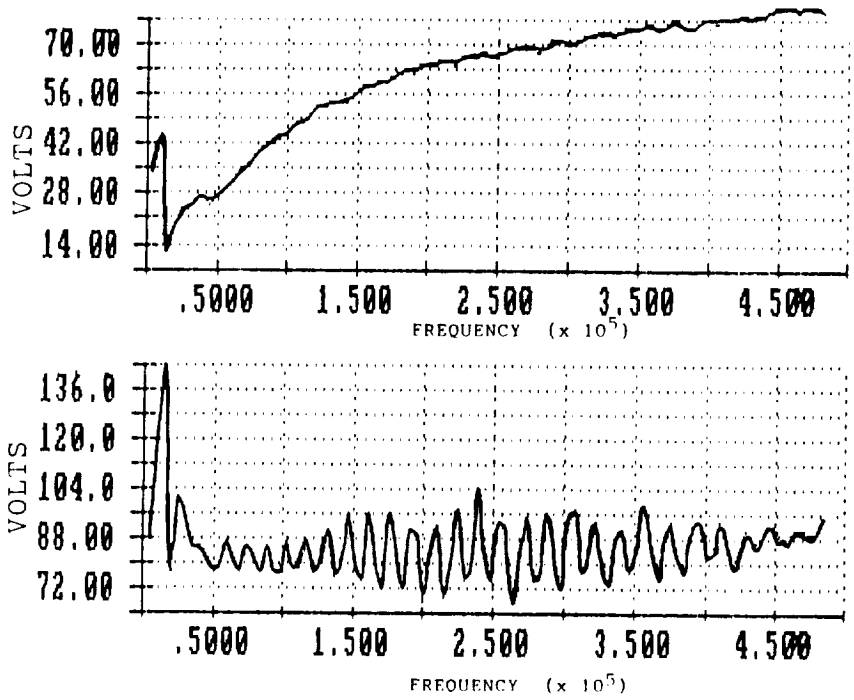

Figure 4.14 Frequency response of a 60 dB preamplifier with a 100 kHz high-pass filter (top) and with a 1 uf shunt capacitor (bottom) to a constant amplitude swept sine function.

It was found through the course of the work that it was important to observe low frequency components of the signal as well as high. Therefore, most of the experiments were conducted with the 1 μf shunt capacitor instead of the 100-H filter. Another important fact is that the LC filter only filters the signal between the transducer and the

main amplifier. Low frequency noise present at the wall outlet will enter the input line of the measuring and detection circuits and will be superimposed on the AE signal at the main amplifier input or thereafter before being stored.

Line noise was a severe problem in the solidification laboratory. Large generators, HVAC (heating, ventilation, air-conditioning) equipment, and rotating machinery in the building resulted in random inductive spikes, line voltage fluctuations, electro-magnetic interference (EMI), and low frequency hums to occur at random. The 100-H filter was ineffective at reducing any of this noise. Therefore, steps taken to reduce this interference included using an isolation transformer, choke filter, foil-wrapped wires, and also testing during the night. It should be noted that a "quiet" line was available in another laboratory for the calibration and system response tests. A more detailed discussion of noise generated within the measurement system will be given in Section 4.4, System Noise.

4.3 Waveguide Response

The selection and design of the crucible and waveguide was paramount to the success of this study. The ideal design would transfer acoustic emission signals from the solidifying metal to the transducer without any distortion of the waveform. At the least its effect on the signal should be discernible and minimal. In the beginning, the crucible and waveguide were considered to be two components that would be coupled prior to testing.

The choice of crucible material was limited to either graphite or boron nitride because of its contact with a molten aluminum-lithium alloy. In a conversation with personnel

at the Alcoa Technical Center [76], it was learned that these are the only proven materials which do not react with or alter the composition of the Al-Li alloys. Their recommendation was boron nitride since it is virtually inert and is not wetted by the molten Al-Li alloys. The low coefficient of friction and the non-wetting feature of BN would prove it to be an ideal crucible material for an acoustic emission study since it would not add frictional noise during shrinkage of the casting.

As stated in Section 3.3.2 three waveguide materials were initially investigated: fused quartz, copper, and boron nitride. It was decided that the initial geometry would be a 1.3 mm dia.x 30 cm long round bar. Comparisons of signal responses were done by coupling each to an S9208 transducer and performing standard pencil lead breaks on the opposite end.

4.3.1 Boron Nitride Rod Response

It was informative to observe the response of the S9208 transducer to a single cycle 100 kHz sine wave because the changes to a known waveshape can readily be seen. The top waveform of Figure 4.15b shows the input signal to a sending transducer and the lower waveform is the output from a preamplified S9208 coupled to it (Figure 4.15a). The ringing due to reflections within the sending and receiving transducer crystals is obvious. The original sine wave does not appear distorted or dispersed.

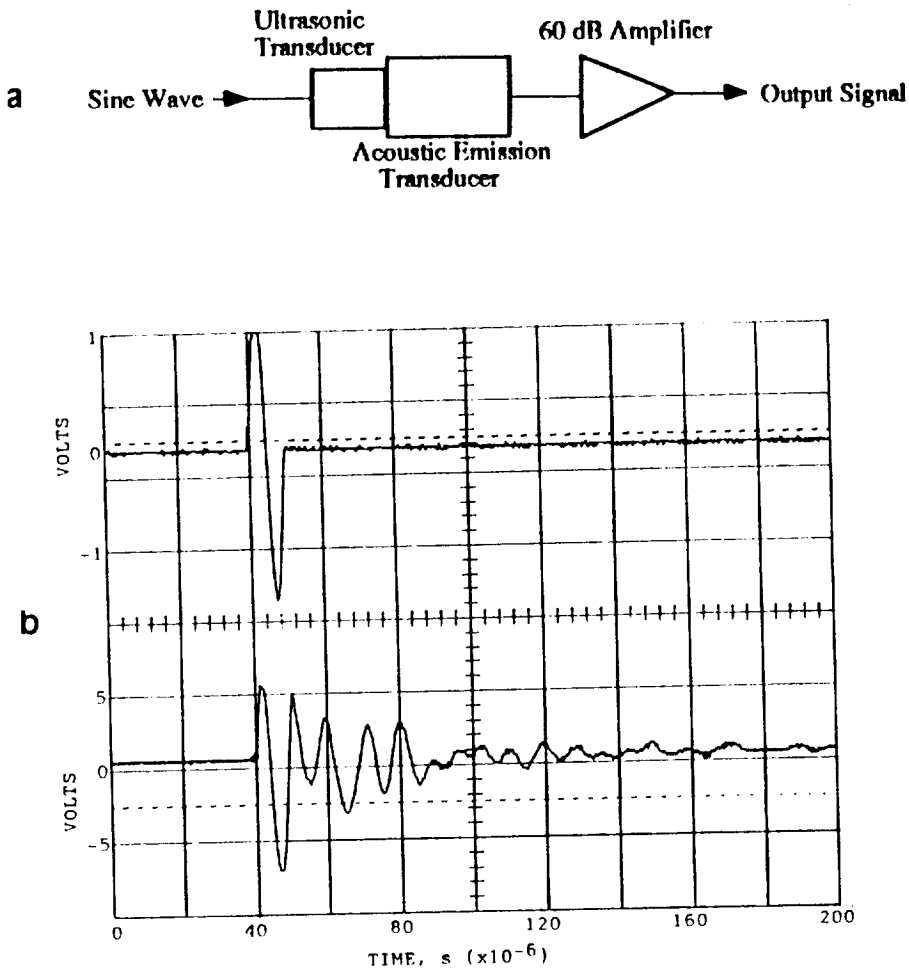

Figure 4.15 (a) The coupling arrangement of an ultrasonic transducer and a broadband acoustic emission transducer to observe: (b) the response (bottom plot) to a single cycle sine wave (top plot) after 60 dB amplification.

At first it may seem that little attenuation has occured. However, input voltage was transformed to mechanical energy by the sender, transferred across a couplant to the receiver, converted back to an electrical signal, and amplified 60 dB. Close attention to

the vertical scales (Channel 1 at top: 1 V/div and Channel 2 at bottom: 5V/div) shows that the 2 V peak-peak amplitude of the input signal has decreased to an output of 12 mV peak-peak, before amplification.

The added effect of introducing a boron nitride rod between the sending and receiving transducers is shown in Figure 4.16. The output has been displaced by 66.4 μs from the input. Therefore, since a 30.5 cm rod was used, the longitudinal (p-wave) velocity of boron nitride has been calculated to be 4,590 m/s. A time displacement of 131.9 μs was measured to the first reflection (not shown) and the velocity for a round trip of 61.0 cm is 4,622 m/s. From these measurements an average longitudinal mode velocity for boron nitride was determined to be 4,600 m/s.

It can be seen by comparing the outputs with and without the BN rod that the frequency and amplitude are virtually unchanged except for the time delay (see Figure 4.15 and 4.16). Damping of the third and fourth cycle is greater with the rod although the effect is minimal. It should be noted that the 100 kHz single sine wave input may be considered a low ultrasonic frequency and higher frequencies may be attenuated to a greater degree.

A more practical acoustic emission source calibration signal than the sine wave is the pencil lead break in accordance with ASTM E976 [73]. Figure 4.17 is a plot showing the response of an S9208 transducer and BN rod to a lead break on the free end of the rod. The upper figure is a time expansion (10 μs/div) of the first two peaks in the lower figure (50 μs/div).

a

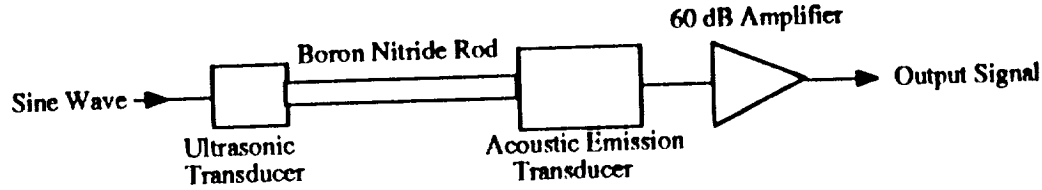

b

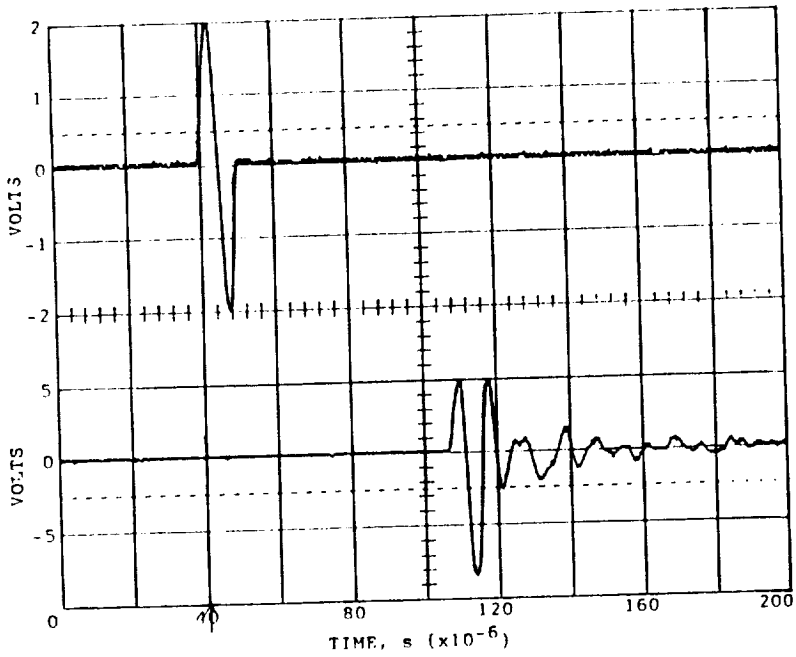

Figure 4.16 (a) The coupling arrangement of an ultrasonic transducer, a BN rod and a broadband acoustic emission transducer to observe: (b) the response of the rod (bottom plot) to a single cycle sine wave (top plot) after 60 dB amplification.

a

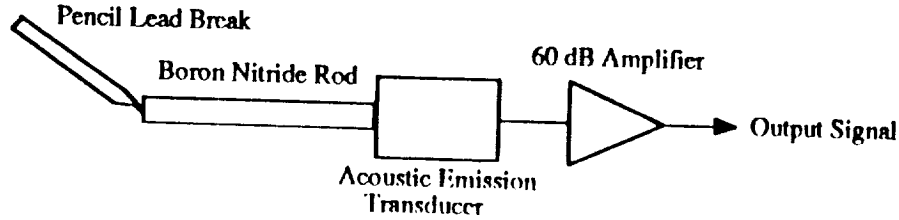

b

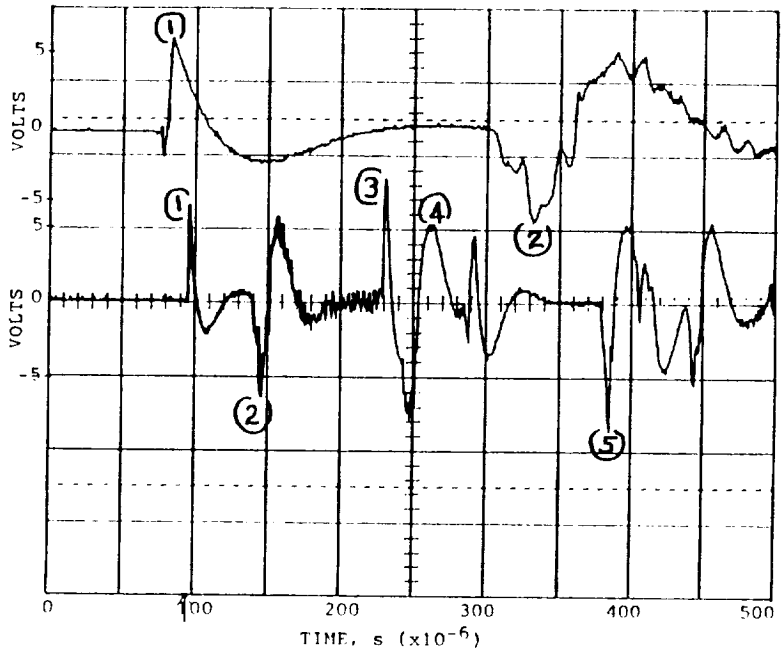

Figure 4.17 (a) The coupling arrangement of a BN rod and a broadband transducer to observe: (b) the response to a pencil lead break (lower plot) on the free end of the rod and a time expansion of the first two peaks (upper plot). (1) indicates arrival of first extensional mode wave, (2) the first flexural mode wave, (3) a reflection of the extensional wave, (4) the first surface wave, and (5) a reflection of the flexural wave.

The 133 μs time difference between the first and third peaks of the lower plot indicates that the latter is a reflected wave of the former. It is in close agreement with the 131.9 μs time difference for the previously discussed sine wave response. Since this is the response to a downward source aimed at the transducer it is reasonable to assume that the first peak is the arrival of the longitudinal mode wave. If it is also assumed that the second peak, which is displaced from the first by 44 μs, is the flexural mode or shear wave velocity may be calculated

$$30.5 \text{ cm}/(66.4 + 44 \text{ μs}) \times 0.01 \text{ m/cm} = 2{,}760 \text{ m/s}$$

which is 60% of the longitudinal velocity. Peak #4 is not a reflection of the flexural wave since the time difference is too short. It may either be the tail end of the extensional reflection or the arrival of a new mode, the first surface wave. Peak #5, however, has the correct time difference to be a reflection of the slower velocity flexural wave.

Rise times of 1 to 5 μs and durations of 30 to 40 μs were recorded for the various modes. Therefore, an oscilloscope setting of 20 μs was determined to be appropriate for detailed observation of AE waveforms during solidification of aluminum and its alloys.

A consequence of determining the wave velocity of the BN bar and knowing its geometry is the ability to calculate its resonant frequency. Since 1.9 cm was bored from the end to form a crucible the effective length was 28.6 cm. Using the simple relationship for the resonance of a bar [77]

$$nf = v / (2 \times L) \qquad \text{(Equation 7)}$$

where: n = wave number f = frequency

v = wave velocity L = length of rod

the fundamental resonant frequency for a boron nitride rod is 8,050 Hz with the first and second harmonics being 16,100 and 24,150 Hz, respectively.

4.4 System Noise

Since an objective of the present study was AE source characterization, it was important to understand which part of the signal was acoustic emission and which part was noise. A simple set of tests was performed which clearly shows the noise contribution of each system component and how it affects an actual AE test signal.

Figure 4.18 is a plot of noise generated directly from a 13 mm dia. x 30 cm long boron nitride rod sitting vertically on a PAC Model S9208 transducer. As described in Experimental Procedures this is the test arrangement for solidification. The BN rod was bored at the top end to provide an integral casting crucible. It was coupled to the transducer using silicone adhesive. The output of the transducer was sent directly to the oscilloscope. Therefore, it is a plot of noise generated by the piezoelectric crystal itself along with mechanical resonance of the rod and transducer casing. Although the RMS voltage is less than 0.005 V the frequency spectrum shows low frequency components of 60 and 120 Hz from EMI fields generated by nearby machinery. There was also an 800 Hz component which was thought to be mechanical resonance from small vibrations on the testing table.

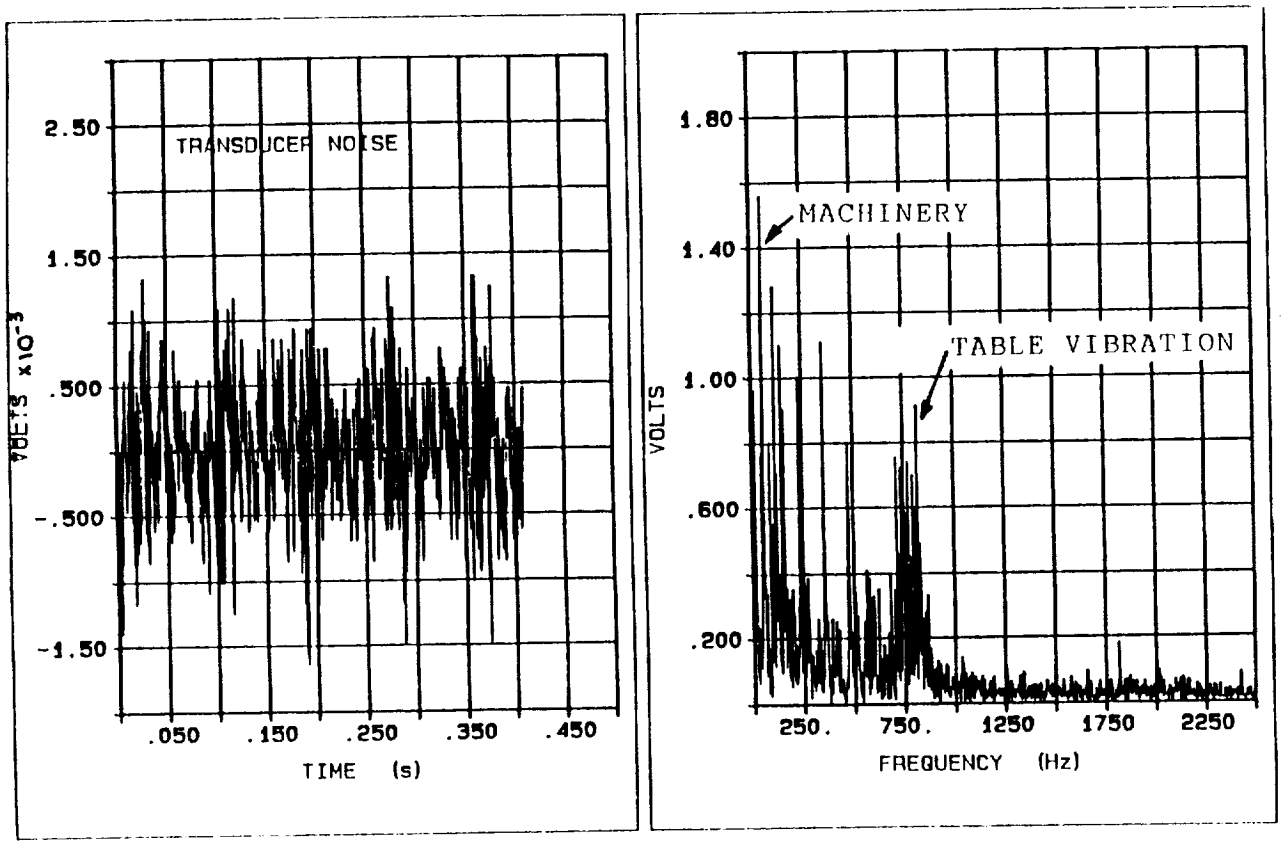

Figure 4.18 Plots of noise generated by a coupled S9208 transducer and BN rod in time and frequency domains.

The above arrangement was modified by connecting a PAC 1220A preamplifier with a 1 μf shunt capacitor to the output of the S9208. The 1220A preamplifier output was coupled to a PAC 3104 AE data recorder with the main amplifier set at 0 dB gain. As shown in Figure 4.19, the noise has increased by an order of magnitude but the 800 Hz resonance seen in the preceding figure is now masked. A strong 120 Hz component is observed as a result of inductive motors operating at the time of test in another part of

the building. The noise from the machinery had been transmitted through the power line into the 3104 and was superimposed on the recorded signal. Without the careful use of an oscilloscope or spectrum analyzer at the time of testing, this interference may have been recorded as valid acoustic emission data. Because of this observation, each test thereafter was examined for this component and the results were invalidated if present.

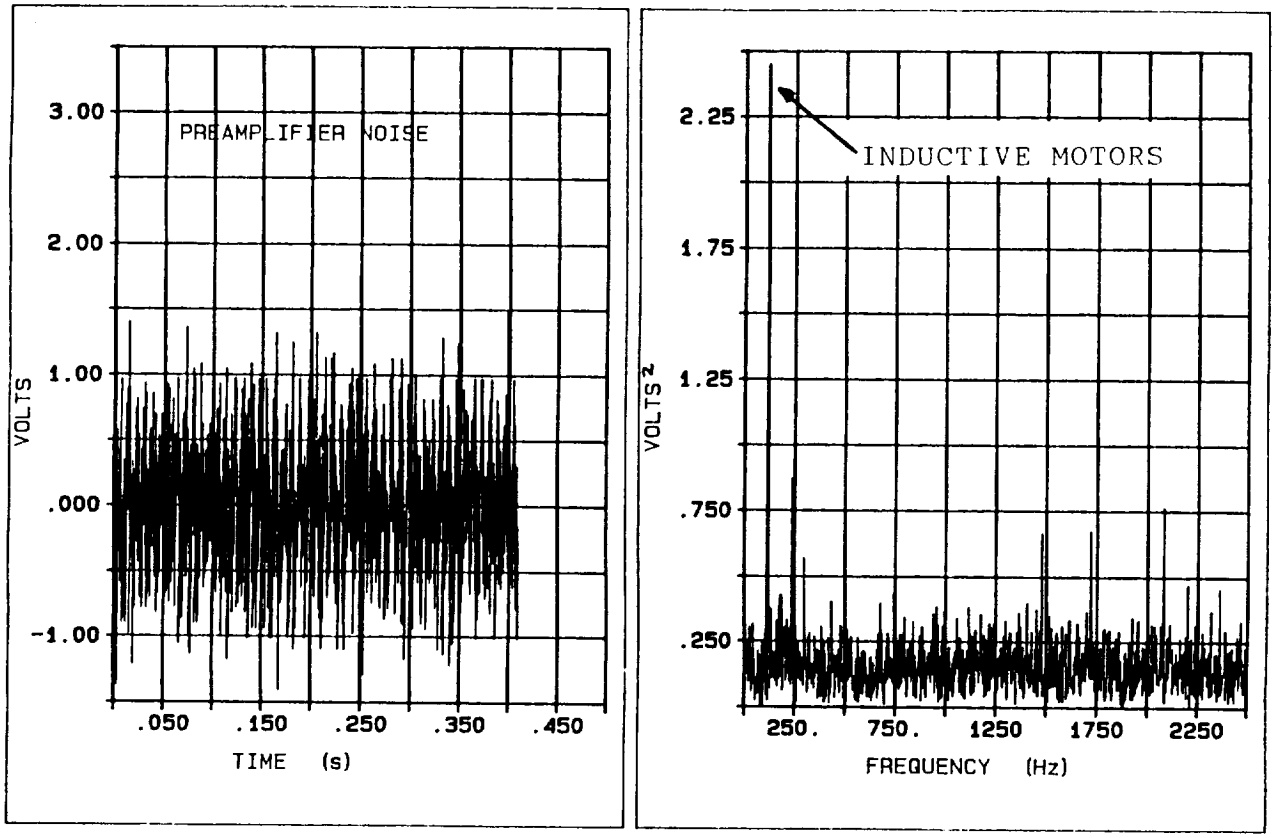

Figure 4.19 Plots of noise generated by a coupled S9208 transducer, BN rod, and preamplifier in the time and frequency domains.

As the main amplifier setting was increased to 30 dB, the noise increased to an RMS level of approximately 0.07 V as shown in Figure 4.20. This is the total system noise for a solidification experiment. The machinery was not active and the 120 Hz noise was not present during this test. The frequency spectrum shows it to be essentially white noise with the exception of an unidentified 2,000 Hz component. Based on this information, a threshold setting of 0.5 V DC was selected for all solidification experiments.

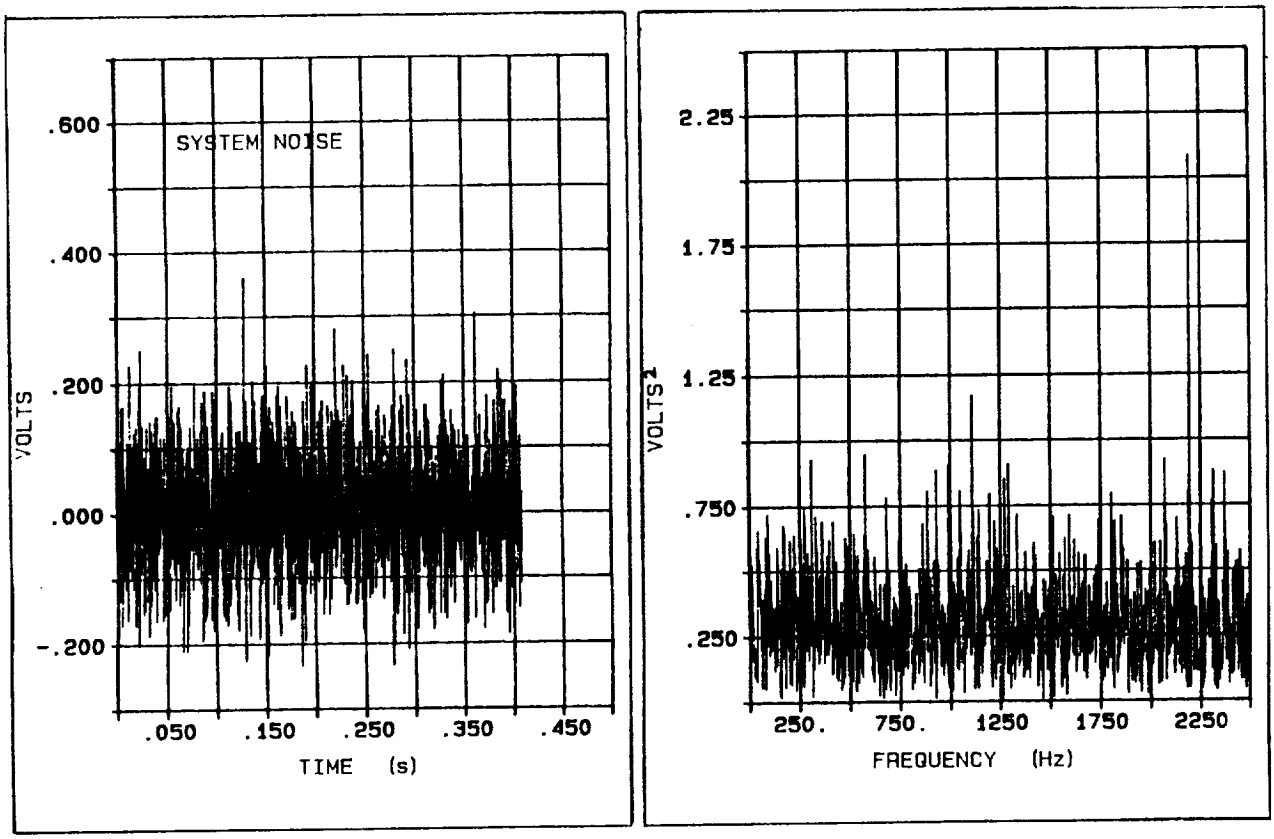

Figure 4.20 Plots of a typical AE signal during solidification illustrating the presence of system noise in the time and frequency domains.

An example of the contribution of noise to the recorded acoustic emission signal is shown in Figure 4.21. The plot is an actual signal recorded during melting of the aluminum in the system described above. The system noise may have a significant effect on the shape of the waveform in the time domain. However, in the frequency domain, the low frequency noise components and the white noise do not interfere with observing the prominent AE frequency components. In this case there is a fundamental peak at 9,200 Hz as shown in the expanded frequency plot (Figure 4.22) which corresponds to the resonant frequency of the boron nitride rod. This was described in more detail in Section 4.3.1, Waveguide Response.

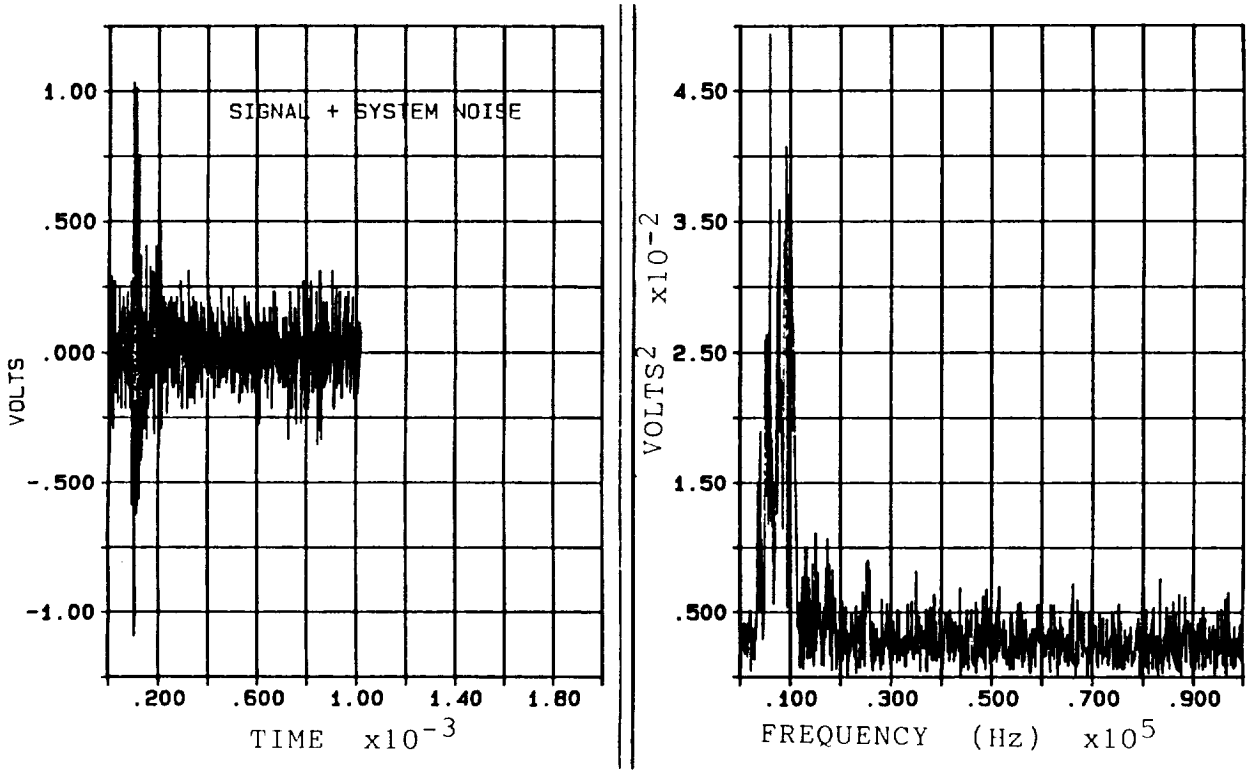

Figure 4.21 Plots of a typical AE signal during solidification illustrating the presence of system noise in the time and frequency domains.

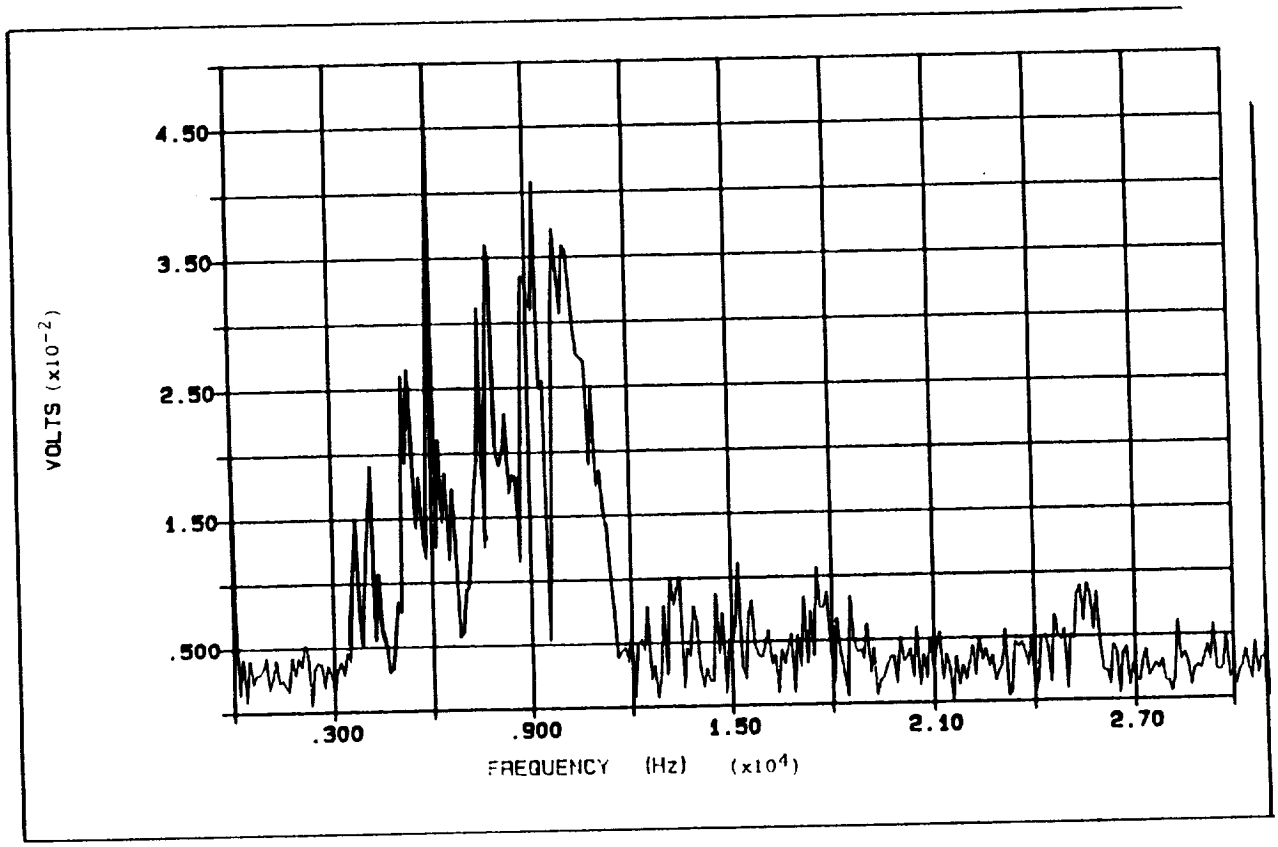

Figure 4.22 Expanded frequency plot of signal and noise shown in Figure 4.21.

4.5 Summary of AE System Response

This Section has provided a detailed discussion based on the response of acoustic emission signals to transducers, waveguides, and noise. Transducer coupling pressure and materials were investigated; silicone adhesive at 10 psi pressure was selected as the standard. Boron nitride was the choice as a primary crucible material because of its low friction and non-wetting features; alumina was used in alternate tests for comparison. A round rod made with an integral crucible was chosen as a waveguide joining the melt

to the transducer. The length was adjusted to provide thermal isolation from the furnace and to provide a low frequency resonance that is generally below the bandwidth of transducers. A broadband displacement-sensitive transducer was selected for its unique combination of properties.

The swept sine function was used not only for demonstrating system component response but also to show distortions caused by the amplification circuits. The effectiveness of the high-pass filter was displayed using this function. Pencil lead breaks were used in a similar manner as a calibrated acoustic emission source for determining the transfer functions of the system components.

It has been shown that considerable noise has been added to the signal as a result of the measurement system. The frequency domain representation of a signal clearly displays the mechanical resonance contributions of the waveguide and transducer. The source components are overwhelmed by these effects and are difficult to distinguish unless the low frequency resonance is filtered. Unfortunately, the low frequency components contain the majority of the signal power and filtering them leaves a weak signal that may be below the noise level. It was decided that (a) a high-pass filtering would be used for source characterization using waveform processing and (b) broadband detection, i.e., no filtering, would be used for maximum sensitivity to solidification signals.

V. EXPERIMENTAL RESULTS & DISCUSSION: AE During Solidification

5.1 Introduction

As described in Section IV, the system for measuring acoustic emission during solidification of aluminum-lithium alloys has been optimized by selecting a crucible, waveguide, transducer, and recording equipment that will transmit the amplified signals with a minimum of added noise, distortion, interference, or attenuation. Two methods of AE data acquisition were employed; simultaneously, in many cases. These include the conventional method (Section 2.1.3b) and the waveform analysis method (Section 2.1.3c).

The former method would record all signals above a preset threshold but store only specific information about each event. Data such as the cumulative number of hits was extremely useful in presenting acoustic emission activity as a function of time or temperature. However, other parameters which are based on signal intensity or length (eg. duration, rise time and amplitude), provided little information on understanding the solidification mechanisms or identifying sources of AE.

The latter method, waveform analysis, would record only specific signals but stored virtually the entire waveform for post-acquisition analysis. Since the integrity of the waveform was maintained, signal processing such as deconvolution and Fourier transformation were possible. The method was used for critical evaluation of a few signals from each test recorded at regular intervals during the solidification process. Analysis in the frequency domain proved very helpful in understanding the complexity of waveform changes that occur as a result of the components in the measurement system.

Analysis in the time domain provided valuable information on wave speeds and the effects of boundaries.

An objective of the experimental protocol was to maintain virtually constant test conditions while changing one variable at a time. Changes in acoustic emission behavior could then be attributed to that particular variable. The variables were chosen because of their effect on solidification mechanisms. For example, the addition of copper to the aluminum would result in two phases forming as the liquid solidified. Therefore, the acoustic emission changes that might occur could be correlated with the change in solidification mechanism.

The objective of changing one variable at a time was achieved with varying degrees of success. More than ninety experiments were performed on the three materials described in Section 3.1, Materials. Many of the initial tests simply constituted a learning curve. This led to a thorough understanding of how subtle variations in the measurement system can lead to dramatic changes in acoustic emission data. Each change in the system caused some change in the acoustic emission signal. This will be discussed in detail.

Another variation, in addition to the three materials, included the furnace atmosphere which was inert in some cases and contained hydrogen in others. Effects of metal mass, number of grains, transducer response, and specimen geometry were also investigated. A portable single channel AE detection system was built for low noise measurements. It was attached to a hot stage microscope for preliminary experiments which directly observed the solidifying surface of aluminum (Section VIII Suggestions for Future Work).

Discussion Section V concludes by considering how microstructures from the experimental specimens provide a metallurgical comparison to the acoustic emission data and justify the proposed models of AE sources.

5.2 Solidification Kinetics

Before an analysis of acoustic emission signals generated during solidification is presented, a more complete description of solidification kinetics and mechanisms will be given. A complete model would include a macromodel describing heat transfer from the melt to the mold wall as well as a micromodel of solidification kinetics and fluid flow in the mushy zone. However, because of the small scale of the castings and the high thermal conductivities of the metals, the macromodel will not be considered. The emphasis will be on morphological changes in the casting and their time-dependency.

The transformation of a liquid to a fully solid phase is a nucleation and growth process that occurs over a period of time. There are currently at least two approaches to the first process: continuous and instantaneous nucleation. Investigators even differ on the definition of continuous. Oldfield [78] suggests a parabolic dependence of the number of nuclei on undercooling and predicts nucleation until the onset of recalescence. Thevos [79] assumes continuous nucleation between the equilibrium temperature, T_E, and the maximum undercooling temperature. Nucleation, as proposed by Stephanescu et al [80], predicts the instantaneous formation of solid nuclei at a specific undercooling temperature, T_N.

For the practical purposes of the present study it is sufficient to know that nucleation begins at the moment the cooling rate deviates from its equilibrium conditions (Figure 5.1). Dendritic growth then follows until grains form. The solidification process is complete when equilibrium cooling resumes.

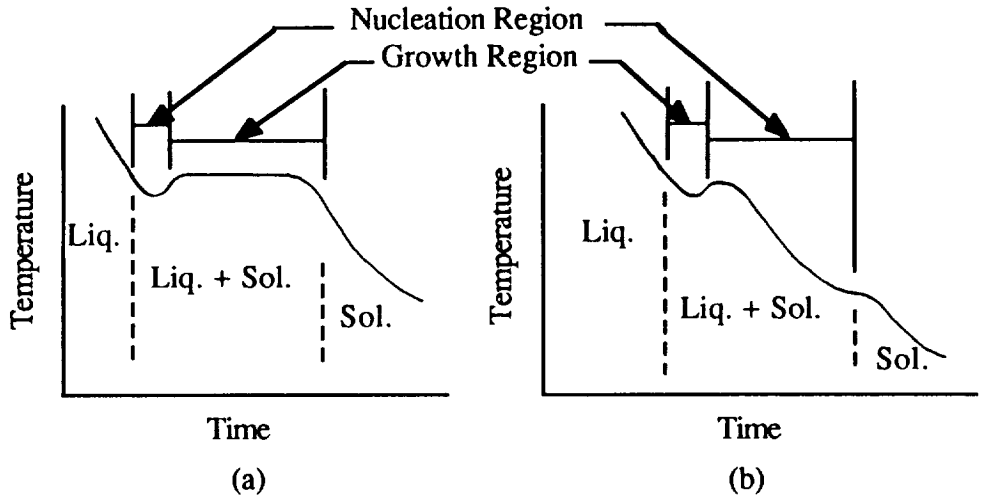

Figure 5.1 Nucleation and growth plots of solidification in (a) ultra-pure aluminum and (b) an Al-Li alloy.

Figure 5.2 illustrates that AE waves can only be detected if the velocity of a specific size source is above a threshold of detectability. If similar threshold values are used for the present solidification study as were used in the fracture studies [81], then, by knowing or approximating the source size and velocity, the detectability of the source may be determined. The method used to estimate the source velocity in the present study is computer-aided differential thermal analysis (CA-DTA) [82]. The first step in this method was to determine the fraction of solid, f_s, as a function of time which was derived from the thermal history or cooling curves.

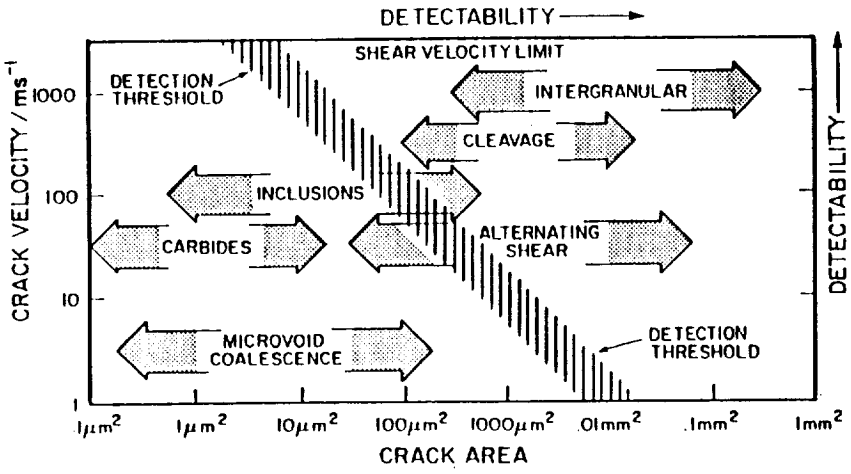

Figure 5.2 Detectability of acoustic emission signals by considering source velocity as a function of source area [81].

The latent heat of solidification,L', at a specific time, t, was calculated by using the following difference equation with the upper limit of integration being that time, t.

$$L' = C_p \text{ [area under } (dT/dt)_{cc} \text{ - area under } (dT/dt)_{zc}] \qquad \text{(Equation 8)}$$

where: C_p - specific heat

cc - cooling curve in the temperature region where solidification occurs.

zc - zero curve, based on cooling curve in temperature region after solidification has occurred.

Once the latent heat is known at a sufficient number of times during solidification, the fraction of solid as a function of time is given as

$$f_s = L' / L_{TOTAL} \qquad \text{(Equation 9)}$$

Using the cooling curves of Figure 5.1, the fraction of solid was plotted for castings of ultra-high purity (UHP) aluminum and an aluminum-lithium alloy (Figure 5.3). Both curves are slightly parabolic and clearly show the time dependency of solidification. Within the first minute, approximately 20 % of each specimen has solidified. One minute before the end of the transformation, less than 10 % of the liquid remains. Complete solidification of the UHP aluminum casting requires over six and a half minutes, whereas, the Al-Li alloy casting takes a minute less. Cooling curves for the aluminum-copper alloy used throughout this study provide similar results.

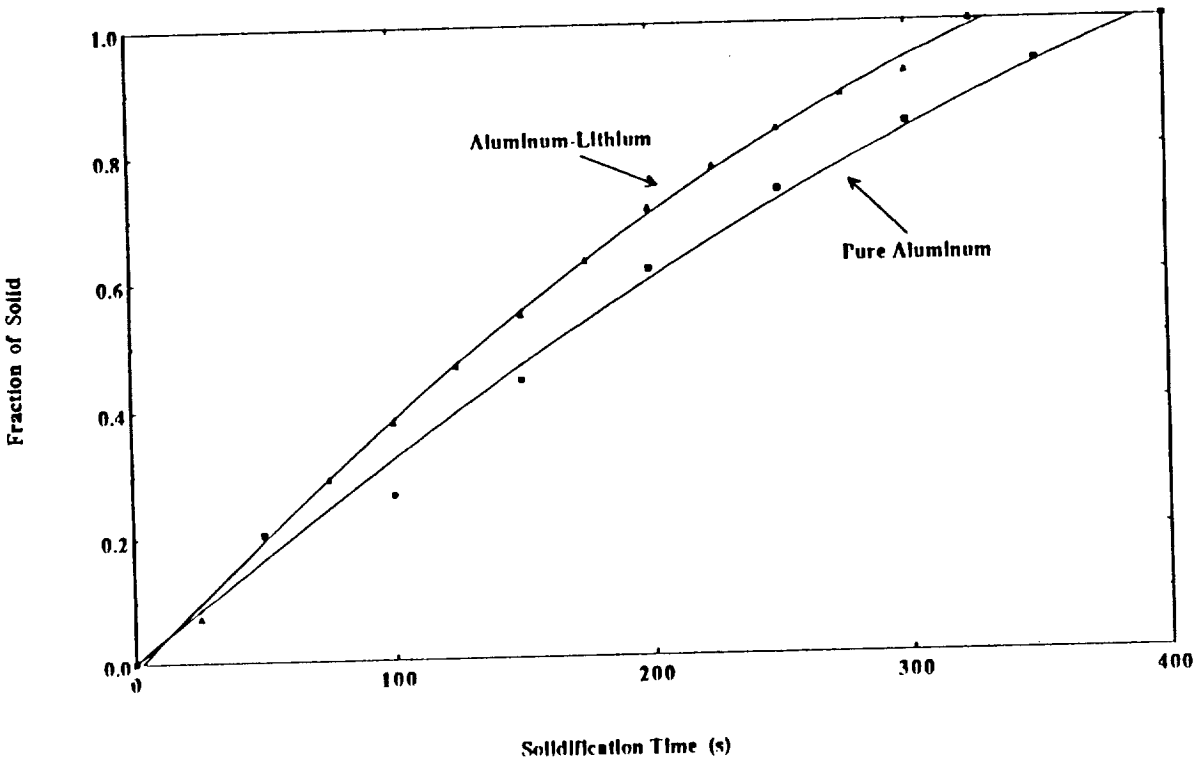

Figure 5.3 Fraction of solid as a function of solidification time for (a) a 2.7 g UHP aluminum and (b) a 2.7 g AA2090 Al-Li alloy specimen cooled at the same rate.

To put the solidification rate in perspective, the average grain size of a small aluminum-lithium casting was determined to be 0.3 mm. Assuming the nucleus forms in the center of the grain, the grain radius of 0.15 mm may then be considered to be the total growth distance during solidification. The estimated growth rate, therefore, is 0.15mm/400 s or approximately 4×10^{-7} m/s. Even considering that the secondary dendrite arm growth velocity may be several orders of magnitude greater than the

primary, it is still very slow and does not compare with the 100 m/s velocity of inclusion cracking which does release detectable acoustic emission. It is concluded that growth and impact of dendrites during the formation of grain boundaries is not a viable source of acoustic emission.

At the onset of the experiments, nucleation was considered as a possible AE source as proposed by Xiufang [17]. If the instantaneous nucleation model of Stephanescu [80] is considered then it is conceivable that the expansion rate of a developing nucleus would be fast enough to generate a detectable stress wave within the remaining liquid. The key to verifying this would be detection of AE signals during the narrow nucleation temperature range. This was a critical part of the present experiments and will be discussed in the same sections listed in the previous paragraph.

Likewise, porosity, which develops as hydrogen evolves from the solidifying casting, has also been proposed by others [14] as an AE source. If the rapidly expanding pores generate acoustic stress waves, then the measurable percent of porosity would be proportional to the cumulative number of acoustic emission hits. This was also investigated, as described in III. Experimental Procedures, by varying the percent of hydrogen in the furnace atmosphere. Other acoustic emission sources that were considered include: dislocation motion and micro-cracking from residual stresses during solidification, dendrite fracture, liquation cracking, and oxide cracking.

5.3 Acoustic Emission from Pure Aluminum Castings

5.3.1 Conventional Analysis

Over thirty tests were performed on 2.7 gram specimens of ultra-high purity aluminum. They were conducted in an inert argon atmosphere using an integral BN crucible and waveguide. Initial trials collected few acoustic emission hits. The reason was poor coupling of the specimen with the crucible bottom and, therefore, with the transducer. Even in an ultra-high purity (UHP) argon atmosphere the polished specimen developed a thin oxide coating which acted as its own crucible. The oxide coating prevented the specimen from assuming the shape of the crucible, and good transmission of the AE signals was impaired. When additional weight was placed on top of the melt, the liquid metal was able to break through cracks which formed in the oxide filling the bottom of the crucible. As a result, acoustic emission signals were detected when the weight was added.

Insertion of the thermocouple into the melt also caused poor AE detection. As the specimen cooled and bonded to the rigid T.C. wires, it was pulled away from the crucible bottom. The problem was solved by redesigning the weight to hold the T.C. in the melt as well as force the casting to remain in contact with the crucible bottom. Details are given in the Experimental Procedures Section 3.3.1.

Although the cumulative number of hits in subsequent tests ranged from 200 to over 1,000, a common pattern was seen in every experiment. The system was quiet during the first few minutes of the test. A one to two minute period of high acoustic emission activity followed, then a quiet period returned as the specimen cooled. Figure 5.4 shows the results of two such tests. Although the number of hits varied, the rate of hits and the

period of high activity coincide. The next step was to determine the temperature range in which this activity occured. The purpose was to correlate it with the solidification mechanisms.

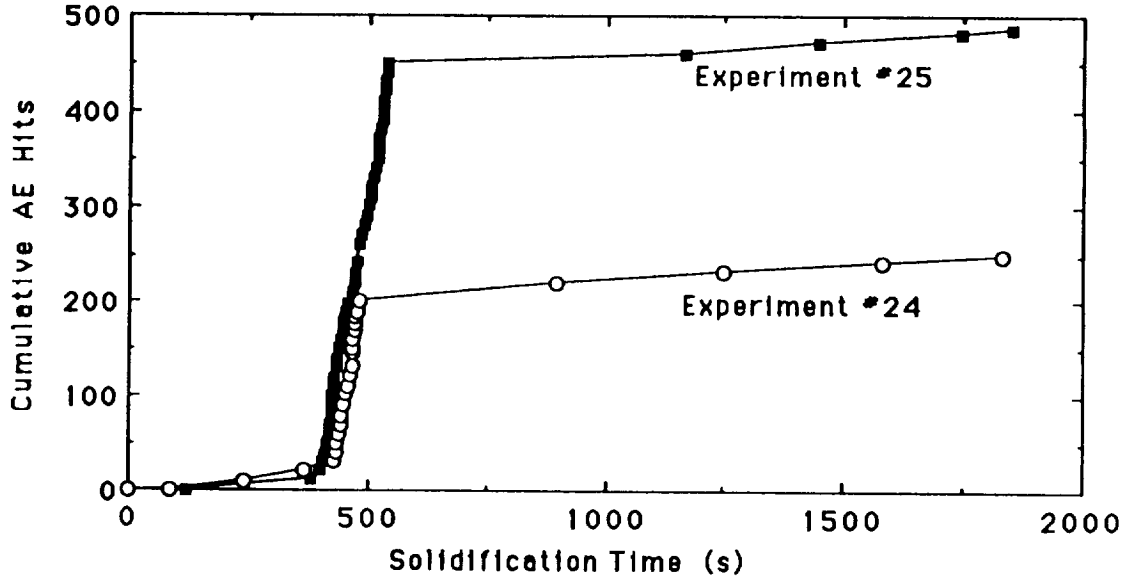

Figure 5.4 Plots of cumulative acoustic emission hits v. time during the solidification of UHP aluminum from two experiments with similar volume specimens.

The cooling curve of Figure 5.5 illustrates the temperature range of high acoustic emission activity. It can be seen that it coincides with the last minute of solidification. Referring to the fraction of solid plot in Figure 5.3, it can be concluded that virtually no AE hits are detected until less than 10% of the liquid remains. Also, the high activity ceases immediately when the specimen is 100% solid with only scattered hits thereafter.

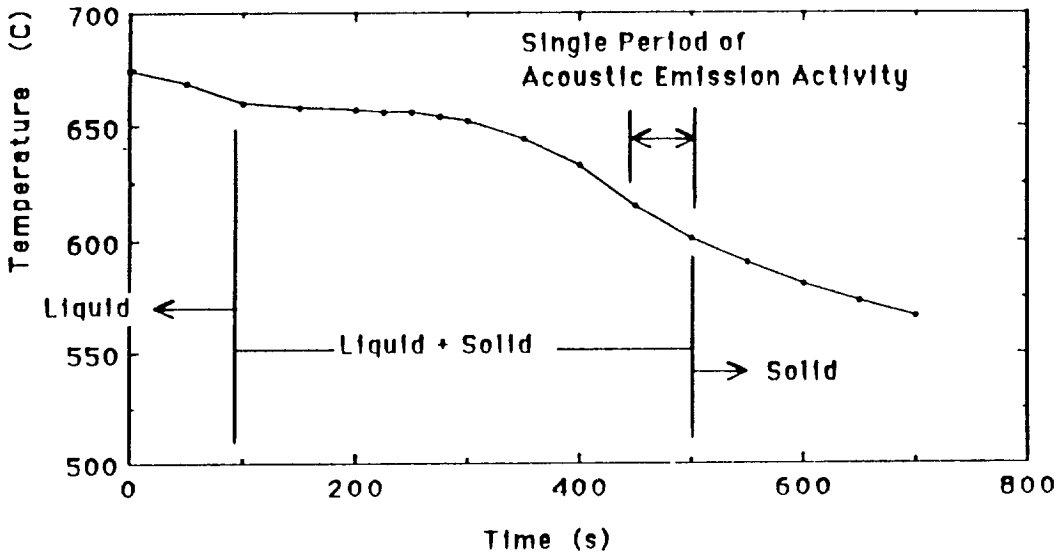

Figure 5.5 Cooling curve of 2.7 g ultrapure aluminum casting indicating temperature range that corresponds to high acoustic emission activity.

As discussed in Section 5.2, Solidification Kinetics, nucleation occurs during recalescence as the latent heat is evolved and dendritic growth follows. No acoustic emission was detected during nucleation or the early stages of dendritic growth. The hits are generated during the time period when dendrites impinge on each other, forming grains, i.e., as the last fraction of solid forms. The observation that the activity begins during a thermal arrest leads to the assumption that volumetric shrinkage was not an AE source. This logic implies that the melt has not pulled away from the mold wall. The reason is that thermodynamic principles conclude: if the presure and temperature remain

constant, the volume will not change. If an oxide coating had been responsible for the AE hits, continuous activity would have been expected during cooling from the superheat temperature of 700°C to the transformation temperature of 660°C or during massive shrinkage below this temperature.

Metallographic analysis (Section VI) revealed equiaxed grains which was expected since the temperature readings showed virtually no change from the center of the casting to any side. No microporosity was present which was also expected since it has been shown [83] that excess molecular hydrogen remains in solution as high purity aluminum solidifies without forming pores.

The mass of the specimen was doubled for a series of tests in an alumina crucible that was cemented to a boron nitride waveguide. Dimensions of this waveguide were similar to the BN rod. The purpose was to observe the effect of increased solidified mass and to be sure that the results are a function of the casting material and not the measurement system. It should be noted that, whenever a new setup was used, acoustic emission was monitored without a specimen to verify that heating and cooling the system would not contribute to the number of signals. In all cases, with argon gas and compressed air flowing, there was no acoustic emission generated with an empty crucible during a simulated melting and solidifying cycle.

Figure 5.6 illustrates four conventional AE parameters plotted as a function of time. At the end of solidification, approximately 800 seconds, a trend is observed. The amplitudes of some signals increase to a maximum of 80 dB from a level below 50 dB. The rise times increase to a maximum of 180 μs from a 40 μs maximum before the period

of high activity. The durations also increase from less than 200 μs to a peak of 1,600 μs. Finally, the energy reaches a maximum for some signals of 180 V-s. Therefore, it may be concluded that the overall intensity of AE signals increases significantly as the last fraction of solid forms, i.e., the grains form in the metal. Figure 5.7 contains two amplitude distribution plots with the dependent variables being hits and duration. From this amplitude distribution data, no characteristic amplitude or duration may be determined for signals generated during solidification of UHP aluminum.

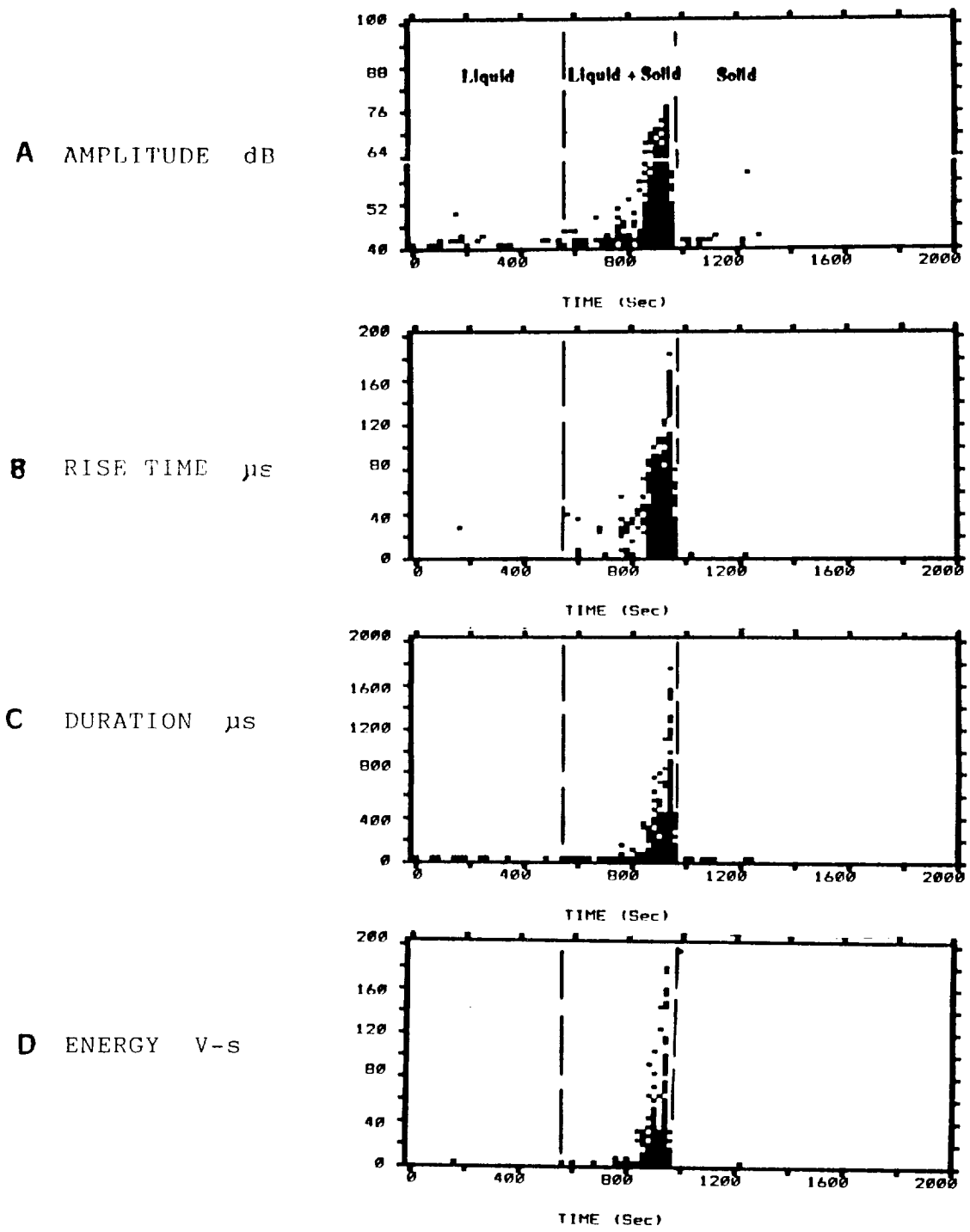

Figure 5.6 Acoustic emission (a) amplitude, (b) rise time, (c) duration, and (d) energy as a function of time during solidification of an UHP aluminum.

a HITS #

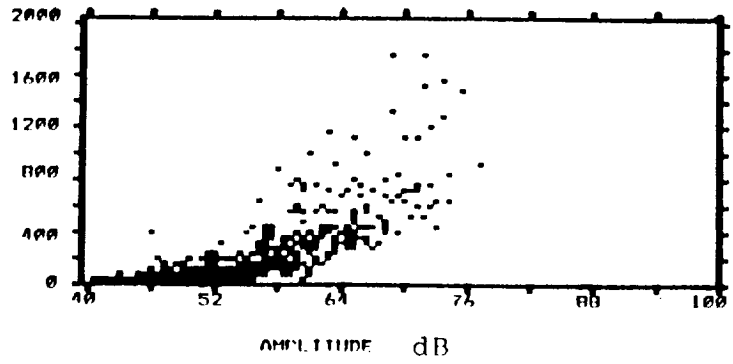

b DURATION μs

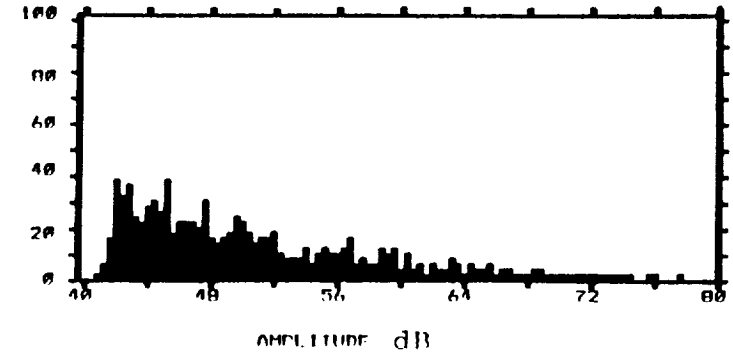

Figure 5.7 Acoustic emission (a) hits and (b) duration as a function of amplitude during solidification of an UHP aluminum.

Figure 5.8 displays the cumulative AE hits for the 5.2 g aluminum specimen cast in an alumina crucible. The upper figure (a) is a time expansion of the initial part of the test. As with the smaller casting (Figure 5.4), there is a rapid increase in AE hit rate which decreases abruptly afterwards. The total number of hits reached 1,100 during this period. The test was repeated on the same specimen twice with hits totalling 1,000 and 1,600. The interesting variation between this series and the 2.7 g tests is the second period of AE activity which begins three and a half minutes after the first period.

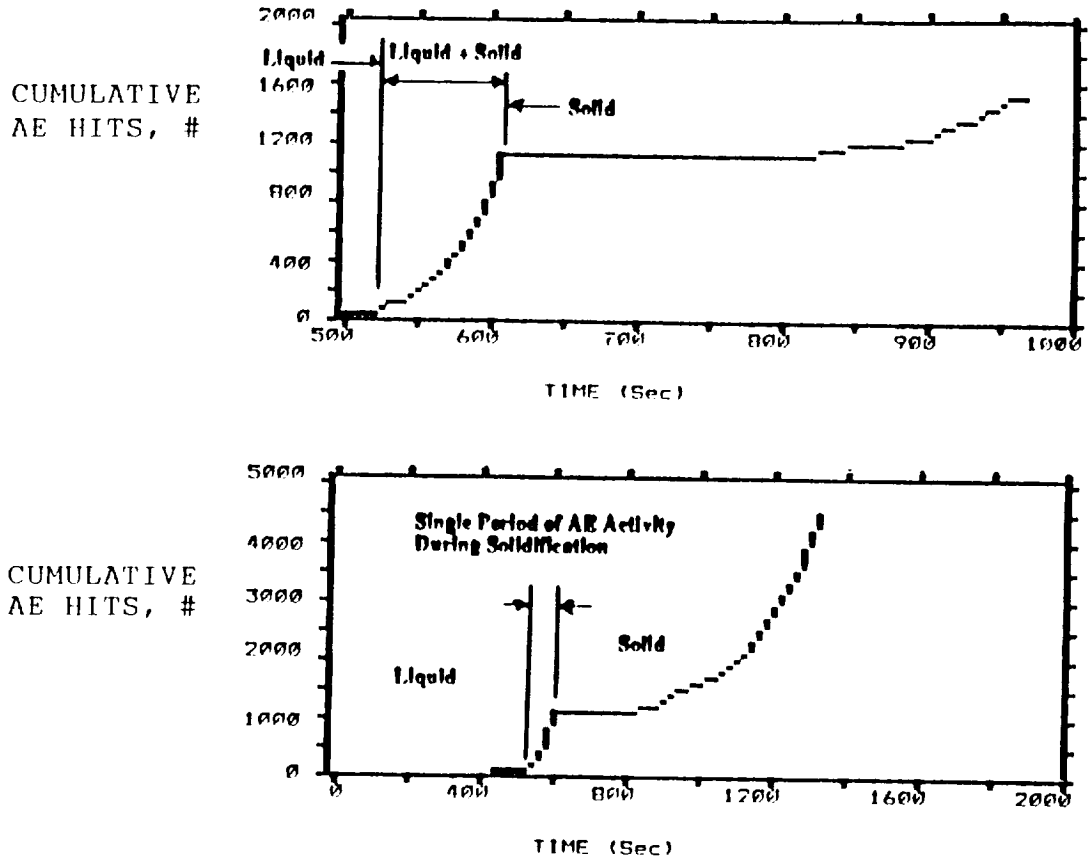

Figure 5.8 Plots of cumulative acoustic emission hits v. time during the solidification of a 5.2 g ultra-pure aluminum casting. (a) The upper plot is a time expansion of the first 1,000 seconds of (b) the lower plot.

The recording instrument was turned off at 4,516 hits but the activity continued for at least another 20,000 hits. The start of the second period corresponds to a temperature where the material is completely solid and has cooled more than a hundred degrees Celsius below its solidification temperature (Figure 5.9). This type of behavior was not observed in the boron nitride crucible, which does not adhere to aluminum, but is evident with an alumina crucible which does restrain the shrinking casting.

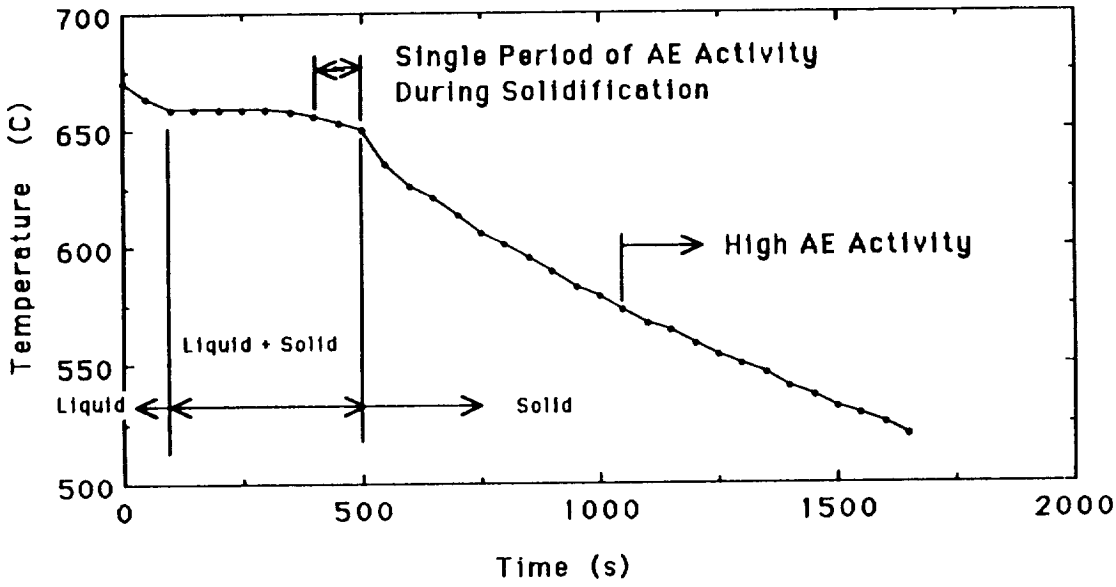

Figure 5.9 Cooling curve of 5.2 g ultrapure aluminum casting indicating temperature ranges that correspond to periods of high acoustic emission activity.

The results of the ultrapure aluminum experiments lead to several conclusions. Acoustic emission is generated by inherent solidification mechanisms that occur as the last fraction of solid forms. Nucleation is not a source of AE in pure solidifying aluminum. Likewise, porosity was not responsible for the AE signals since no porosity was present. Dendritic impact may be discounted in the present experiments as an AE source since the growth rates have been shown to be too slow to produce detectable stress waves. Oxide cracking and volumetric shrinkage are not reasonable AE sources since the activity at the end of solidification lies within a discrete time period at constant temperature. Both mechanisms would display high AE activity during periods of temperature change and this activity was not observed. Mold wall friction would have caused the continuous form of acoustic emission. Only burst signals were recorded, with no continuous emission; therefore, friction between the mold wall and the specimen was discounted as an AE source in the present experiments.

Many possible sources of AE have been eliminated as a result of solidification of ultra-pure aluminum. Additionally, microstructural analysis, described in Section 6.1, revealed no significant inclusion content which may have been a source of cracking and, therefore, acoustic emission. Only a single phase matrix was present which formed equiaxed grains during the liquid-to-solid transformation.

The model that is proposed for the first period of AE activity involves the tips of adjacent dendrites meeting in opposing growth directions while surrounded by the remaining liquid. The tips do not instantaneously cease growing but rather exert mutual opposing forces until the process is brought to an end. These stresses provide a driving

force for diffusion-controlled dislocation motion within the dendrite arms. As grains form, their boundaries introduce low energy sites for the release of strain energy from dislocation pile-ups. No energy dissipation in the form of heat evolution was measured during this first period of AE activity. Therefore, it is suggested that the primary form of this energy release is acoustic waves.

Another possible source is crystallographic realignment to accommodate grain formation. This would introduce grain boundary sliding and also cause fused dendrite tips to fracture, thereby releasing bursts of strain energy until solidification is complete. While no evidence of grain boundary sliding was derived, metallographic analysis did reveal dendritic tip fracture in the Al-Li alloy as discussed in Section VI.

The AE activity after solidification appears to be a function of specimen restraint by mold wall adhesion. As the casting cools and shrinks, an avalanche of dislocation sources are created as newly formed grains are internally stressed. This activity is outside the realm of a solidification study since it occurs substantially below the solidification temperature. For a more quantitative description of the relationship between specimen restraint and acoustic emission, the reader is referred to a paper by Sharma, et al [16]. They conclude that the AE energy increases by a factor of four as the solidification condition changes from free contraction to high restraint (0 to 37.6 kg/mm restraining spring stiffness). They proposed hot tearing and pore formation as the AE source mechanisms.

5.3.2 Waveform Analysis

Individual signals were recorded during the solidification of the ultra-pure aluminum castings. The method, described in Section 3.3.2, permits both time and frequency domain representation of the signals. The intent was to identify any waveform characteristics that might change during cooling and correlate them with defect mechanisms such as solidification cracking.

Figure 5.10 (a-d) illustrates four signals from a solidification experiment recorded at equal time intervals, from the beginning to the end of the solidification period. The signals were recorded periodically and, at first, the time domain waveforms appear to decrease in duration as the solidification takes place. Referring back to Figure 5.6(c), it can be seen that the trend for most signals is the opposite. This illustrates that careful interpretation of the individual waveforms is required since random selection of a few signals can lead to false conclusions of the total AE signal trend.

Analysis of the power spectra for the four signals reveals a strong resonant peak at approximately 11,000 Hz with harmonics at 22,000 and 33,000 Hz. As discussed in Section 4.3, Waveguide Response, when the signal is not frequency filtered, the dominant spectral component is the fundamental resonant frequency of the waveguide. This is what occurred in the experiment of Figure 5.10. The acoustic signals were not passed through the 100-H filter after being transmitted through a BN rod and broadband S9208 transducer. Therefore, the response of the waveguide overpowers that of the transducer response and acoustic emission signals. The spectra will be virtually the same

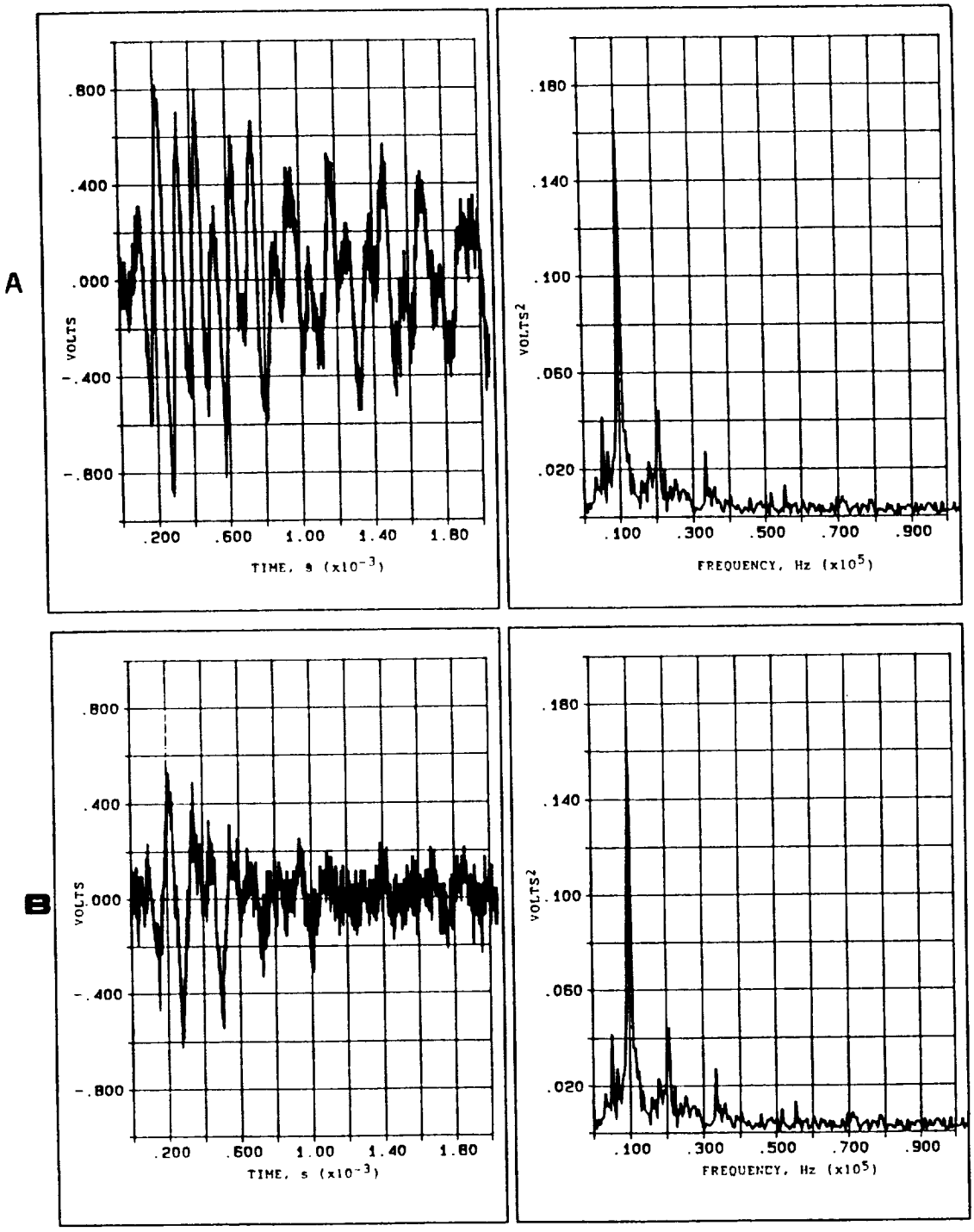

Figure 5.10 Acoustic emission signals recorded from (a) beginning to (d) end of the solidification of an ultra-pure aluminum casting and displayed in the time and frequency domains .

C

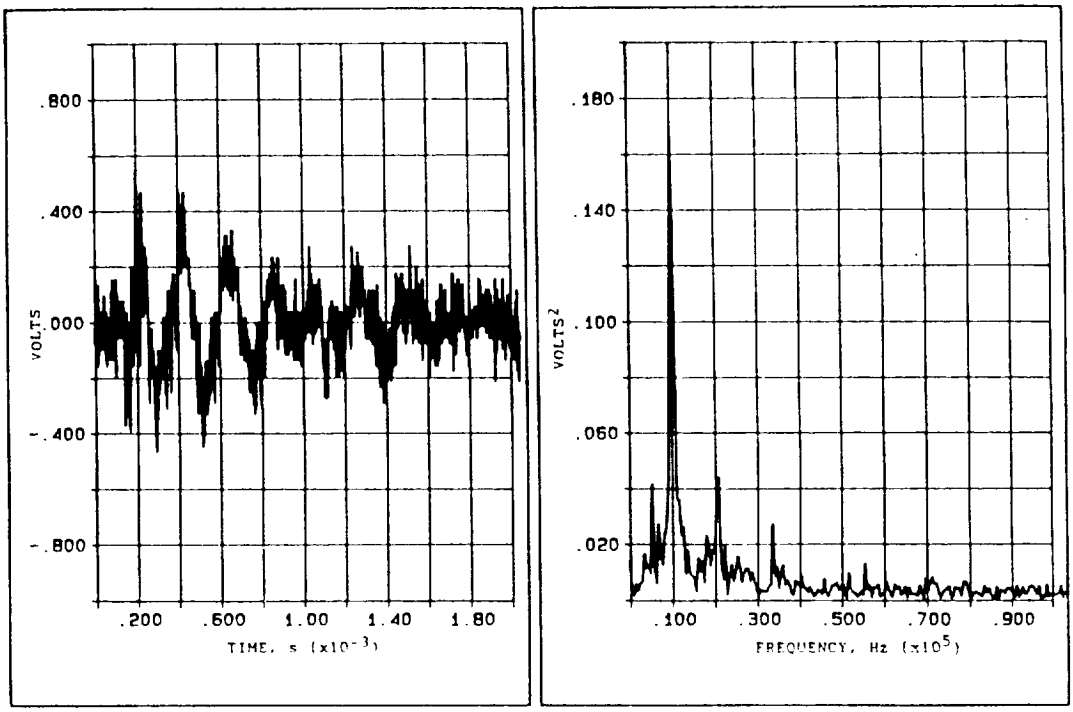

D

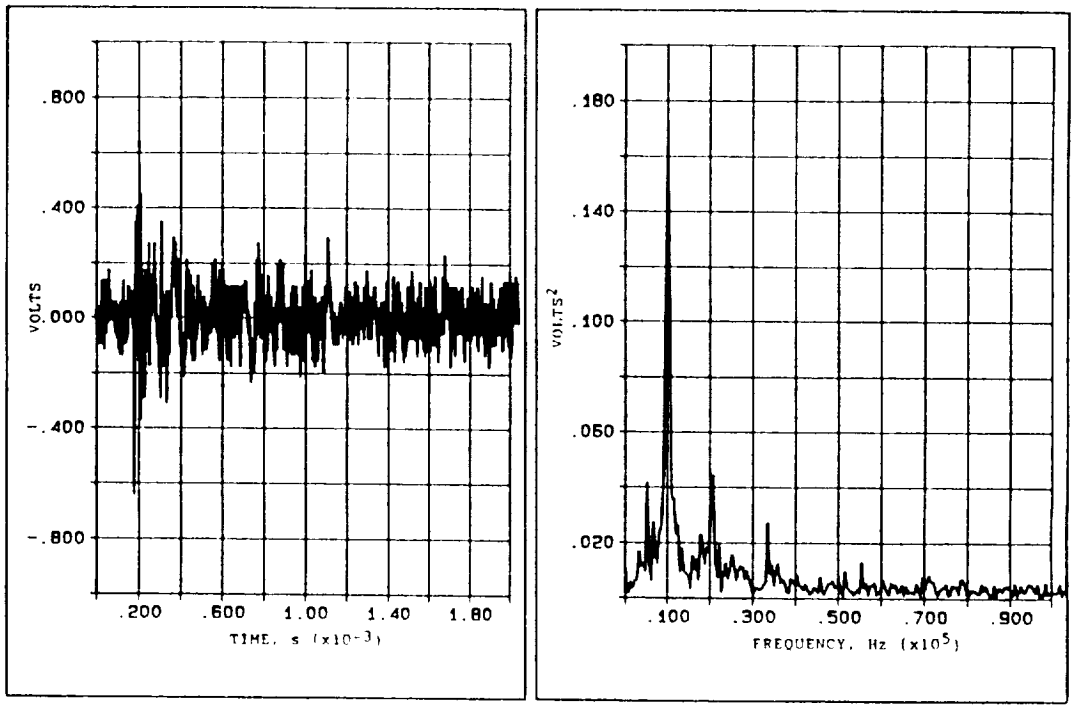

Figure 5.10 Continued.

regardless of the type of source mechanism and, therefore, a characteristic spectrum cannot be attributed to a specific acoustic emission source. The result is that little information is obtained from the spectra on AE characteristics.

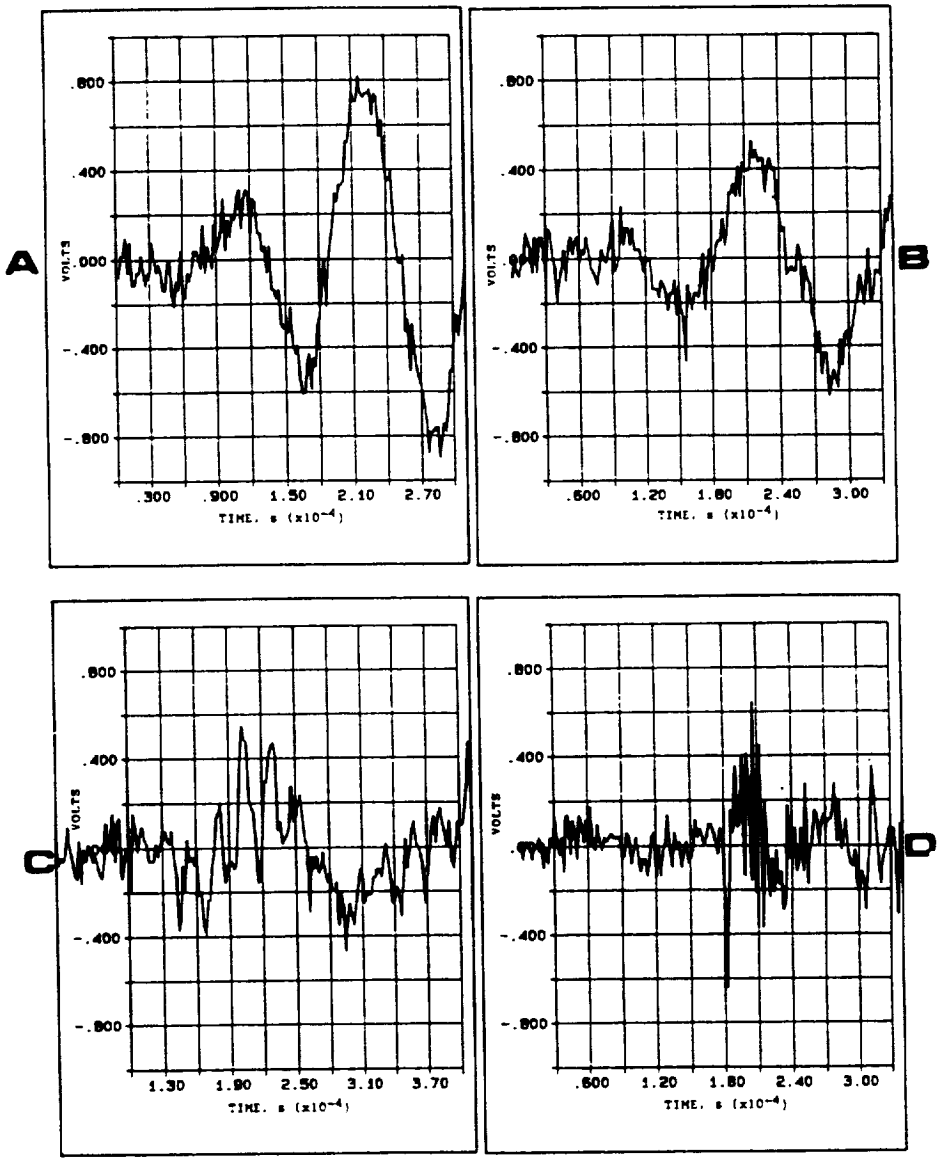

Figure 5.11 Expansion of first wave arrivals in signals shown in Figure 5.10.

The initial wave arrivals of Figure 5.10 are assumed to be the first longitudinal wave arrivals or p-waves. They were expanded from Figure 5.10 and are shown in Figure 5.11. No consistent information on signal characteristics such as rise time or duration could be determined from these signals or from additional p-wave analysis. Therefore, this type of analysis was not pursued in the present study.

For comparison, four signals from a second solidification experiment are shown in Figure 5.12. It can be seen that a resonant frequency of 8,200 Hz dominates the spectra. A broadband transducer was used along with a 28 cm BN rod (7 mm longer than the first experiment. No frequency filtering was done. By applying Equation 7, the resonant frequency of the rod was calculated to be 8,200 Hz (2,800 Hz lower than in the first experiment). Therefore, it is again concluded that the spectra reflect primarily the waveguide response.

Although these eight waveforms are simply examples from two experiments, analysis of hundreds of other waveforms from other tests led to the same conclusion. Neither individual waveform nor frequency spectrum analysis of acoustic emission from solidifying pure aluminum were able to identify signal characteristics that could be correlated to a source mechanism.

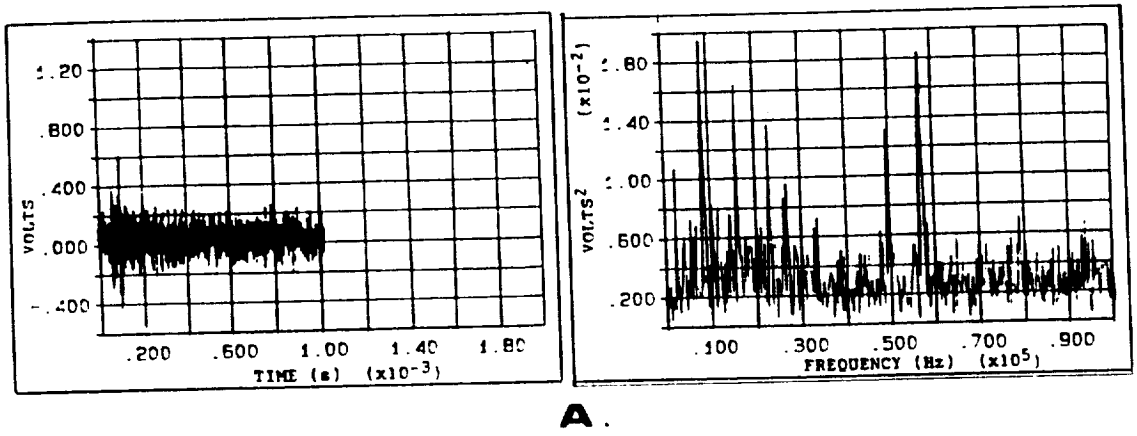

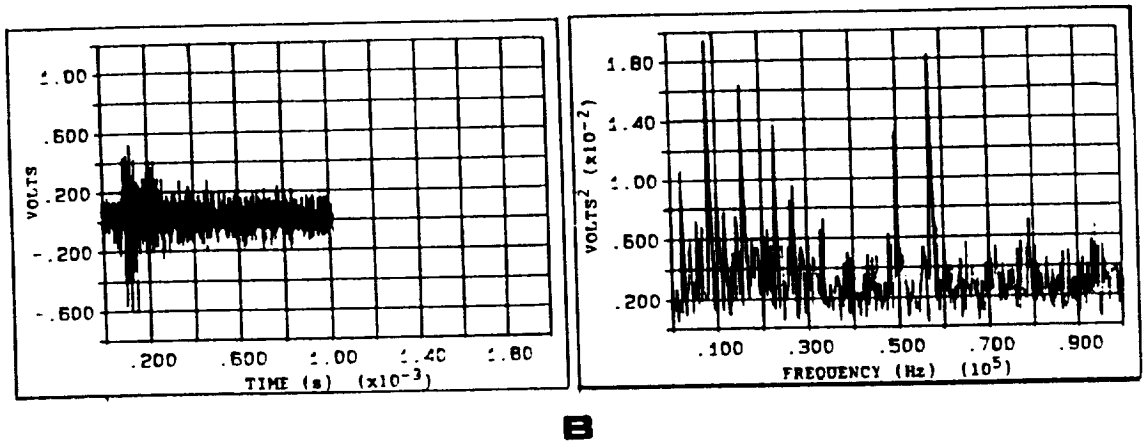

Figure 5.12 Acoustic emission signals recorded from (a) beginning to (d) end of a second solidification experiment using UHP aluminum.

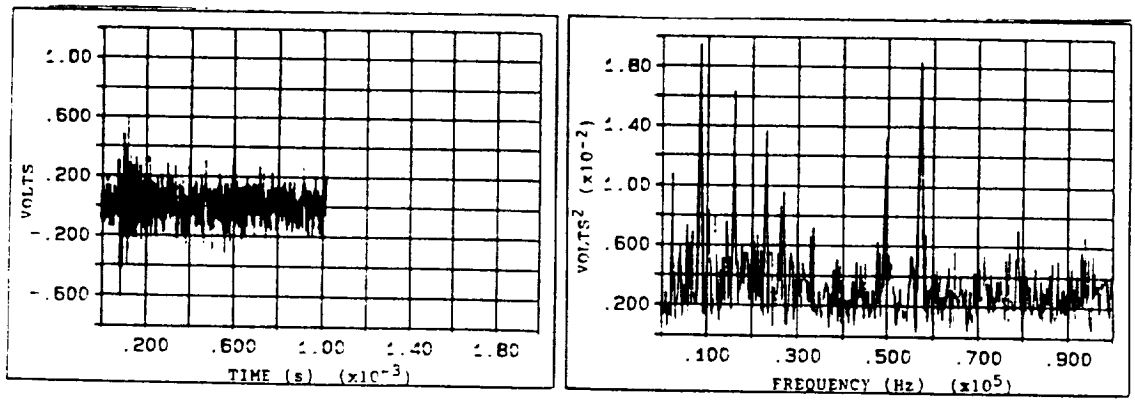

C

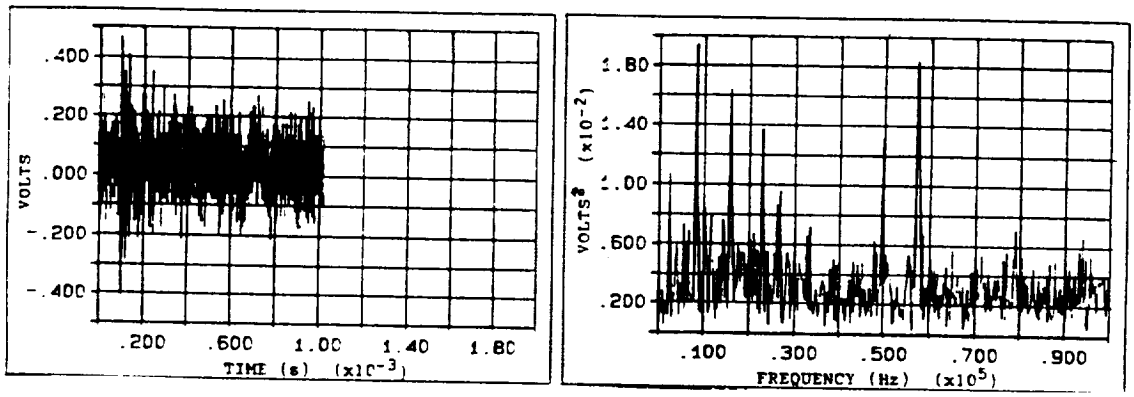

D

Figure 5.12 Continued.

5.4 Acoustic Emission from Aluminum-Lithium Alloy Castings

5.4.1 Conventional Analysis

Ultra-pure aluminum has been shown to generate a single period of acoustic emission during solidification. In contrast, aluminum-lithium alloys have two discrete periods of AE activity which may be correlated with two solidification mechanisms. The second period will be discussed first. As with the pure aluminum, it occurs at the end of solidification.

The second period of acoustic emission occurs during the last minute of solidification which corresponds with approximately the last ten percent of liquid. At this time, the dendrite tips are impinging on each other and grain boundaries are being developed. As discussed in Section 5.3.1, the grain boundary formation provides low energy sites as destinations for dislocations contained within the solid. The high temperature, well above 0.5 T_M, and the moderate to high residual stresses are conditions required for diffusion-controlled dislocation creep [83]. This movement of dislocations from the matrix to the grain boundary results in a release of strain energy which is considered a primary source of acoustic emission. Another source which may contribute to the total cumulative AE events is solidification cracking. As shown in Section VI, Metallographic Analysis, solute segregation and secondary phase formation combine to form brittle regions within the alloy which result in microcracking of the porous material as it cools. This event releases strain energy which is transmitted as acoustic emission.

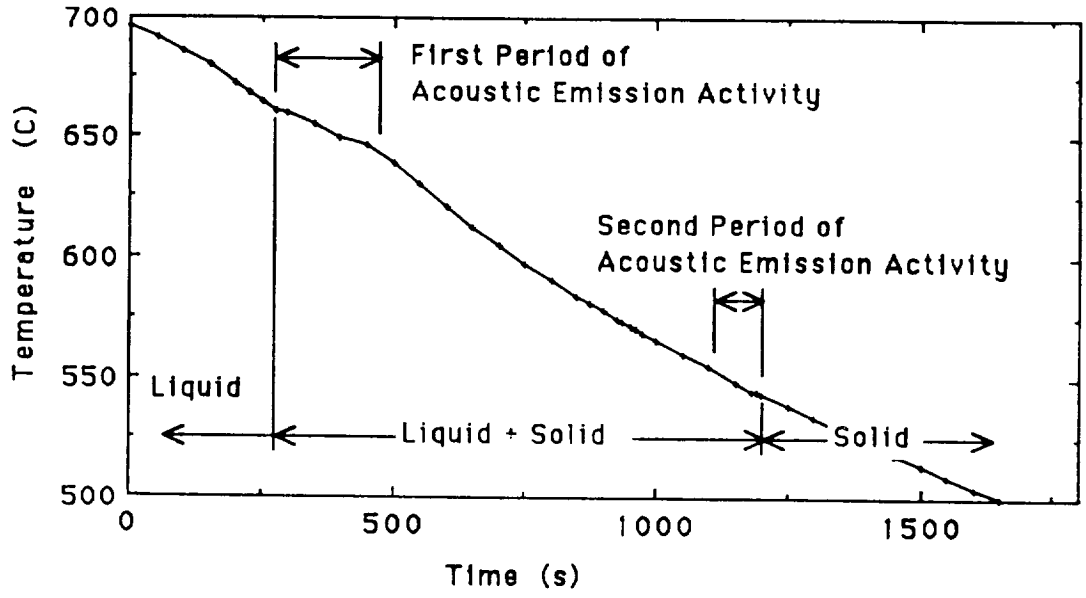

Figure 5.13 Typical cooling curve of 2.7 g aluminum-lithium alloy casting indicating temperature ranges that corresponds to high acoustic emission activity.

The release of strain energy during grain boundary formation was a source mechanism proposed for the single AE period of pure aluminum. Imposed stresses at high temperature that cause fracturing of fused dendrite tips, diffusion-controlled dislocation motion (dislocation creep), and grain boundary sliding are present in alloys as well. If the dendrites are aligned with each other (columnar) as they grow, rather than at opposing angles (equiaxed), then it would be expected that less compressive stress between grains would be present and less realignment would occur.

The same acoustic emission source mechanism that was proposed for UHP aluminum, grain boundary formation, is also proposed for the second period of AE activity during solidification of an aluminum-lithium alloys. As with the pure metal, this

regime corresponds with the formation of a single phase. The solidification rate of the Al-Li alloy can be seen in Figure 5.3 to be greater than the pure aluminum but the dendritic growth rate is still to be considered too slow to generate detectable stress waves upon impact. The signals are burst-type, not continuous, and only occur within a specific temperature range. As the solvus is reached, the activity slows significantly. The low level of activity that is present is considered a result of continued grain boundary realignment and micro-cracking after solidification. Oxide or hydride cracking, mold wall friction, and volumetric shrinkage are again discounted since they would generate emissions throughout cooling rather in a discrete temperature interval.

A comparison of microstructural and acoustic emission data provide more evidence that the source of high AE activity is grain boundary formation. Table 5.1 lists the results of seven experiments performed on equivalent size specimens under similar initial conditions. Although the intent was to maintain a constant cooling rate for all tests, the small size of the castings and the furnace variables (particularly gas flow and heat extraction) made a constant rate difficult to achieve. As a result of cooling rate variances, the shape of the grains varied from equiaxed to columnar. Taking advantage of the microstructural differences, the grain shape was examined and compared to the AE data. It can be seen qualitatively in Table 5.1 that, as the microstructure changes from equiaxed to columnar, the percentage of total AE hits occuring in the second period decreases. This is in agreement with the concept that less dislocation creep and grain boundary sliding occurs in columnar grains and, therefore, less strain energy is released to generate acoustic emission hits.

Table 5.1 Relationship of microstructure and second period AE hits in an aluminum-lithium alloy.

Test	2nd Period Hits (%)	Type of Grain Structure
Li7	77	equiaxed
Li10	71	equiaxed
Li17	70	equiaxed/columnar
Li18	69	equiaxed/columnar
Li11	50	equiaxed/columnar
Li14	25	columnar
Li19	13	columnar

From over thirty tests, selections were made to illustrate common trends in AE activity. Figure 5.14 contains plots from four tests on 2.7 g specimens in the standard BN waveguide/crucible arrangement. The upper plot for each test is the cumulative AE hits v. time that has been previously used. The lower plots are derivatives of the cumulative curves. This method of data analysis displays hit rate and illustrates the length of time and acuity of the AE activity periods. When the rates are normalized and compared, the reproducability of the experiments can be observed (Figure 5.15).

Normalizing removes the effect of crucible-melt coupling by disregarding the total number of hits and designating the maximum rate as unity.

The cascade plot of Figure 5.16 is another method of presentation that shows the common occurence and duration of a first period of AE activity in five similar tests. Although a second period of AE activity occured in every Al-Li alloy experiment, the number of hits varied considerably. As was discussed at the beginning of this section, this may be attributed to the deformation mechanisms present. For example, less grain boundary sliding in the columnar grains produces less acoustic emission. Finally, Figures 5.17(a) and (b) plot acoustic emission parameters as functions of temperature. Figure 5.17(a) uses cumulative AE hits as the dependent variable, whereas, Figure 5.17(b) uses signal duration. The former shows that the AE begins at the liquidus with strong periods of activity at the beginning and end of solidification. The latter illustrates longer duration signals at the end of solidification. As will be discussed later with reference to Figure 5.20, the longer durations were concluded to be a function of source intensity rather than fraction of solid since the durations decreased again after the specimen was fully solid.

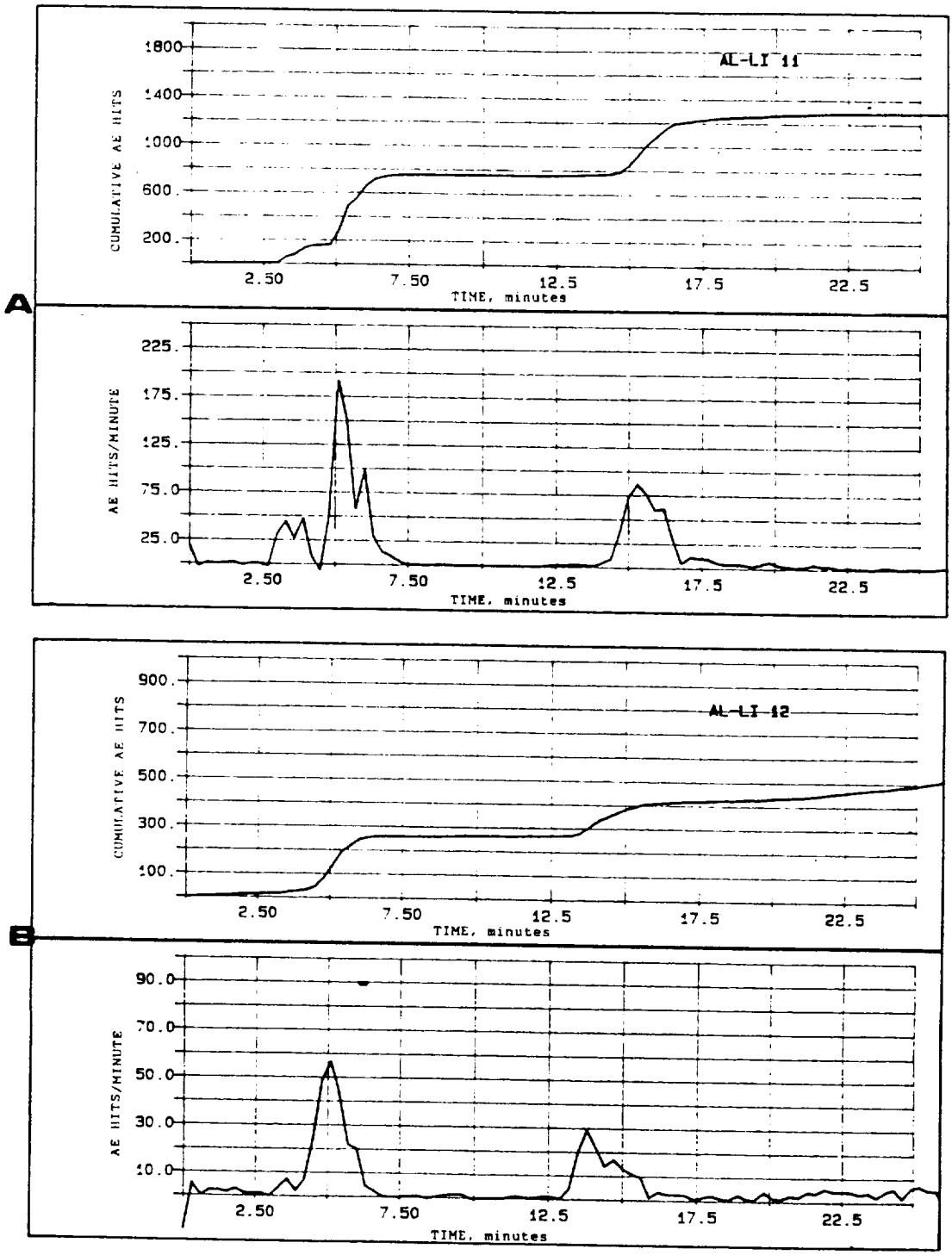

Figure 5.14 (a-d) Results of four experiments illustrating cumulative AE hits v. time (upper plots) and AE hit rate (lower plots) for 2.7 g Al-Li alloy castings.

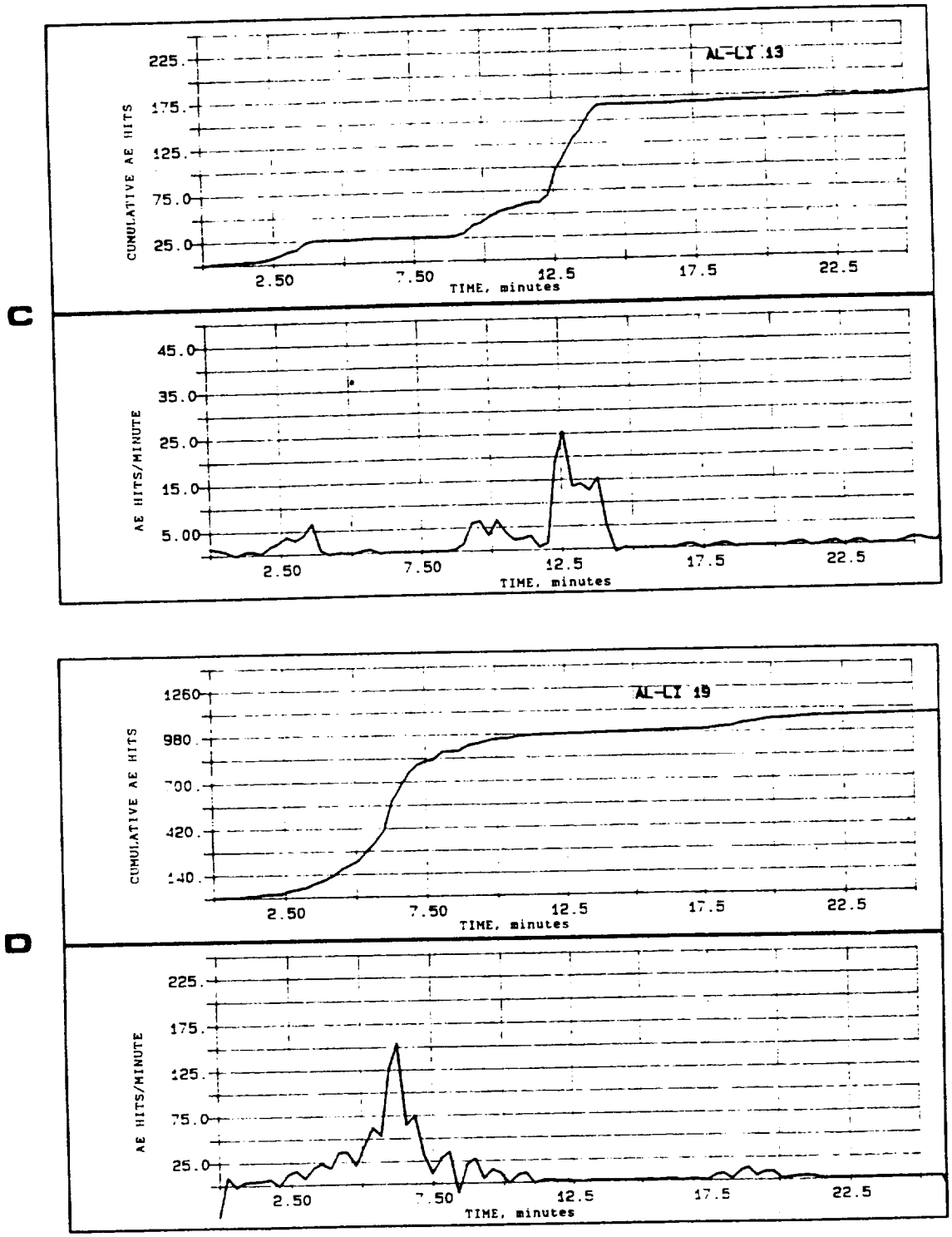

Figure 5.14 Continued.

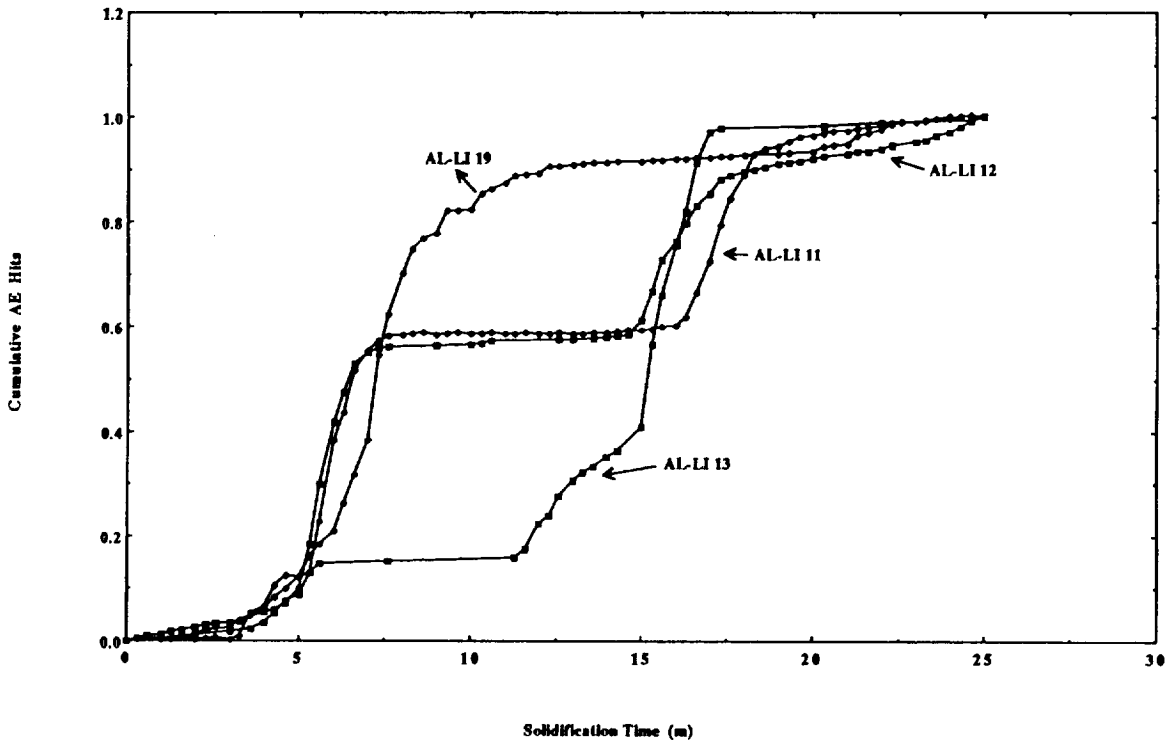

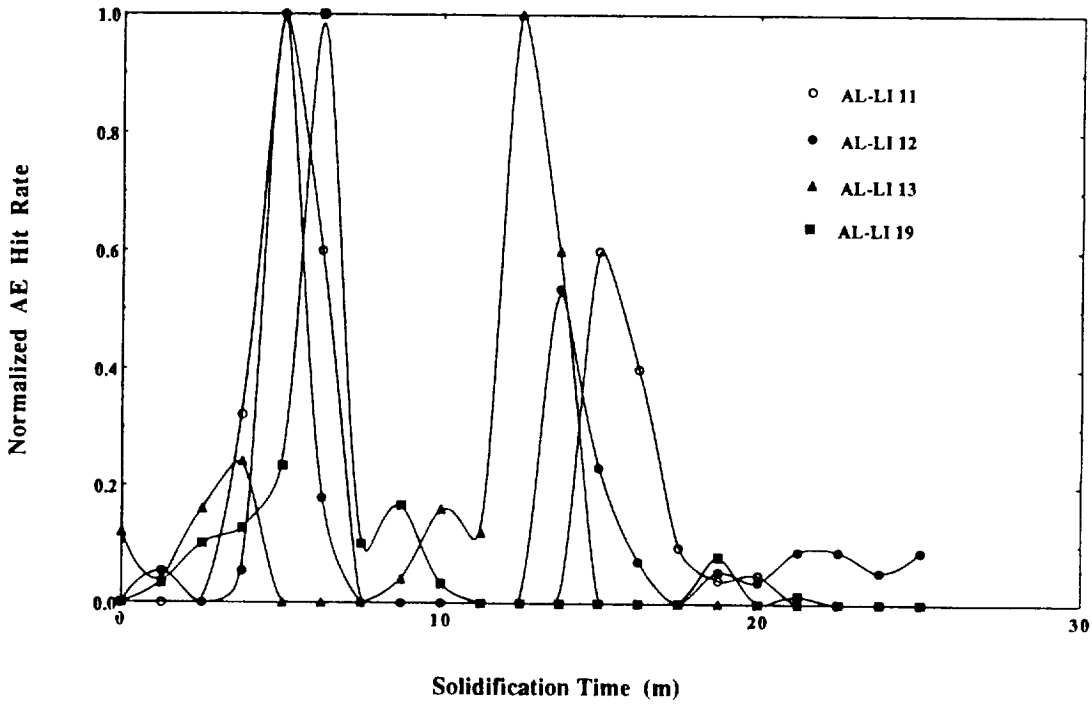

Figure 5.15 (a) Normalized cumulative AE hits v. time and (b) normalized AE hit rate for four Al-Li alloy solidificaton experiments.

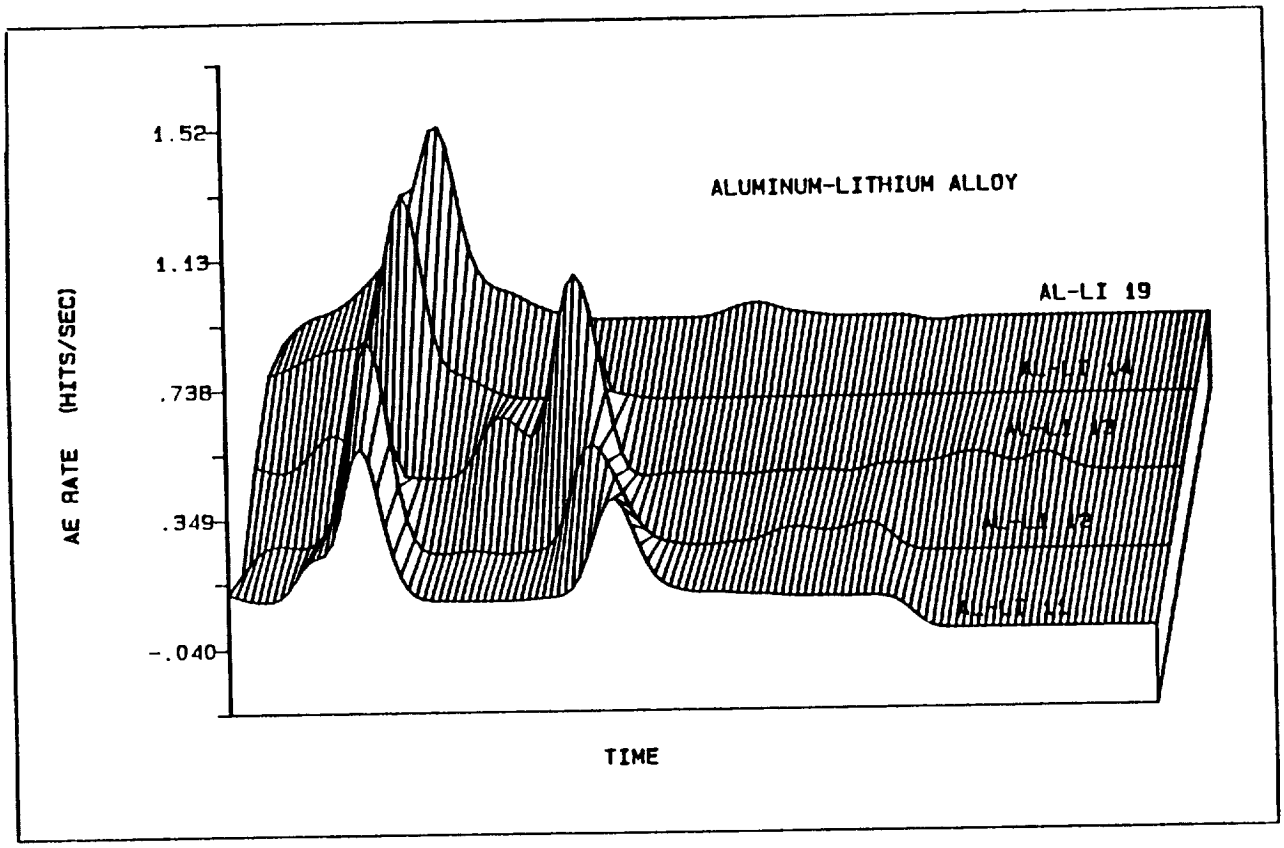

Figure 5.16 Cascade plot of AE hit rate v. time for five aluminum-lithium alloy specimens during solidification, cast under similar conditions.

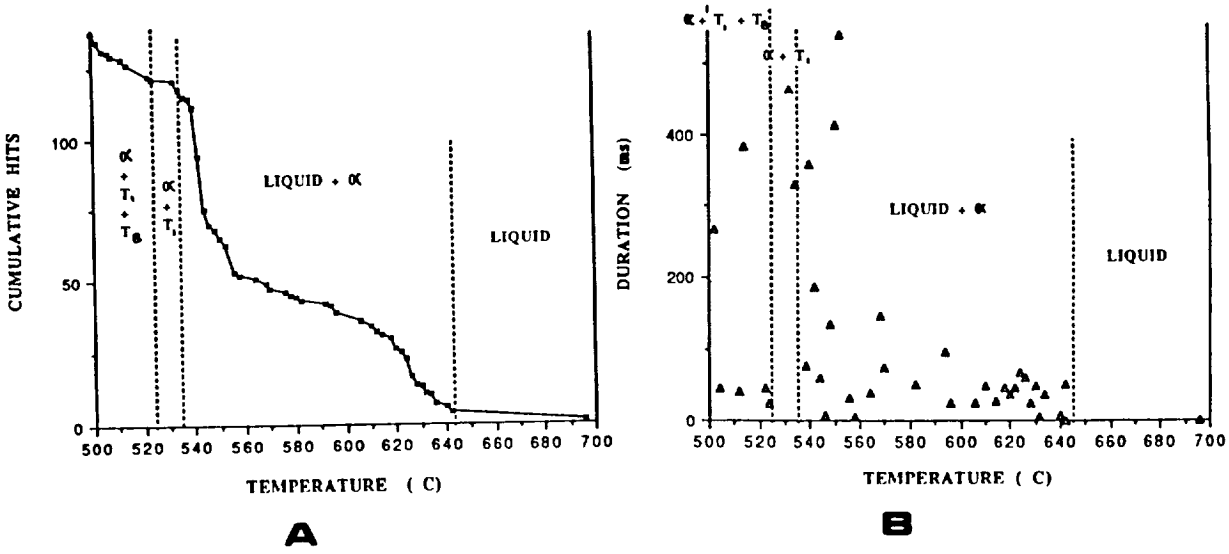

Figure 5.17 Plots of (a) cumulative AE hits and (b) AE signal duration as functions of temperature and phase.

As the mass of the aluminum-lithium alloy was increased from 2.7 to 10.8 g, the local solidification time increased from approximately 350 to 900 seconds. The microstructure was columnar with traces of equiaxed dendritic growth in the center of the casting. The average grain size, in accordance with the ASTM three ring intercept method, increased from 0.22 to 0.33 mm. The large mass experiments were performed in alumina crucibles which adhered to the metal as it cooled. Figure 5.18 is a typical cumulative AE hit v. time plot for a 10.8 g casting. There was minimal acoustic emission activity at the end of solidification. This is explained by the combination of slow and directional grain formation which produces minimal internal stress during solidification and, therefore, few detectable AE hits. In other words, the larger grains

with low angle boundaries contain less potential strain energy than smaller equiaxed grains. It was assumed that the slower grain formation allowed more time for energy dissipation and, since AE is related to the rate of strain energy release, fewer emissions occur during slow grain formation.

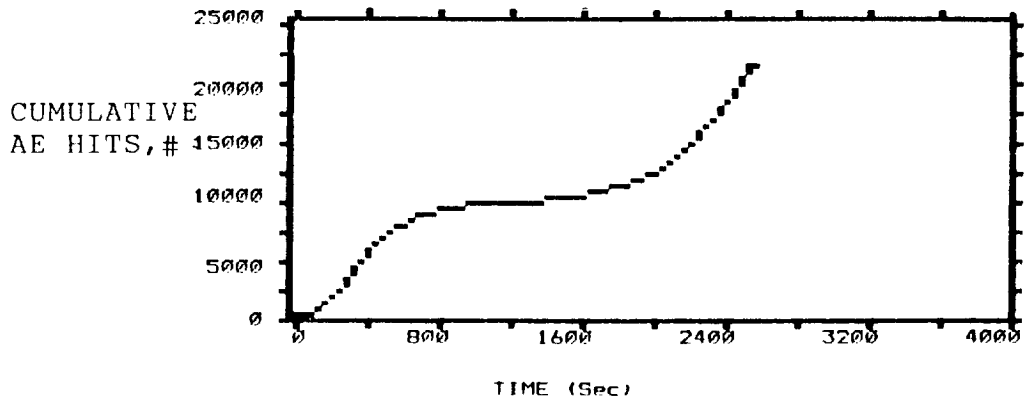

Figure 5.18 Cumulative AE hits v. time during the solidification of a 10.8 g Al-Li alloy.

It can also be seen in Figure 5.18 that there is strong activity beginning at 1,600 seconds which corresponds to 535°C, the solidus, and that it continued to room temperature. As with the pure aluminum, this is attributed to internal tensile stresses induced by the adherence of the casting to the mold wall during volumetric shrinkage. When a boron nitride crucible was used, which does not adhere, there was low level AE activity which was considered a result of continued grain boundary realignment and micro-cracking during final cooling. Although the recording equipment was shut off at 500°C, it is estimated that over 30,000 hits occured by the time the specimen had reached room temperature.

The first period of acoustic emission activity, began at the liquidus (644°C), as the first fraction of solid forms, and continued for approximately five minutes (Figure 5.13) until approximately 20% solid had formed (Figure 5.3). The AE activity at the beginning of solidification did not occur with ultra-pure aluminum, but was evident in every Al-Li alloy test. The only difference in the solidification mechanisms is the formation of interdendritic porosity. In the ultra-pure metal, the hydrogen remains in solution as it is rejected into the adjacent liquid. However, in an aluminum-lithium alloy, it forms micro-pores which become trapped between growing dendrite arms (Section VI, Metallographic Analysis).

It is this microporosity that is proposed to be the source of internal stress responsible for the first period acoustic emission. One source model involves expanding pores which exert force between growing dendrite arms. This force generates dislocation motion in the growing solid particles that are suspended in the stress-free liquid. Another possible mechanism of strain energy release is the micro-cracking of dendrite arms induced by hydrostatic pressure from interdendritic hydrogen.

Initially, the test program was designed to vary the percent of hydrogen in the furnace atmosphere, thereby controlling the percent of porosity in the casting. A series of experiments was done using an inert UHP argon atmosphere before changing to a mixture of argon and 4.1% hydrogen. Al-Li alloy specimens tested in the pure argon all contained a small percentage of porosity (less than 5%) usually concentrated at the bottom of the casting. Since it was then thought that the hydrogen was present in the specimen before testing, the soak time above the liquidus was increased to one hour in UHP argon.

This was to allow the hydrogen to diffuse out of the specimen before cooling. However, this did not eliminate the porosity completely.

The 4.1% hydrogen mixture did not lead to the expected results. Rather than increasing the interdendritic porosity, it caused a turbulent chemical reaction on the top surface of the casting, leaving a grey powder, assumed to be lithium hydride (LiH). The internal porosity was still minor but the AE hits increased two orders of magnitude. The AE activity was attributed to the formation of the powder instead of the porosity. This was verified by testing the ultra-pure aluminum in the 4.1% hydrogen atmosphere. There was no effect on the AE activity as a result of the hydrogen.

The final percent of porosity was not indicative of the total acoustic emission hits. However, as the size of the casting was increased from 2.7 to 10.8 g, the hits in the first period increased by almost a factor of ten (Table 5.2). This is explained by considering the slower growth velocity of the larger casting. Although a larger volume of gas is being evolved in the form of more micropores between growing dendrites. There is also more time for the hydrogen to diffuse out of the specimen and enough available liquid to refill the voids left by the evolved gas. Microstructural analysis of the larger volume specimens reveals interdendritic porosity only in the center of the casting where the hydrogen diffusion path was too large. In the ultra-pure aluminum, where there was no porosity, there was no first period of acoustic emission regardless of the casting size.

Table 5.2 Correlation of AE activity and percent of porosity as a function of mass and composition.

Specimen	Porosity	Atmosphere	AE Hits (1st Period)
Aluminum 2.7 g	0	UHP Ar + 4.1% H	0
Aluminum 5.2 g	0	UHP Ar + 4.1% H	0
Al-Li 2.7 g	less than 5%	UHP Ar + 4.1% H	1,250
Al-Li 10.8 g	less than 5%	UHP Ar + 4.1% H	11,000

The present model describes two periods of AE during the solidification of an Al-Li alloy. The first period, occurring at the beginning of solidification, is attributed to interdendritic porosity, whereas, the second period, occurring at the end of solidification, is controlled by grain boundary formation. The model agrees in part with Feurer and Wunderlin's results [14] for an Al-4.5Cu-0.2Ti alloy (Table 5.3). They also observed a two stage behavior but considered both the AE events at the beginning and the end of solidification to be caused by porosity formation. The present study has shown detectable acoustic emission in porous-free material that is related to grain boundary formation as well as AE at the beginning of solidification as a result of porosity. Porosity may also

contribute to the AE at the end of solidification but its presence is not essential to detecting hits.

Table 5.3 Summary of AE results for the alloy Al-4.5Cu-0.2Ti [14].

Specimen	H_2 Content (cm^3 STP/100g)	Total AE Counts (x 10^4)	Pore Fraction (1.0 = 100%)
A	0.05	1.05	0.19
B	0.17	2.75	0.46
C	0.23	6.35	0.63

The present experiments have also shown no direct relationship between grain size and cumulative acoustic emission hits (Figure 5.19). Instead, it can be concluded that at least two factors control the acoustic emission in solidifying aluminum-lithium alloys. The first is interdendritic porosity controlled by a combination of the initial hydrogen concentration and the material's ability to evolve the gas without generating micropores. The second is the degree of internal stress present at the end of solidification. This internal stress is influenced by the rate of heat extraction and, therefore, grain size and alignment.

As was done in the analysis of pure aluminum, four conventional AE parameters are now presented as functions of time (Figure 5.20) and amplitude (Figure 5.21) in order to identify trends that may characterize AE sources. A similar pattern is seen for the Al-Li

alloy: higher amplitude, rise time, duration and energy during the periods of high AE activity. In the case of Al-Li alloys this happens to be at the beginning as well as the end of solidification. As can be seen, there was nothing distinctive about these two periods. Continued low level activity occurred after solidification which is considered a result of continued grain boundary realignment during cooling. An additional period of high activity occurred if the specimen adhered to the mold wall due to imposed stresses during shrinkage. It is concluded from the analysis of this test and several others that AE sources during solidification of aluminum-lithium alloys cannot be identified by parameters related to waveshape. On the other hand, the complementary use of cumulative hit data, thermal analysis, and metallography were effective in finding that interdendritic porosity and grain boundary formation are solidification mechanisms that generate acoustic emission during the same experiment.

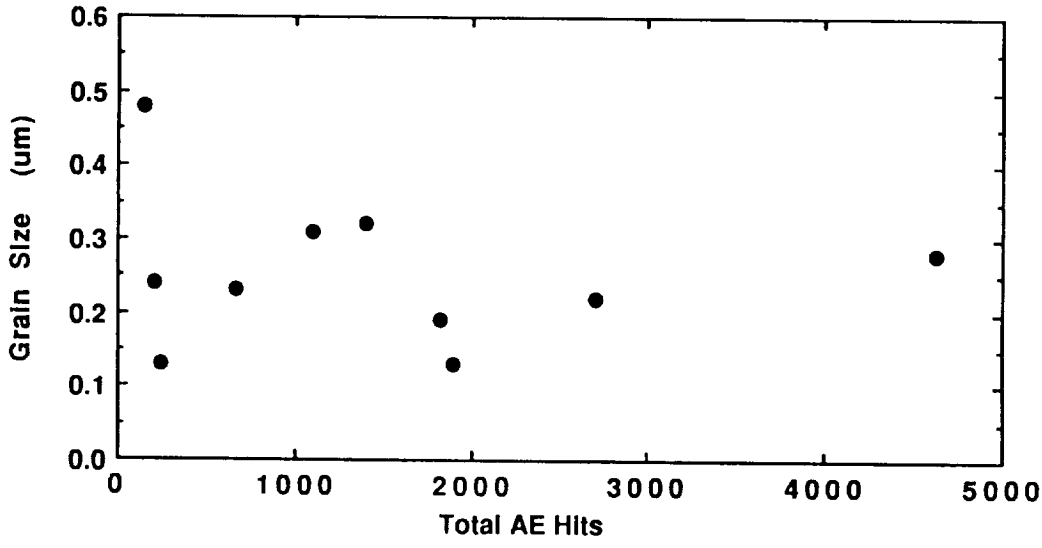

Figure 5.19 Grain size v. AE hits for 2.7 g Al-Li alloy castings with columnar and equiaxed grain structure.

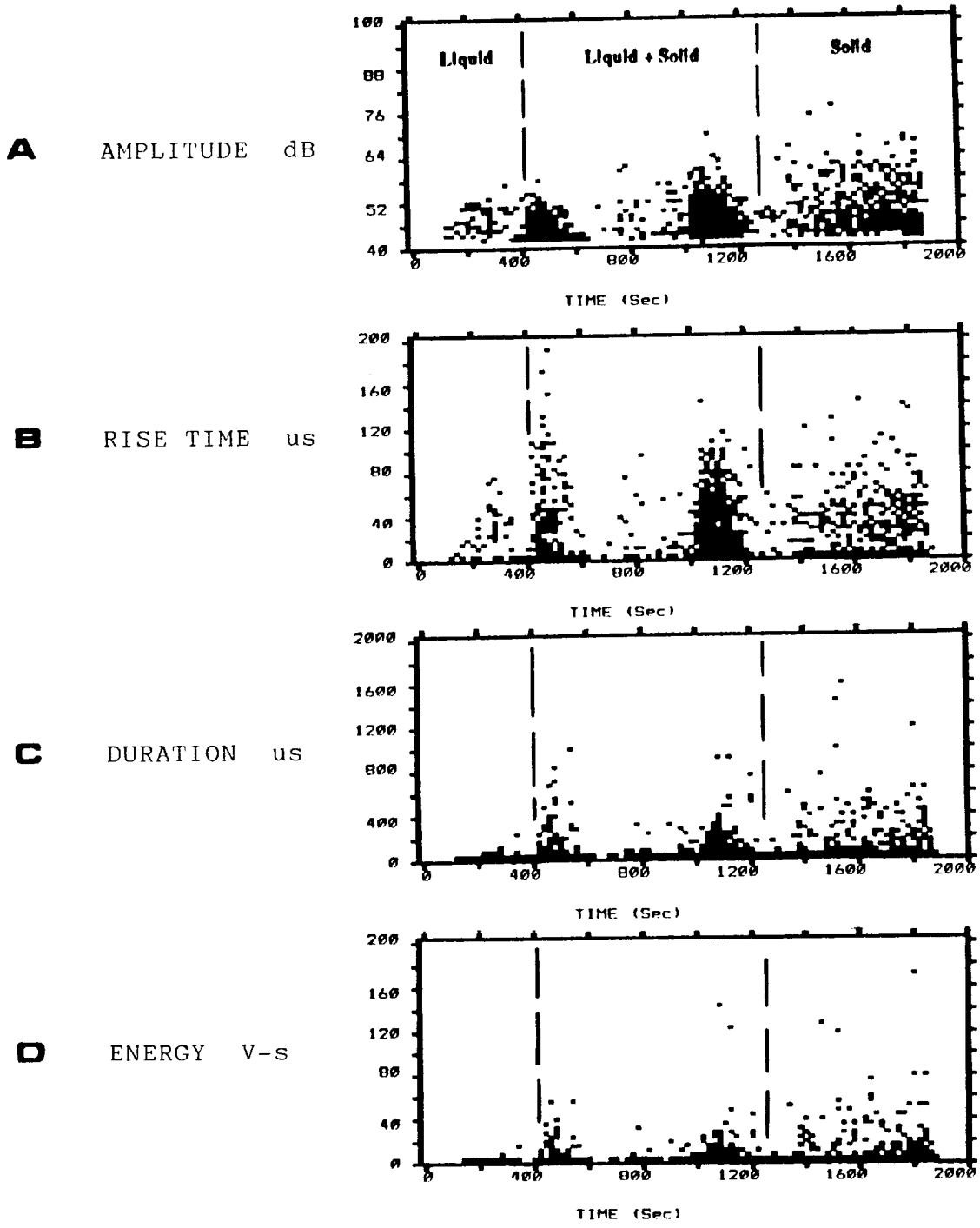

Figure 5.20 Acoustic emission (a) amplitude, (b) rise time, (c) duration, and (d) energy as a function of time during the solidification of an Al-Li alloy.

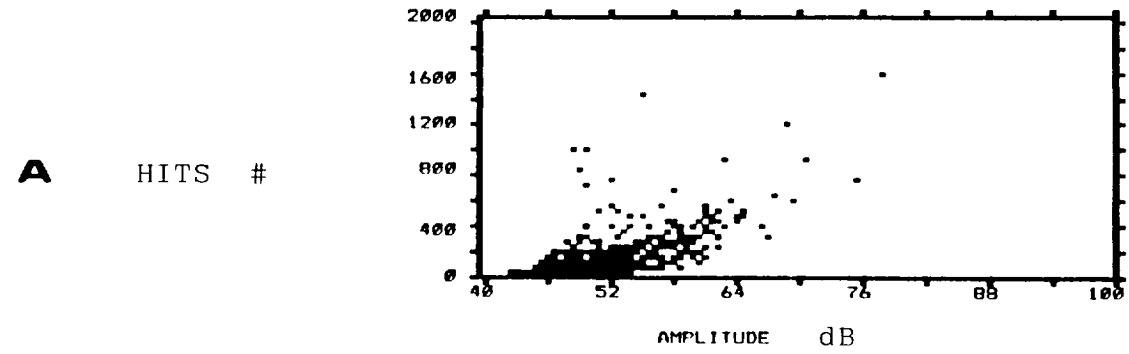

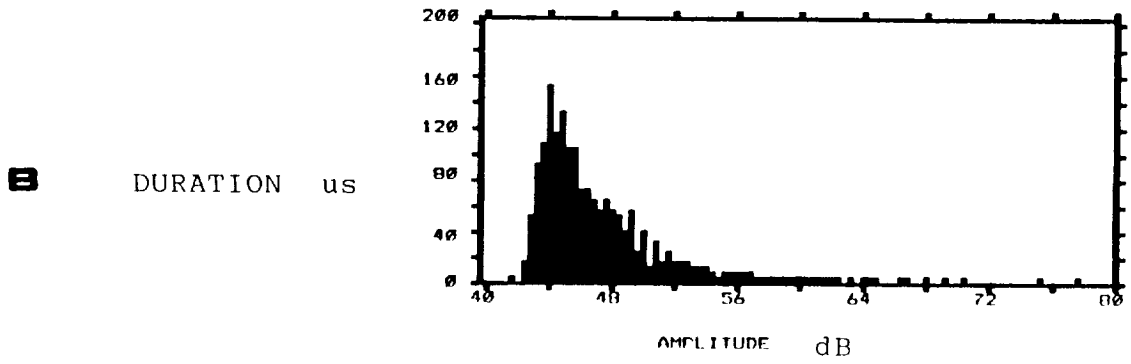

Figure 5.21 Acoustic emission (a) hits and (b) duration as a function of amplitude during solidification of an Al-Li alloy.

5.4.2 Waveform Analysis

Individual AE signals were recorded periodically during the solidification of the Al-Li-Cu alloy. As with the pure aluminum, the intent was to determine waveform characteristics that could distinguish AE sources. Figure 5.22 illustrates four signals: the first two occurred during the first period of high activity and the second two during the second period of activity in a solidification experiment. It was difficult to distinguish features in the time domain, as was expected, therefore, frequency domain analysis was used.

The frequency spectra are noticeably different than they were for the pure aluminum tests (Ref. Figures 5.10 and 5.12). Rather than a prominent resonant peak at 11,000 or 8,200 Hz, the main spectral components are located within a narrow bandwidth centered at 200 kHz. This discrepancy can be explained by understanding that the Al-Li experiment used a 100-H filter and the pure aluminum tests did not. Therefore, in the former test, the waveguide effects are filtered out and the 11,000 (or 8,000 Hz) component and its harmonics are suppressed. By referring back to Figure 4.4, it can be seen that the S9208 transducer, used in the Al-Li alloy test, had a resonant frequency peak at 200 kHz. Instead of the spectrum being dominated by the waveguide response, in this case, it is dominated by the transducer.

In conclusion, individual waveform analyses in the time and frequency domains were unable to distinguish the AE source in the first period, attributed to interdendritic porosity, from that of the second period, attributed to grain boundary formation. If the low

frequency components are filtered out, the response of the transducer dominates; whereas, if filtering is not used, the waveguide response dominates.

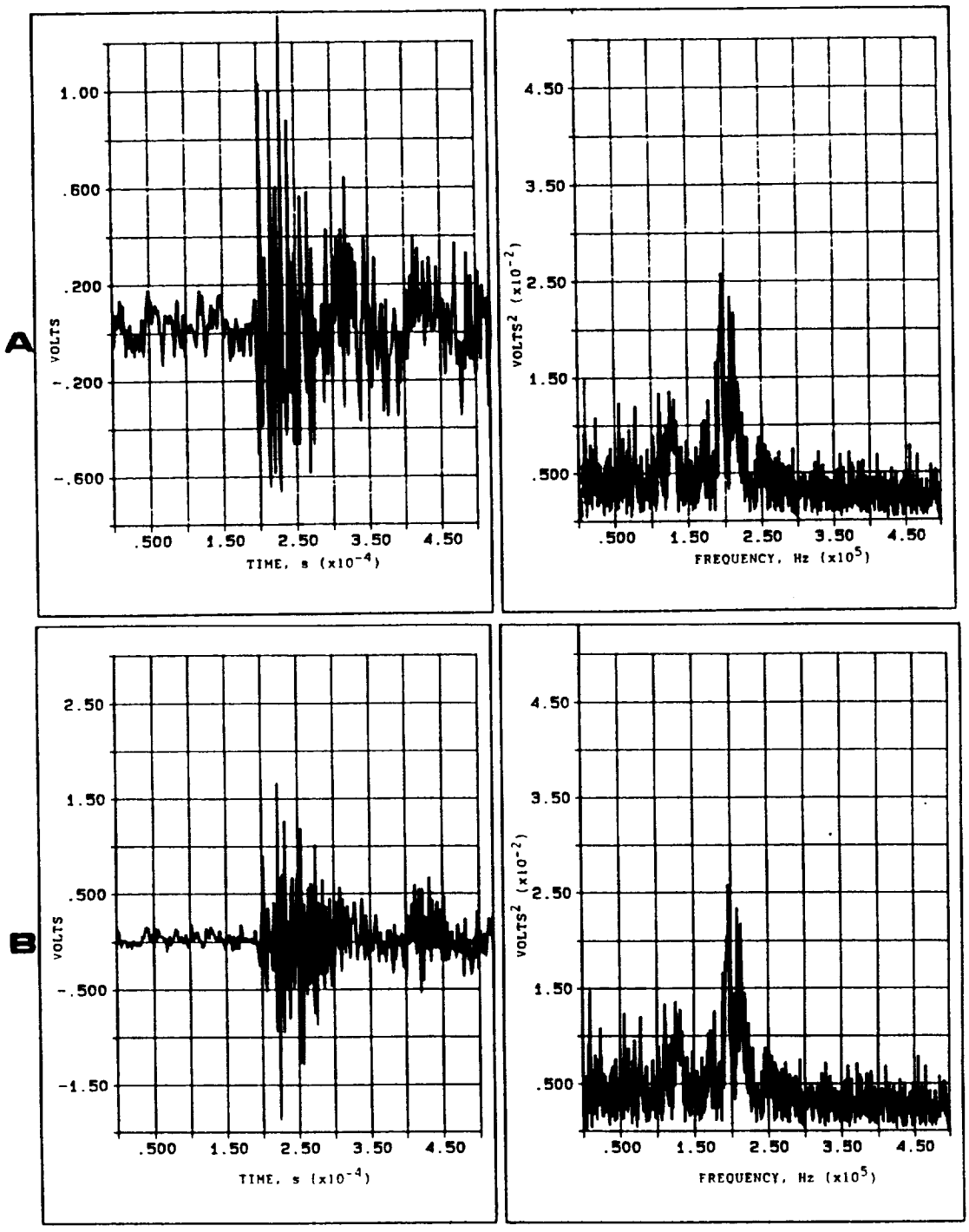

Figure 5.22 Time and frequency domain analysis of four signals recorded during solidification of an Al-Li alloy. (a and b) illustate the first period of AE activity and (c and d) the second period of AE activity.

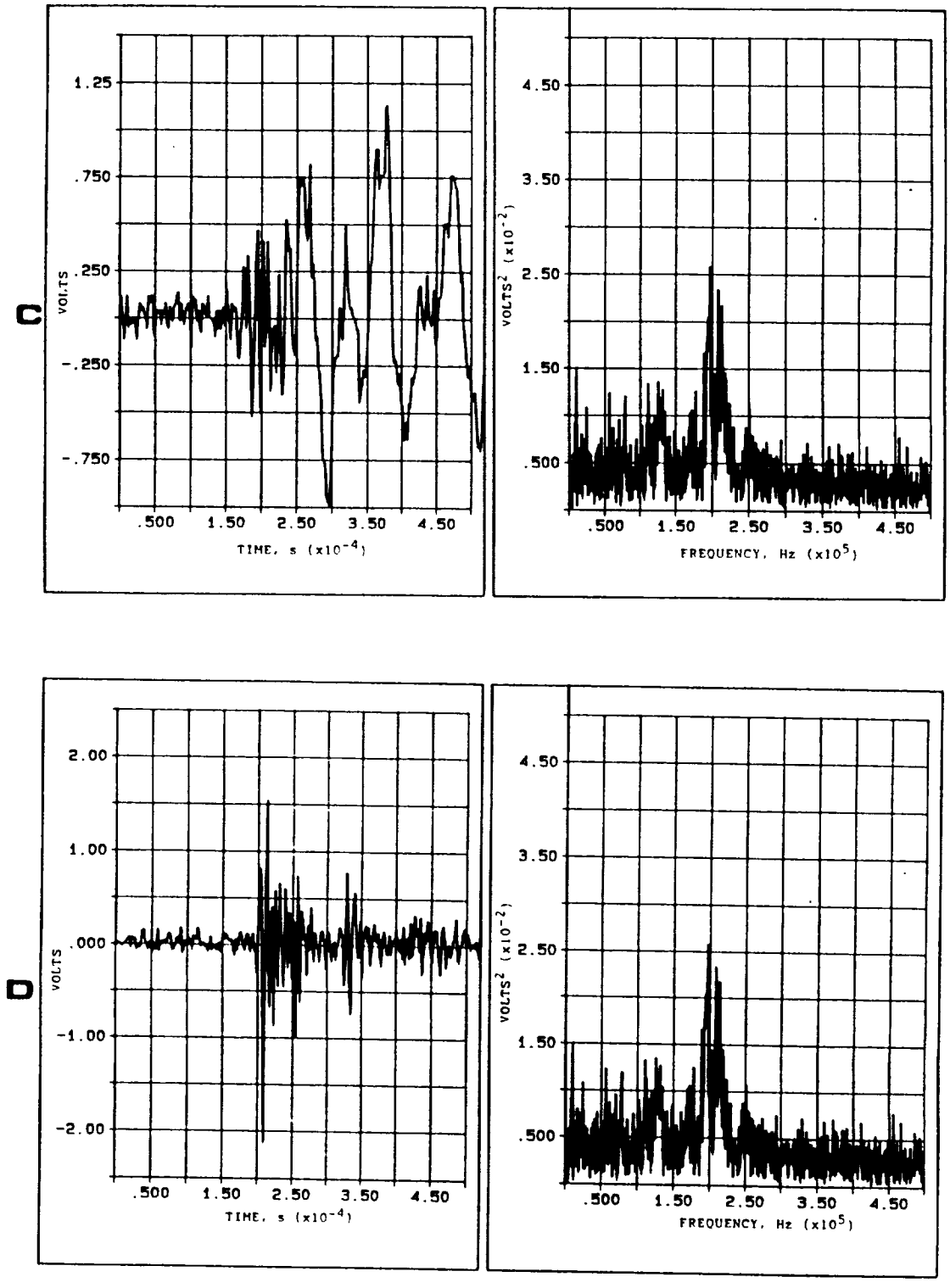

Figure 5.22 Continued.

5.5 Acoustic Emission from Aluminum-Copper Alloy Castings

5.5.1 Conventional Analysis

The acoustic emission pattern of aluminum-copper alloys (Figure 5.23) is similar to aluminum-lithium alloys (Figure 5.14). There is a two stage behavior with high AE activity periods at the beginning and end of solidification. The average number of hits, 255, was low compared with 1,050 for Al-Li alloys tested under similar conditions. The percent, in general, was also lower in the Al-Cu alloy (Figure 6.9) as compared to the Al-Li alloy.

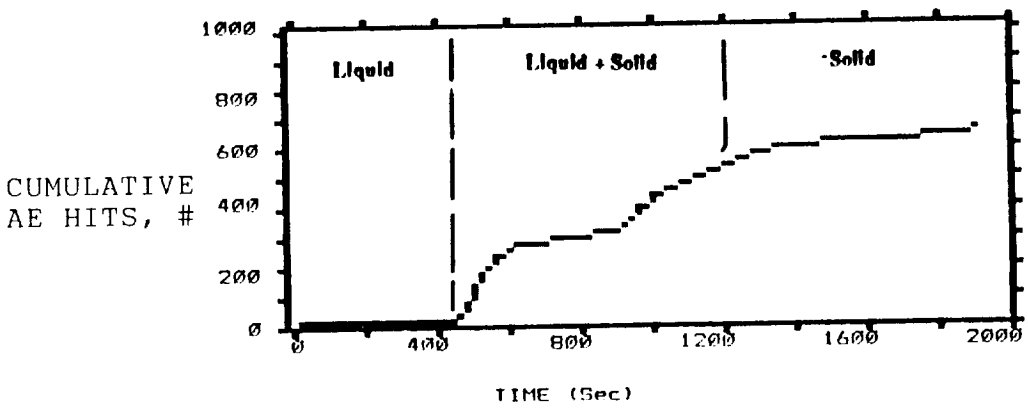

Figure 5.23 AE activity v. time during the solidification of a 2.7 g Al-4.7w% Cu alloy.

Most of the experiments with this alloy were performed to adjust the AE gain and threshold settings, calibrate the temperature measurement system, and record individual waveforms throughout the solidification range. Because of the variations in test settings, it was difficult to compare data. The results, however, do support the conclusion that alloys have two discrete AE periods: one beginning at the liquidus and continuing to approximately a 0.2 solid fraction and the other beginning at roughly 0.9 solid fraction and ending at the solidus.

Because of the low number of hits per test, plots of the conventional AE parameters for the Al-Cu alloy, as functions of time (Figure 5.24) and amplitude (Figure 5.25), do not show the clustering seen for ultra-pure aluminum (Figures 5.6 and 5.7) or the Al-Li alloy (Figures 5.20 and 5.21. As a result, little information about trends in acoustic emission signal parameters could be derived from conventional analysis for the Al-Cu alloy. No distinction could be made between the types of signals generated during the first and second periods of AE activity.

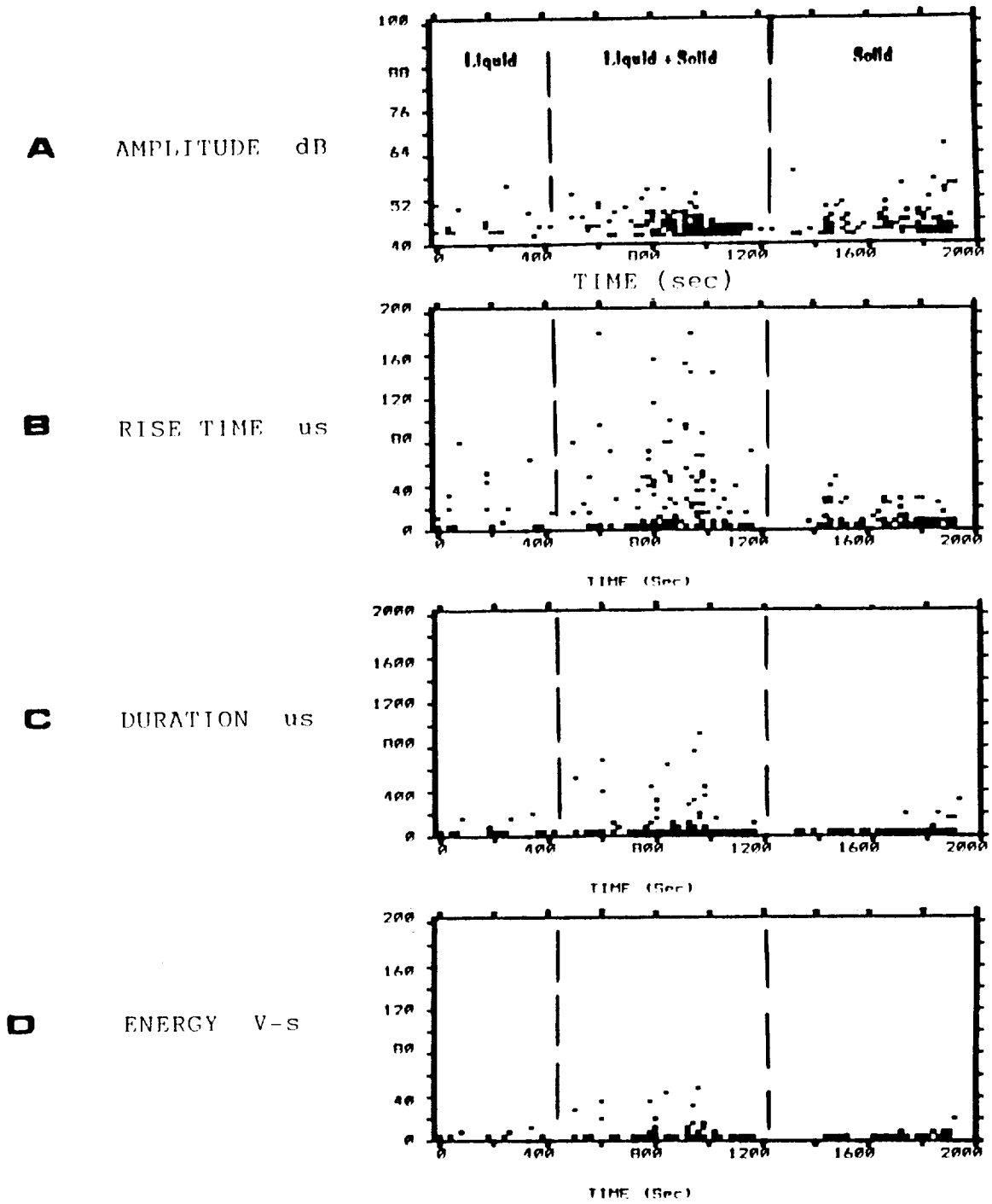

Figure 5.24 Acoustic emission (a) amplitude, (b) rise time, (c) duration, and (d) energy as a function of time during the solidification of an Al-4.7wt%Cu alloy.

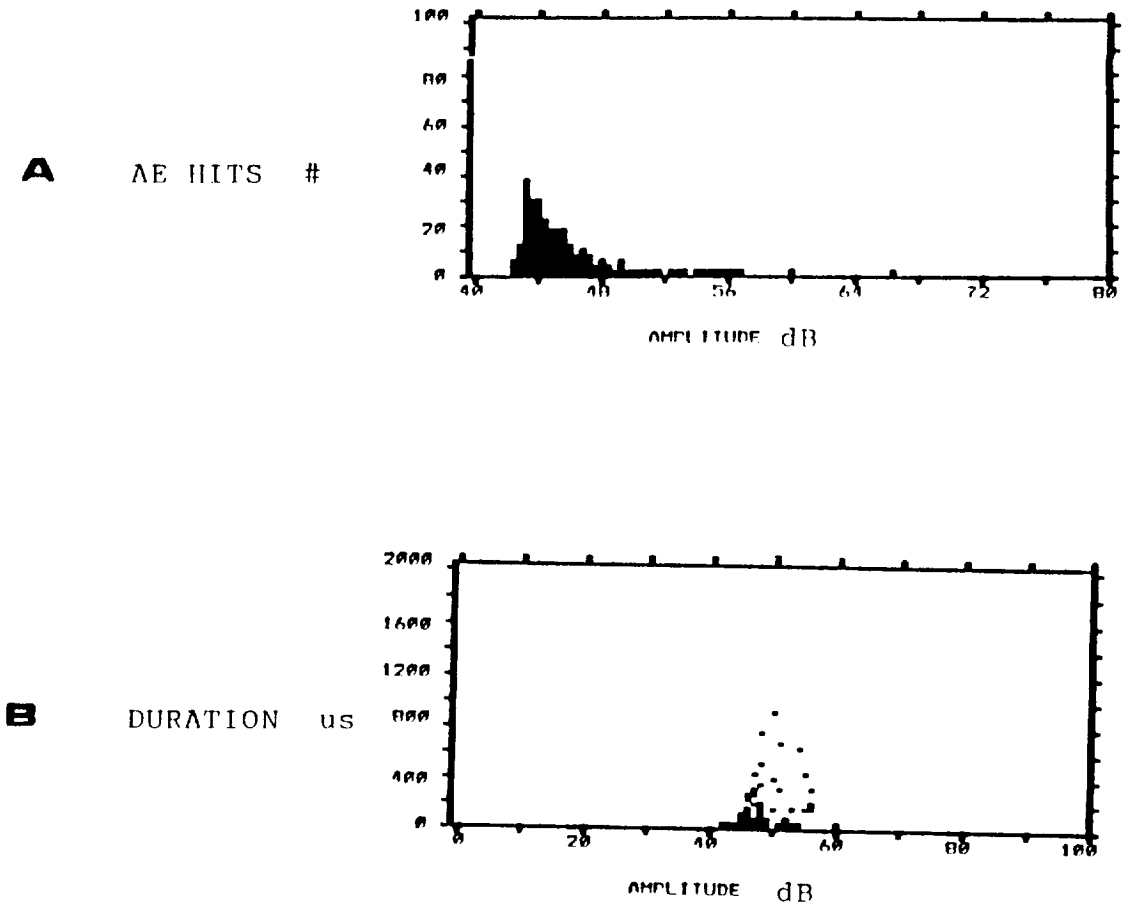

Figure 5.25 Acoustic emission (a) hits and (b) duration as a function of amplitude during solidification of an Al-4.7wt%Cu alloy.

5.5.2 Waveform Analysis

Individual waveform analysis of acoustic emission signals generated during a solidification experiment with an Al-4.7wt%Cu alloy provided information similar to that from the Al-Li alloy (Section 5.4.2). In the case of the Al-Cu alloy, a PAC R6I resonant-type transducer was used with a 100-H filter. Figure 5.26 illustrates, in the frequency domain, that the 60 KHz resonant component of the transducer dominates. The low frequency component of the waveguide is suppressed by the filter and the AE source component is indistinguishable. The first two plots (a & b) were recorded during the first period of AE activity and the second two plots (c & d) were recorded during the second period. No distinction can be made for one set of signals from the another.

Although this is again only an example from one test, similar results were obtained in other tests. The high frequency components of the transducer, caused by resonance, dominate the power spectrum when the low frequency resonance components of the waveguide are suppressed by filtering. In conclusion, individual waveform analysis was unable to distinguish AE sources in the first and second periods of AE activity and it was unable to characterize features of the source signals.

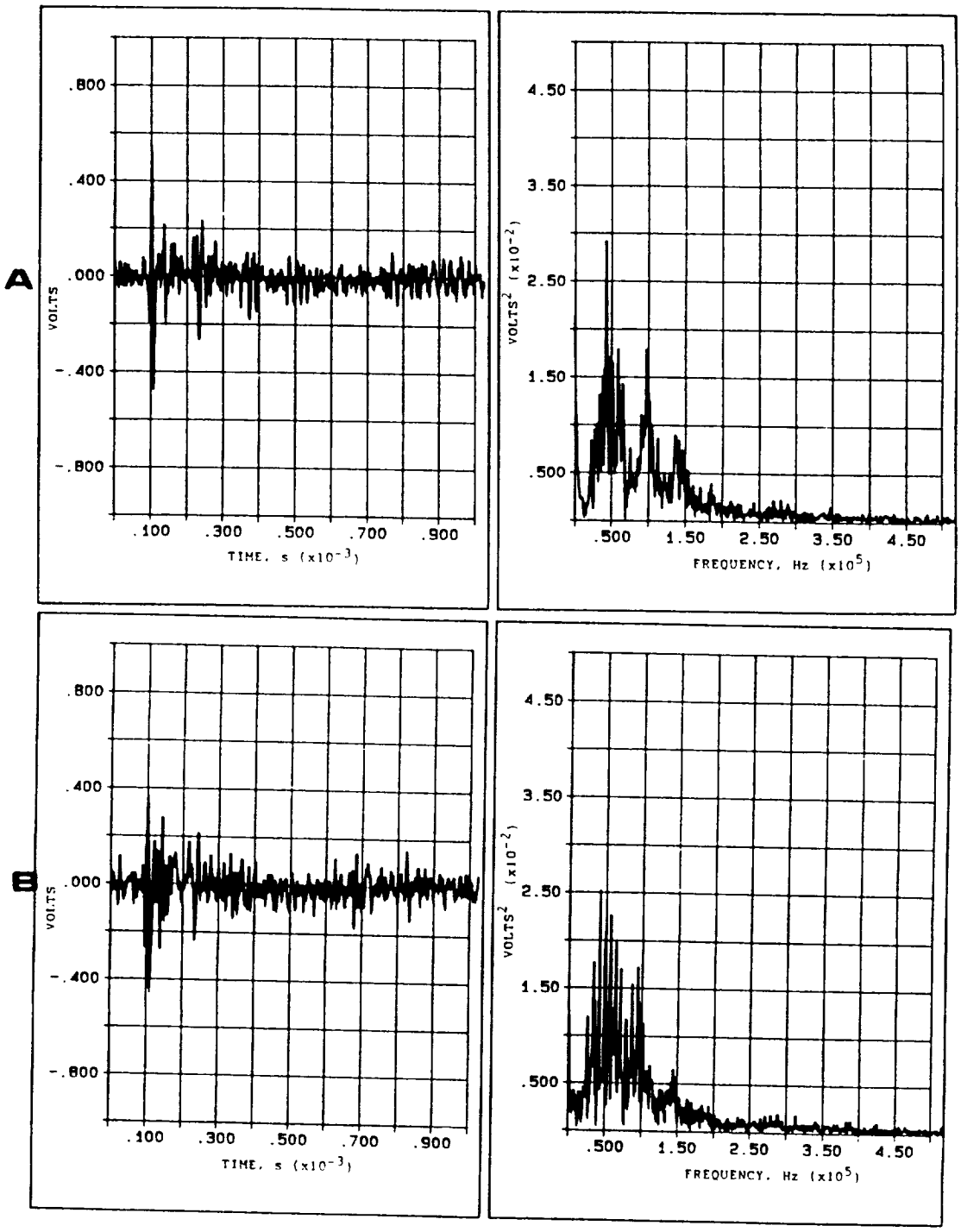

Figure 5.26 Acoustic emission signals recorded from (a & b) the first period of AE activity and (c & d) the second period during the solidification of an Al-4.7wt%Cu alloy.

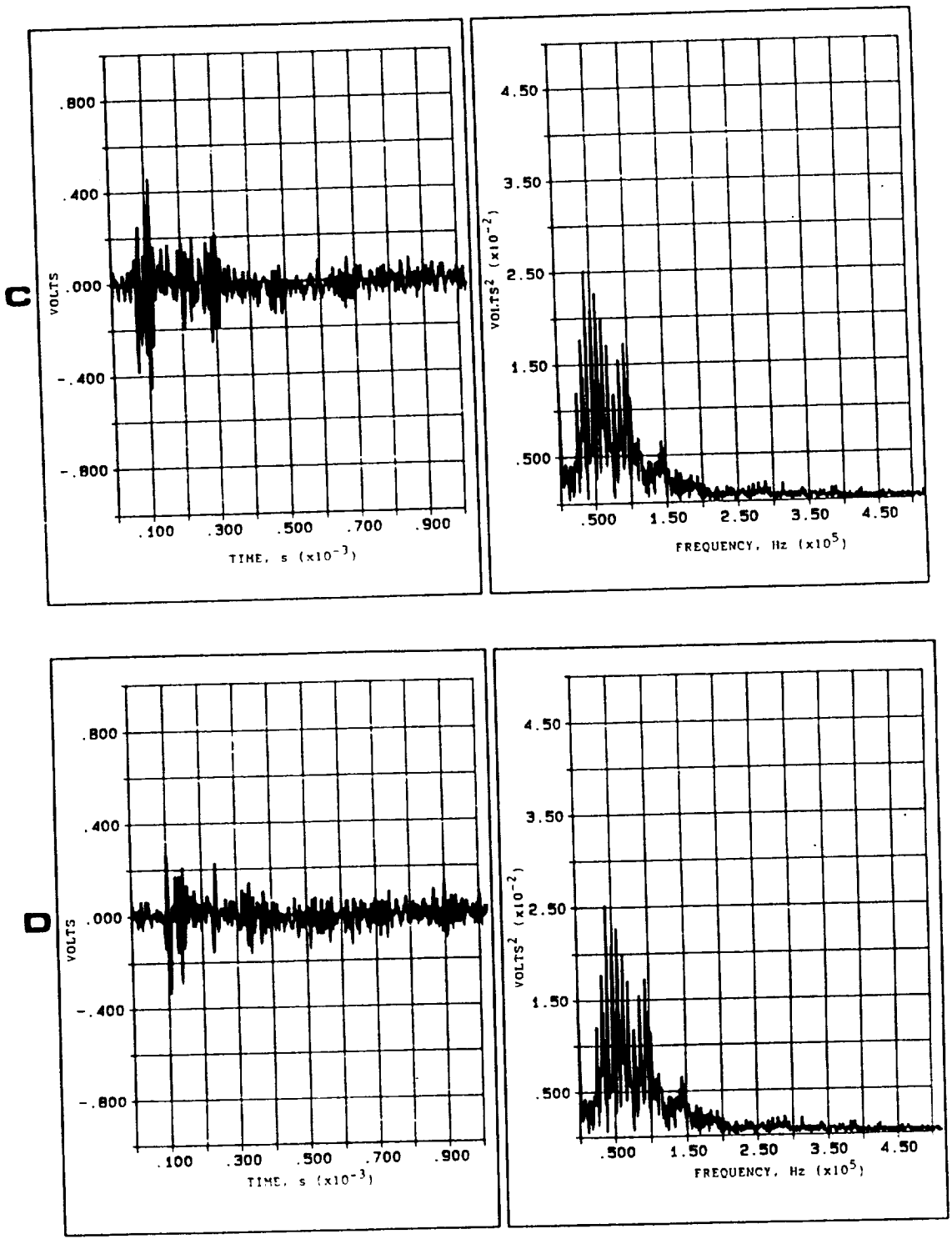

Figure 5.26 Continued.

5.6 Summary of AE During Solidification

It has been shown that AE from ultra-high purity aluminum occurs as the last fraction of solid forms. A model was presented that suggests source mechanisms include dislocation creep and grain boundary sliding generated by compressive stresses as grain boundaries form at a high temperature. As the volume of the casting increases, the pattern remains the same although the number of hits increases. No relationship was found between the number of grains and the number of hits. Other factors which affected the number of hits included the integrity of the melt-crucible coupling and the threshold selected for AE detection.

A different AE pattern was realized for an Al-Li alloy. A period of high activity coincides with the beginning of solidification (prior to 20% fraction of solid). The system was then quiet until the second period began near the end of solidification (above 90% fraction of solid). A model has been presented which describes interdendritic porosity as the AE source mechanism during the first period. Internal stresses, as described for the pure aluminum, are also considered a source mechanism in the second period of the Al-Li alloy's AE activity; solidification cracking also contributes to the total AE events. The percent of hits in the second period were reduced as the grain structure changed from equiaxed to columnar. It was explained that less strain energy would be released during the formation of the columnar grains because of less internal stresses and would, therefore, have less potential of generating acoustic emission. Increasing the volume of the casting increased the number of hits in the first period but had no effect on the second period.

For comparison with the Al-Li alloy, an Al-4.7wt%Cu alloy was tested. The two stage behavior, although less pronounced, was observed. Porosity was low in the Al-Cu alloy as was the number of hits in the first period of AE activity. The low number of hits in the second period was considered a consequence of less grain boundary realignment and virtually no micro-cracking in the lithium-free Al-Cu alloy. When the volume of the specimen doubled, very few hits were recorded. This may be explained by non-porous grains which formed more slowly in the larger specimen and, therefore, had less internal stress during the final moments of solidification.

It should be noted that there was an increase in AE activity for all three materials after complete solidification if an alumina crucible was used. The specimens were observed, after testing, to have adhered to the alumina and this AE activity is believed to be induced by tensile stresses from the restrained aluminum as it cooled to room temperature. When non-wetting boron nitride crucibles were used, there was low level acoustic emission after solidification which was attributed to continued grain boundary realignment during shrinkage.

VI. METALLOGRAPHIC ANALYSIS

6.1 Ultra-pure Aluminum

Metallographic analysis of ultra-pure aluminum was difficult because of its low hardness and minimal impurities. The inherent softness caused smearing of the matrix across grain boundaries during polishing, thereby making etching ineffective for grain boundary studies. The lack of other constituents, which would normally be segregated at the grain boundaries, also made preferential etching ineffective. Several techniques were used in an attempt to exemplify the equiaxed grain structure of the castings. Among others, an electrolytic etch using Barker's reagent was performed, followed by optical study with cross-polarized light. Results of an unetched specimen in Figure 6.1 illustrate a typical microstructure with a surface that is non-porous, as were all of the ultra-pure aluminum specimens, with only a few voids at the grain boundaries. Figure 6.2 illustrates the equiaxed dendritic microstructure that was present during grain boundary formation. The angles of interference between adjacent dendrites, which lead to the development of internal stresses, may also be observed.

In all of the UHP aluminum specimens that were studied, there was no evidence of interdendritic or intergranular porosity, inclusion cracking, or solidification cracking. The optical metallography supports the proposed model for acoustic emission in UHP aluminum (Section 5.3.1). That is, by comparing the conventional AE data with the microstructural details and then considering the solidification kinetics (Section 5.2), it can be concluded that internal stresses developed during the final stage of grain boundary formation result in dislocation motion which generates acoustic emission.

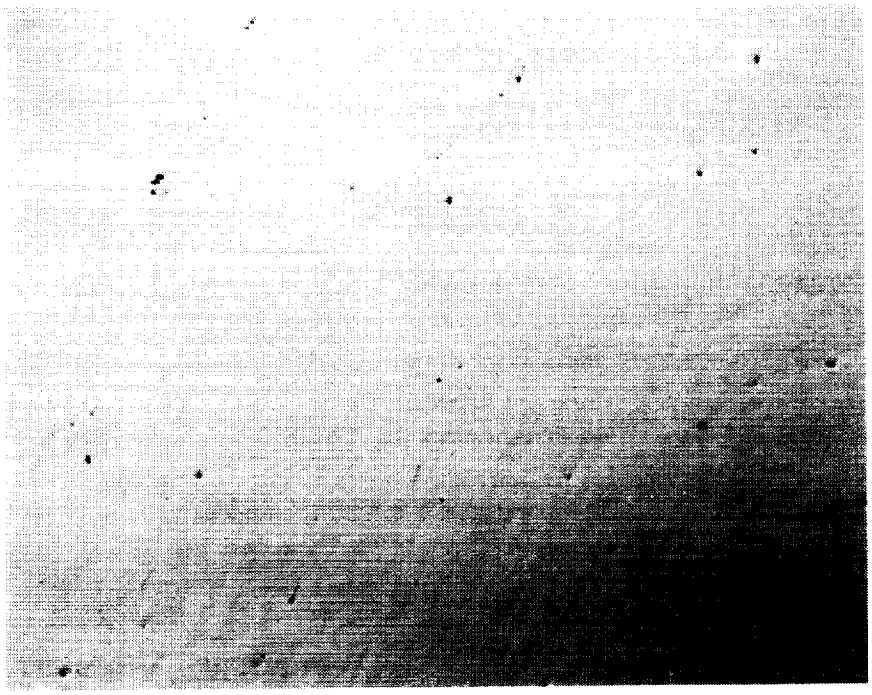

Figure 6.1 Microstructure of UHP aluminum (unetched, 32x)

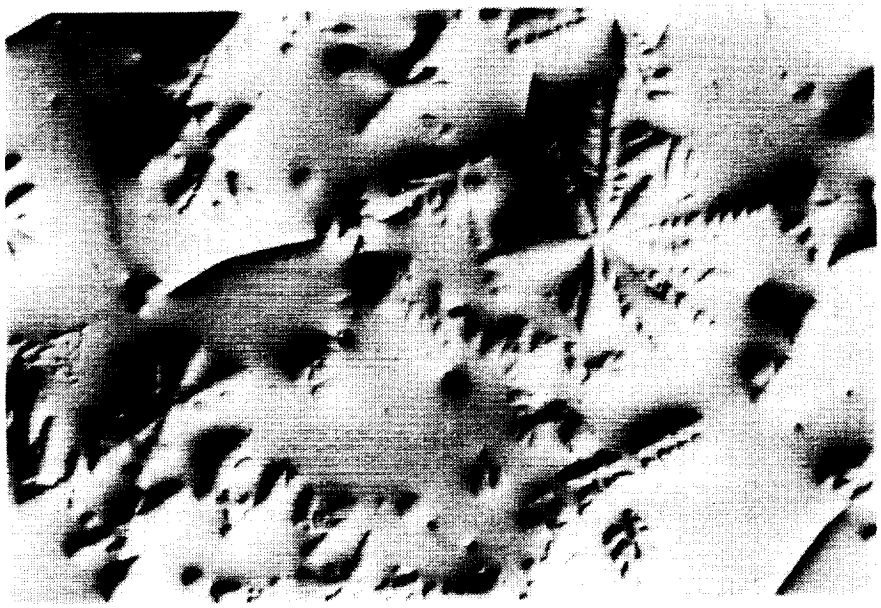

Figure 6.2 Equiaxed dendritic growth of nuclei in UHP aluminum (Kellers, 32x).

6.2 Aluminum-Lithium Alloy

The large degree of interdendritic porosity in the AA2090 Al-Li alloy casting is shown in Figure 6.3. Although the porosity was not this extensive in all castings, it was virtually impossible to eliminate in the Al-Li alloy experiments of the present study. The dendritic structure of Figure 6.3 appears to have been a mixture of columnar and equiaxed growth. A second illustration of the columnar dendritic growth is shown in Figure 6.4. Finally, a comparison of the equiaxed and columnar grain structures is shown in Figure 6.5 (a) and (b), respectively, although the grain boundaries in the latter are difficult to distinguish. Figure 6.6 clearly shows, at three magnifications, the presence of additional phases dispersed throughout the matrix. At least two phases are known [70] to form during solidification (Section 3.3.1): the Θ(AlLi) +T_1(Al_2CuLi) binary eutectic phase and the Θ + T_1 + T_B($Al_{7.5}Cu_4Li$) ternary eutectic phase. It was not, however, necessary to distinguish them in the present study.

It was considered important to know whether or not solute segregation to the dendrite tips, as described in Section 2.2.1, was responsible for a mechanism, such as solidification cracking, that would cause acoustic emission. Therefore, elemental x-ray mapping of aluminum, copper, iron, and zirconium, as shown in Figure 6.7(a-d), respectively, were performed. As expected, the copper concentration was higher between the dendrites and at the tips, as indicated by the orange regions, than in the centers of the dendrites, the green regions. There was also a high concentration of copper in the eutectic phases observed between dendrites, again as expected. The zirconium was uniformly dispersed throughout the aluminum matrix and the iron, surprisingly, was concentrated in a

secondary phase. From this it can be concluded that the interdendritic regions, high in copper, are more brittle than the aluminum matrix

and, therefore, would be sensitive to solidification cracking, especially in the presence of hydrogen gas pressure within the interdendritic pores. These effects are shown in Figures 6.8 (a-d). Examples of dendrite tip fracture, coring, interdendritic porosity and longitudinal microcracking along the dendrite tip arms are seen in Figure 6.8(a) with additional examples in (b-d).

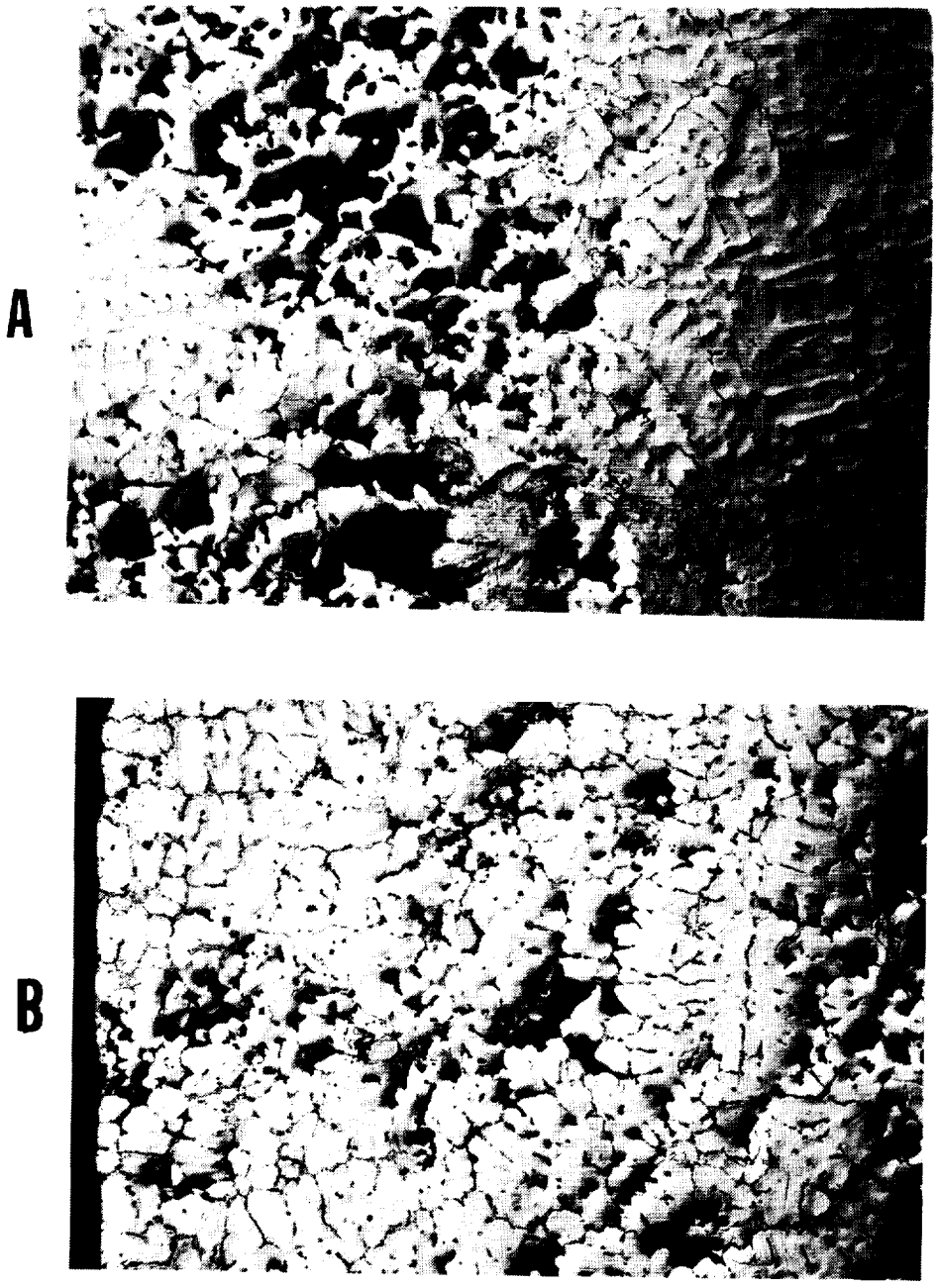

Figure 6.3 Interdendritic porosity in (a) the center and (b) the bottom of an Al-Li alloy casting (both Keller's Reagent, 32x).

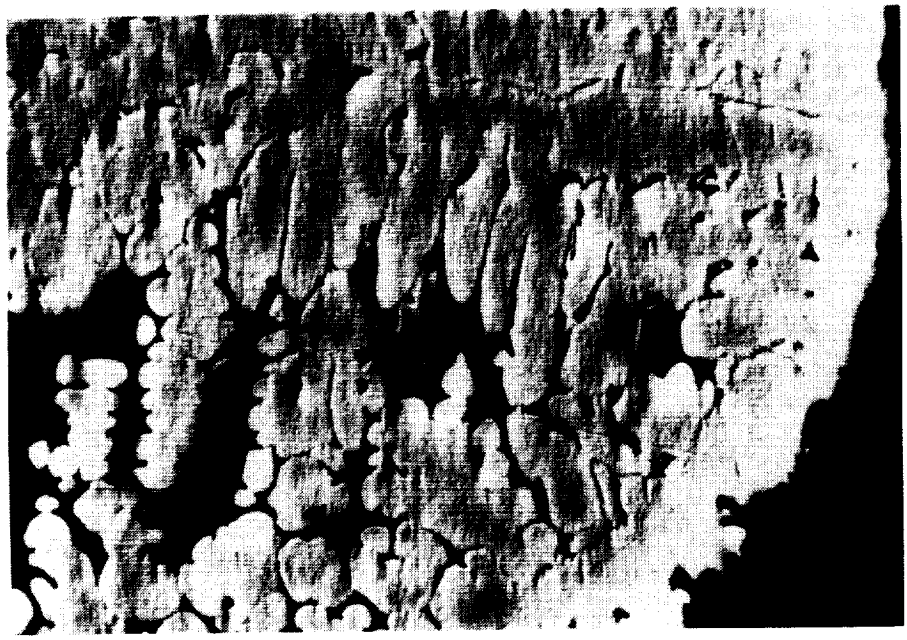

Figure 6.4 Illustration of columnar dendritic growth in an Al-Li alloy casting (Keller's Reagent, 32x).

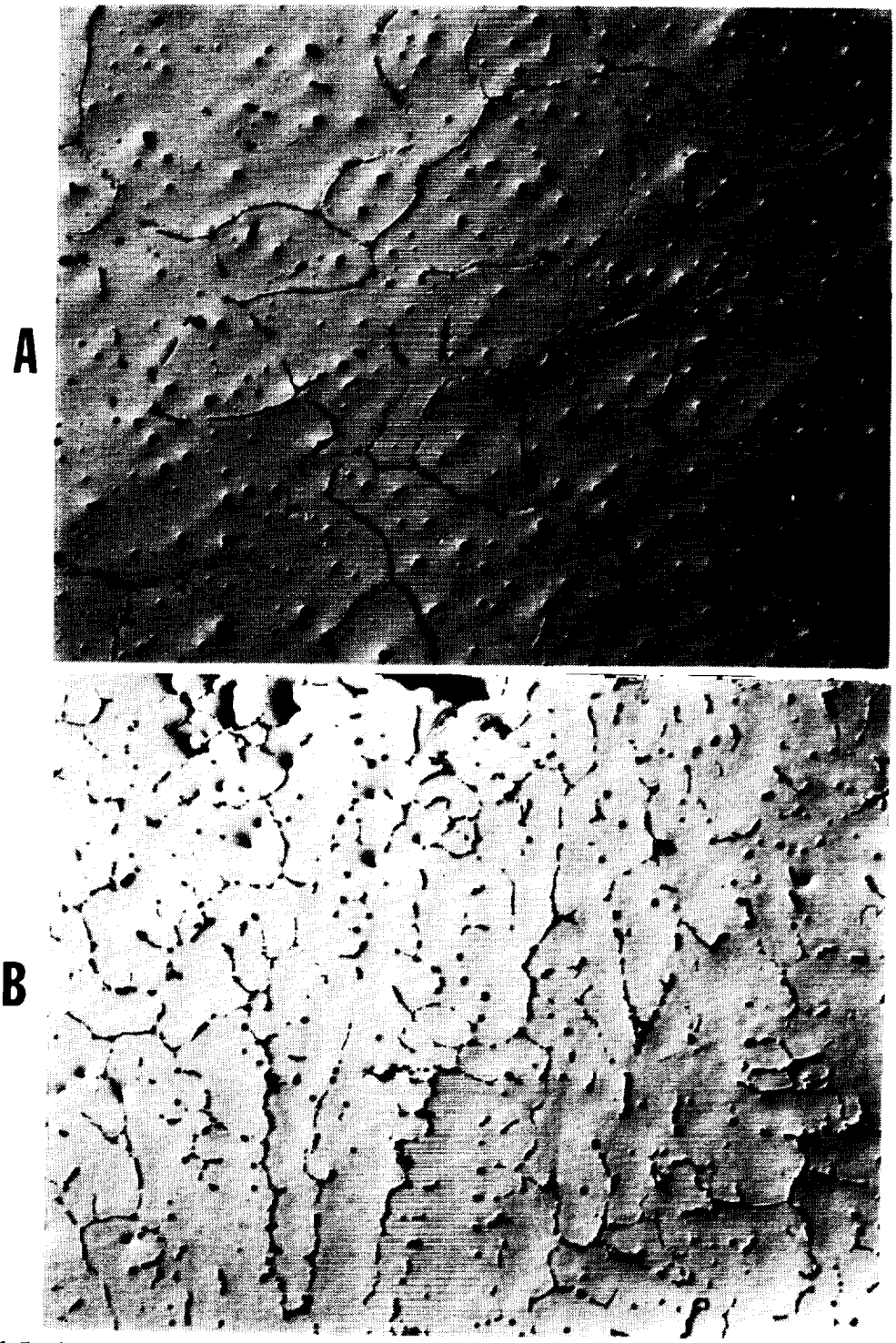

Figure 6.5 Comparison of (a) equiaxed and (b) columnar grain structure in two Al-Li alloy castings solidified under different heat extraction conditions (both unetched, 32x).

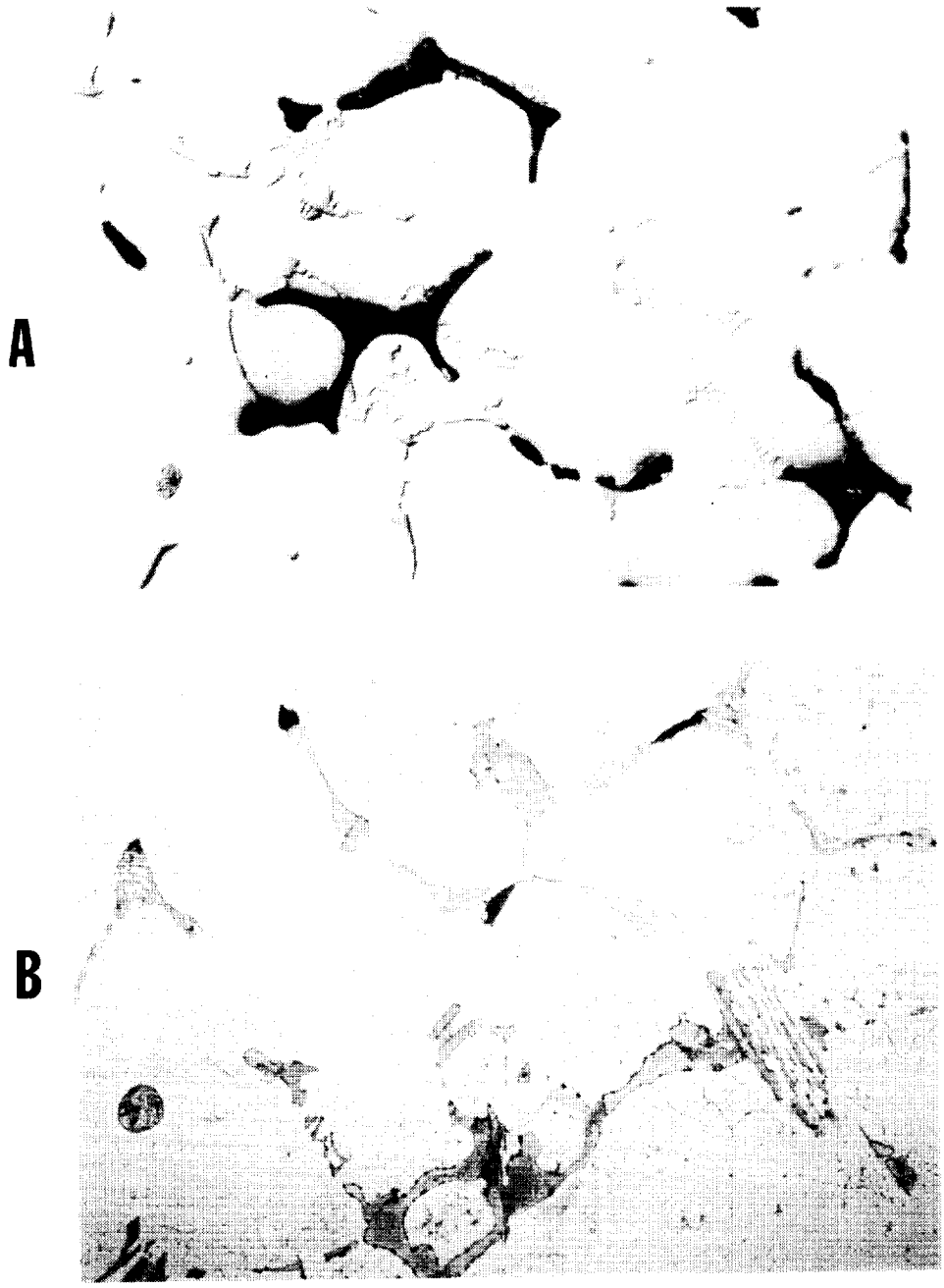

Figure 6.6 Microstructure of an Al-Li alloy at (a) 32x, (b) 100x and (c) 320x illustrating the presence of additional phases dispersed throughout the matrix (Keller's Reagent).

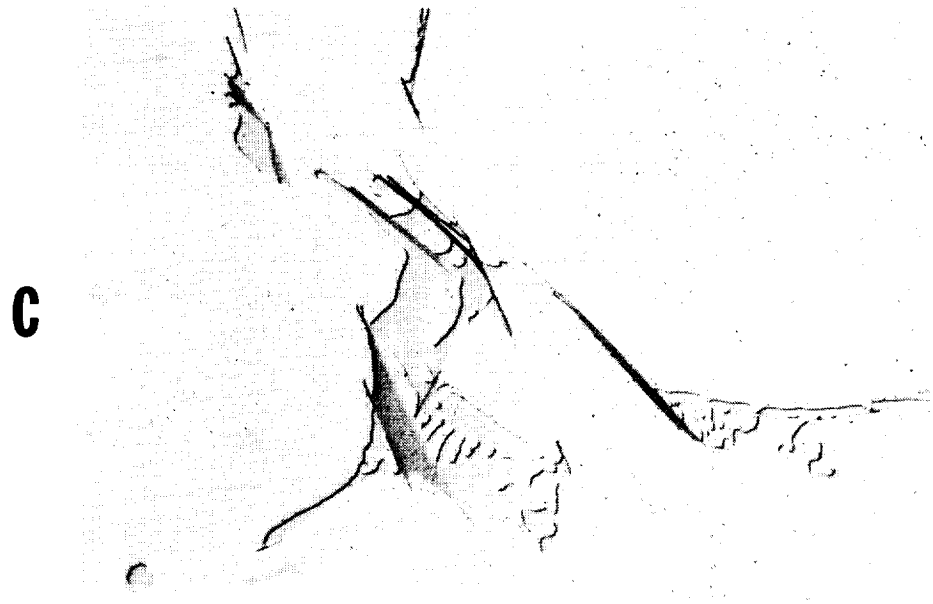

Figure 6.6 Continued.

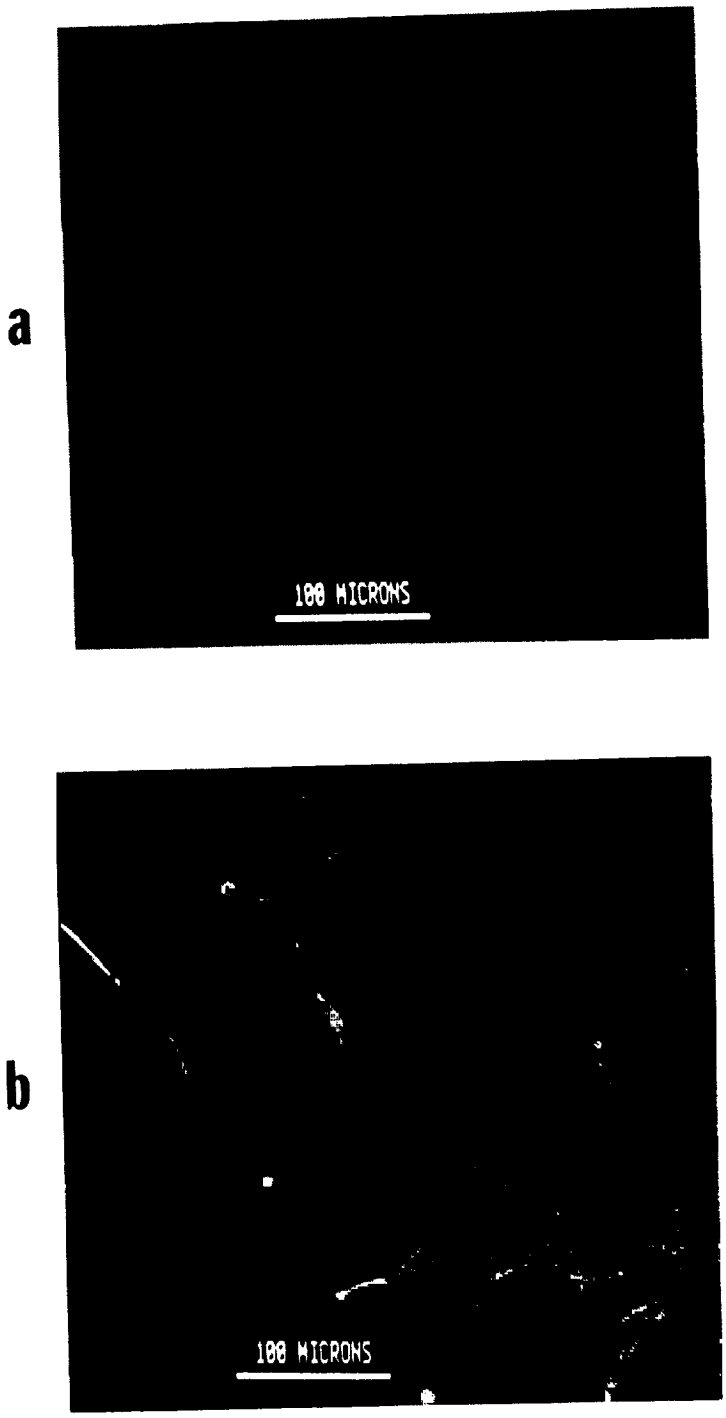

Figure 6.7 Elemental x-ray microprobe maps of relative (a) aluminum, (b)copper, (c) iron and (d) zirconium concentrations in an Al-Li alloy casting.

c

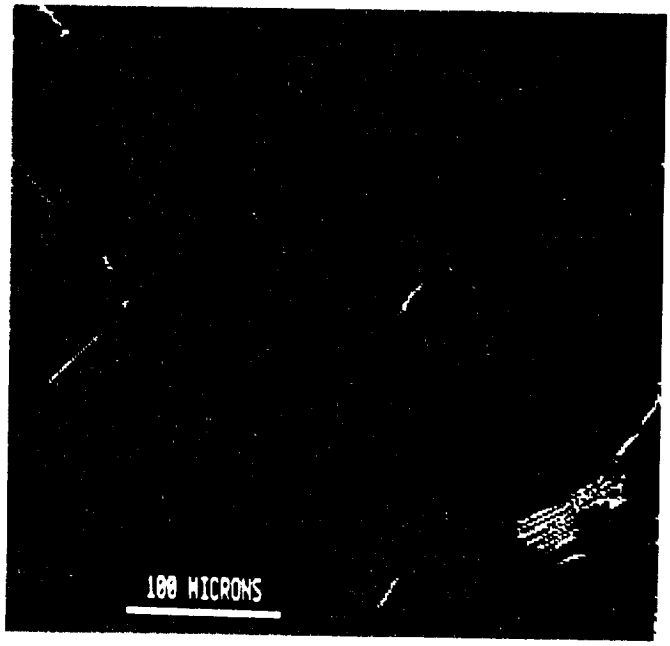

d

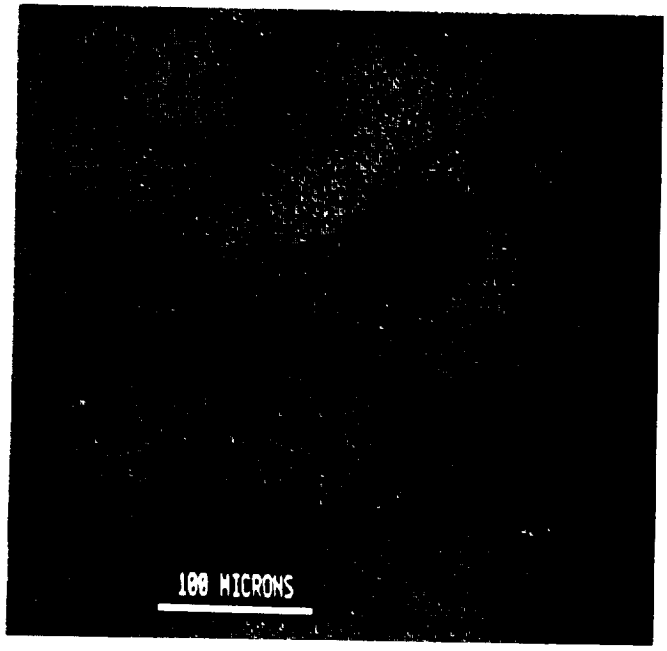

Figure 6.7 Continued.

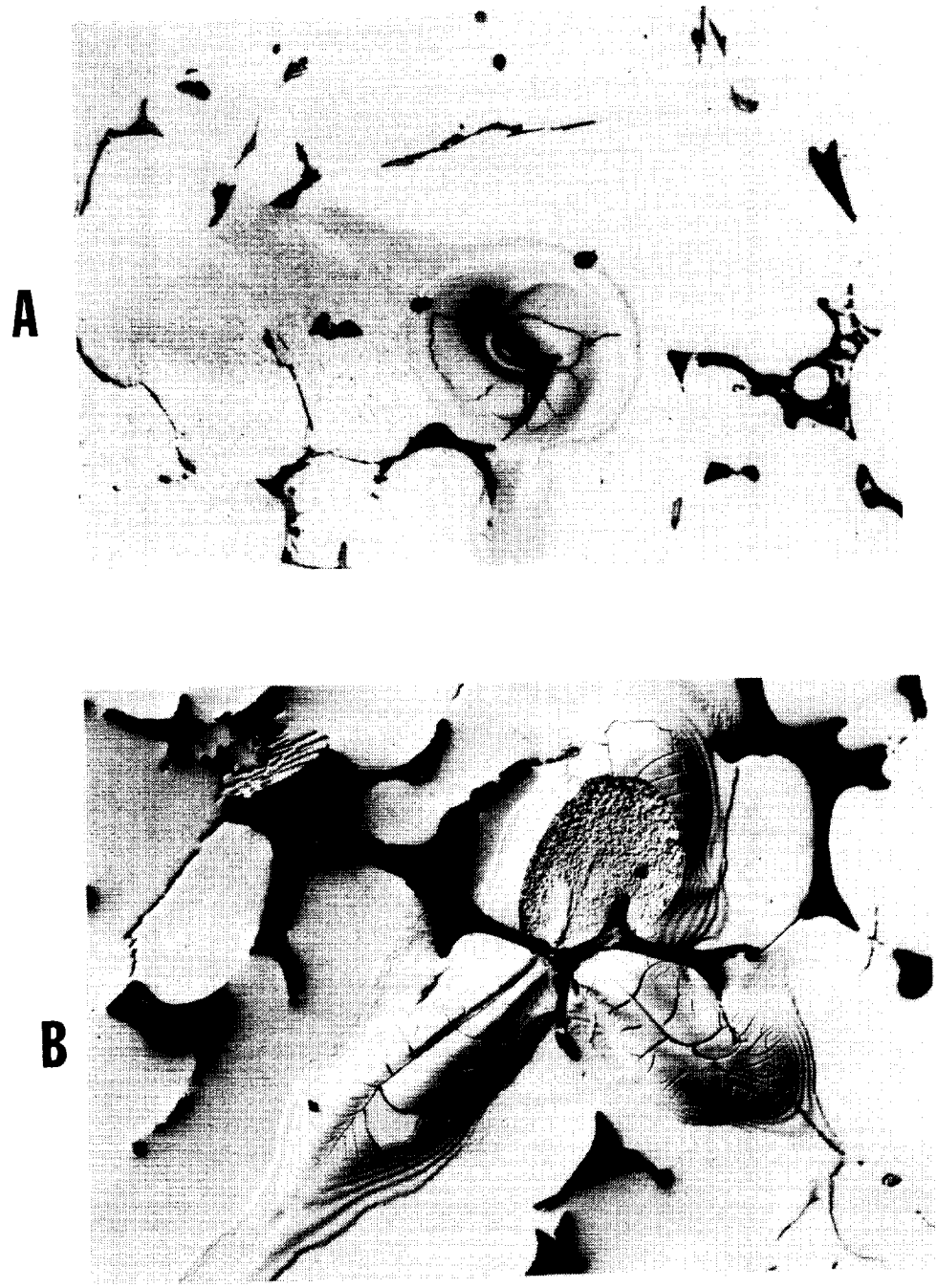

Figure 6.8 (a-d) Micrographs of an Al-Li alloy illustrating the presence of solidification cracking, dendrite tip fracture, interdendritic porosity, and coring.

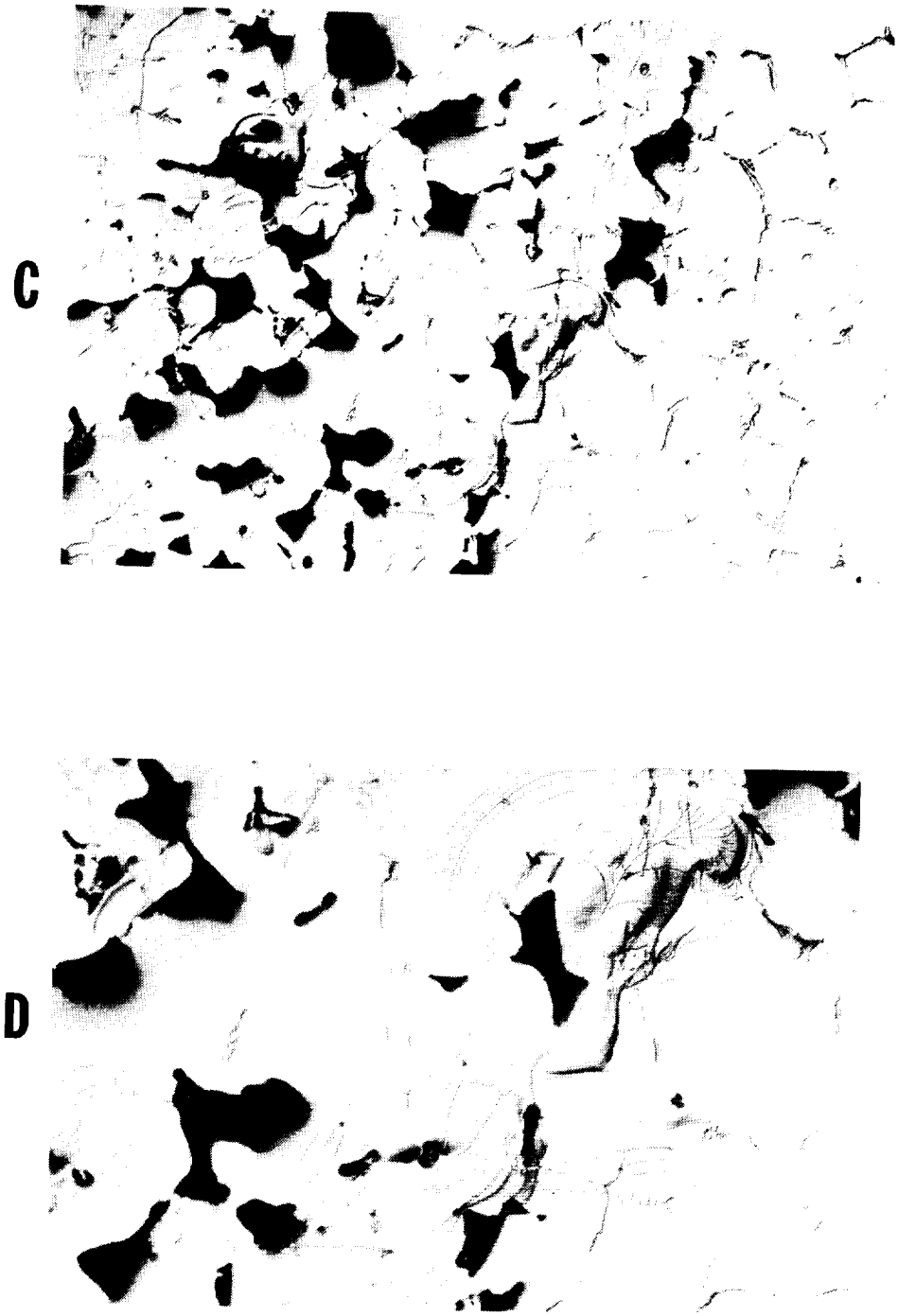

Figure 6.8 Continued.

6.3 Aluminum Copper Alloy

The porosity content of the Al-Cu alloy (Figure 6.9) can be seen to be lower than that of the Al-Li alloy (Figure 6.3). Its character may be considered to be a mixture of mostly intergranular porosity with a small amount of interdendritic porosity. The grain structure is equiaxed with the secondary phase, assumed to be θ based on the 4.7 wt% copper concentration and reference to the Al-Cu phase diagram, being concentrated primarily at the grain boundaries. This type of microstructure was common for all of the casting specimens with some variations in the degree of porosity. The microstructure was not as closely examined for microcracking as was the Al-Li alloy, however, during the study of other features such as grain size, none was observed.

In conclusion, the microstructural analysis of the Al-Cu alloy supports the results of the acoustic emission experiments for this material. There was some interdendritic porosity present that would be responsible for the period of AE activity at the beginning of solidification. The amount of porosity was lower in the Al-Cu alloy than in the Al-Li alloy and, correspondingly, the number of AE events in the first period was lower for the Al-Cu alloy than for the Al-Li alloy. The micro-cracking, if present at all, was lower in the Al-Cu alloy than in the Al-Li alloy and the number of AE events in the second period was lower in the Al-Cu alloy than in the Al-Li alloy. The AE events that were present in the second period are attributed more to dislocation motion during grain boundary formation, as in the UHP aluminum, than to dendrite tip fracture or solidification cracking.

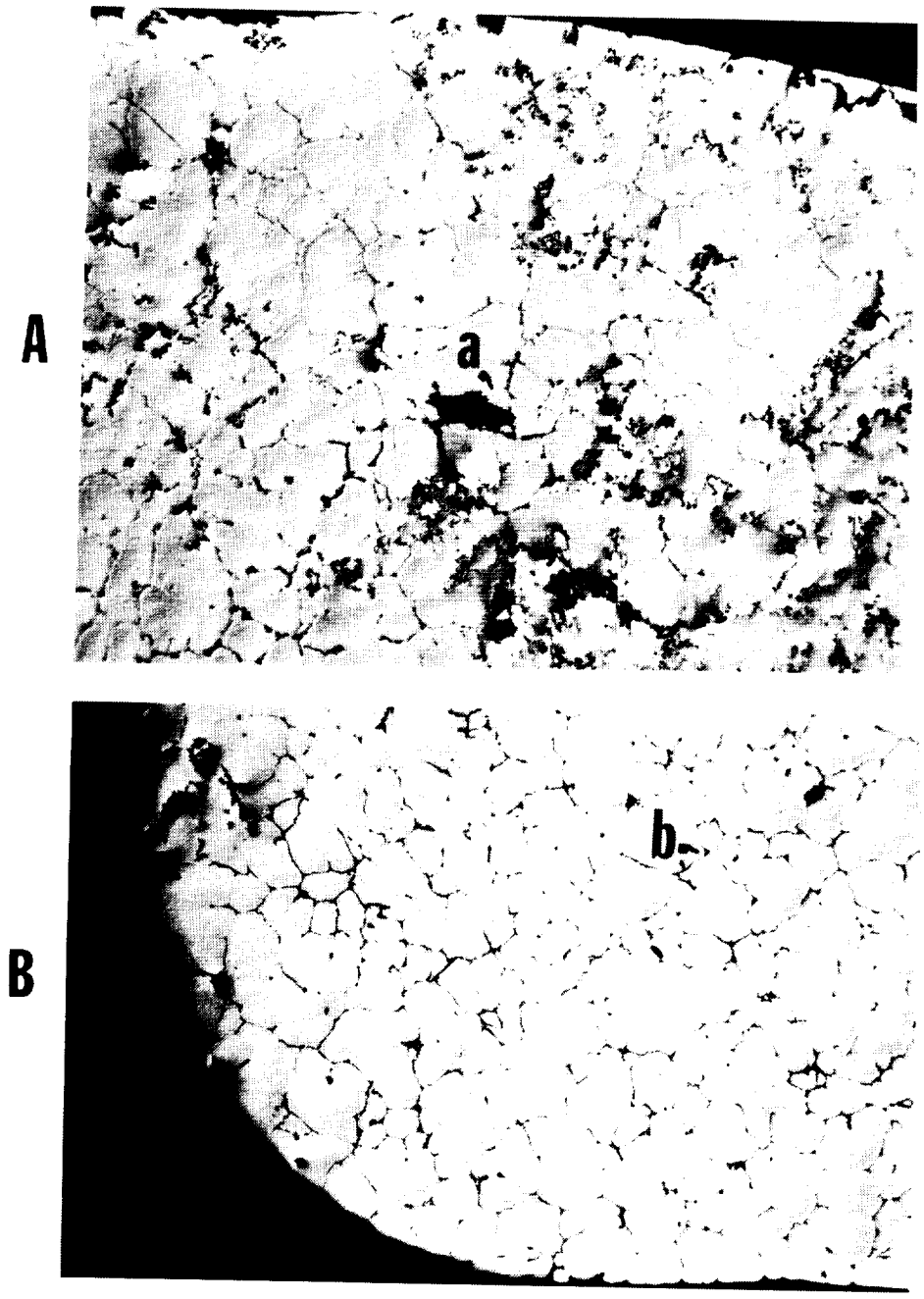

Figure 6.9 Microstructure of the (a) top and (b) bottom of an Al-Cu alloy casting illustrating (A) intergranular porosity and an equiaxed grain structure with (B) the θ phase segregated at the grain boundaries (both Keller's Reagent, 32x).

VII. CONCLUSIONS

In the first part of this work, the influence of the components of the experimental system on known acoustic emission waveforms and their associated frequency spectra was examined. These experimental elements specifically include the transducer, the waveguide, and noise. The major conclusions that can be drawn from observations of these experiments are as follows:

1. When an acoustic emission signal is generated by a solidifying aluminum alloy, the waveform is predominantly changed by the resonant characteristics of the waveguide which couples the crucible to the transducer. If these low frequency resonant components are then filtered out, the transfer function of the transducer dominates the output signal and prevents analysis of the AE source waveform.

2. The average longitudinal and shear mode wave velocities for the amorphous boron nitride waveguide were determined to be 4,600 and 2,760 m/s, respectively. From this, the resonant frequency for a waveguide of given geometry can be calculated and compared to experimental frequency spectra. The response of this material, in rod form, to either a pulse or single sine wave input is a severely attenuated ringing waveform. The boron nitride provided a good compromise between insulating the transducer from furnace heat and transmitting the AE signals to the transducer.

3. Electronic and vibrational noise from each component of the experimental system was characterized to establish a minimum signal threshold that would accept acoustic emission from solidifying aluminum alloys and filter out random signals. It was

necessary to set the total system gain to 90 dB for reliable detection of acoustic emission during solidification.

In the second part of this work conventional AE and individual waveform analyses were used to monitor the solidification of aluminum and two of its alloys. The major conclusions from this part of the work include:

1. Ultra-pure aluminum generated detectable acoustic emission during solidification as the final 10% fraction of solid formed. Several sources of acoustic emission have been discounted but a model was presented which attributes the AE activity to internal stress developed during grain boundary formation.

2. The commercial grade AA2090 aluminum-lithium alloy generated two periods of high acoustic emission activity during solidification. The first occurred at the beginning of solidification ($f_S < 0.2$) and was attributed to interdendritic porosity; the second occurred at the end ($f_S > 0.9$) and a model similar to UHP aluminum ascribed the source to be internal stress from grain boundary formation.

3. A binary Al-4.7wt%Cu alloy generated an AE activity pattern similar to the AA2090 alloy: two periods, at the beginning and the end of solidification, respectively. The low number of AE events in the first period was considered a result of less interdendritic porosity and the low number of events in the second period was considered a result of less microcracking than in the lithium-containing alloy.

4. A crucible material such as alumina, which adheres to the solidifying aluminum alloy, was determined to cause high acoustic emission activity after the specimen had

solidified. A non-wetting crucible material such as boron nitride, which does not adhere to the specimen, did not cause this type AE behavior. Instead, the AE activity after solidification was low and was considered a result of continued grain boundary realignment and micro-cracking as the specimen cooled.

5. Individual waveform analysis in both the time and frequency domains was unable to distinguish acoustic emission signals at the beginning from those at the end of solidification in the Al-Li and the Al-Cu alloys. The frequency spectra obtained demonstrated the influence of the transducer and waveguide transfer functions but produced no distinguishing characteristics for the waveform of the AE source. AE signals were only detected at the end of solidification for the ultra-pure aluminum.

VIII. SUGGESTIONS FOR FUTURE WORK

Although it is time to consider the present study complete, there remain many unanswered questions regarding acoustic emission during solidification of aluminum alloys. Therefore, in the interest of continued research, the following suggestions are given to provide some direction to those interested in pursuing the subject.

Towards the end of the program hot stage microscopy was used as an analytical tool, however, since the results were preparatory in nature, the methods will simply be presented here with suggestions for future work. The AE conditioning circuit described in Section 3.3, Data Acquisition, was integrated into a hot stage microscope system (Figure 7.1). A 2 mm diameter stainless steel rod was coupled to the microscope stage which consisted of an alumina crucible in an argon atmospheric chamber. The other end of the rod was joined to a VP-1093 pinducer which was then connected to a preamplifier, a main amplifier, and an oscilloscope. A 2x5 mm disk of pure aluminum with a polished mirror-finish face was placed in the stage, melted and solidified. During solidification, acoustic emission signals were observed on the oscilloscope and grain formation was simultaneously seen in the form of microscopic surface relief. A similar result was achieved with the aluminum-copper alloy. In addition the eutectic phase formation was also observed. Although the initial results were encouraging, there were problems with oxidation and maintaining focus. It is suggested, therefore, that further hot stage microscopy work be done in conjunction with acoustic emission using materials that do not require controlled atmospheres.

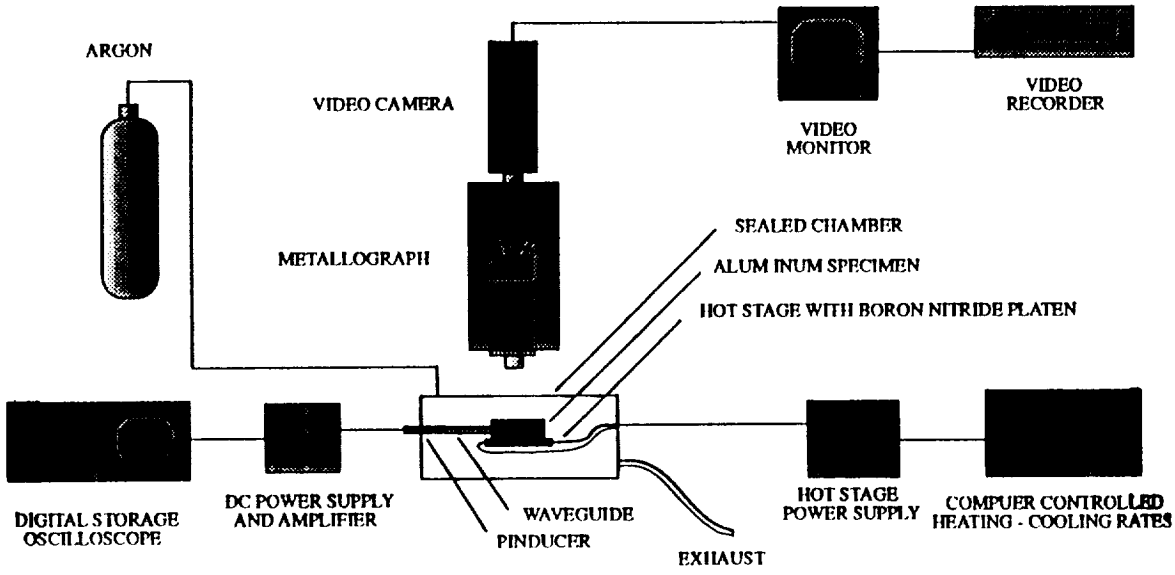

Figure 7.1 Hot stage microscopy system with acoustic emission monitoring capabilities.

A similar technique could be done using differential scanning calorimetry in place of the hot stage microscopy. By coupling the transducer to the stage and using conventional AE analysis, a record could be made of AE activity as a function of evolved heat rather than temperature. Since both AE and heat are forms of energy released during solidification, a very interesting and direct relationship would be expected between the two.

Directional solidification could also provide insight into sources of acoustic emission since the solid-liquid interface could be changed from dendritic to cellular or planar. The

interdendritic porosity attributed to be the source of acoustic emission during the beginning of solidification in the Al-Li-Cu alloy could be eliminated. It would then be expected that the AE activity would also be eliminated. Additionally, directional solidification could be used to examine the effect of cooling rate on the AE activity since the rate can be closely controlled with this method.

References

1. T.F. Droulliard, "Anecdotal History of Acoustic Emission From Wood," J. of AE, **9(3)** (1990) pp. 155-176.

2. J. Czochralski, "Die Metallographie des Zinns und die Theorie der Formanerung bildsamer Metalle (The Metallography of Tin and the Theory of Deformation of Soft Metals)," Metall und Erz, (in German), XIII(N.F.IV), **18** (September 22, 1916) pp 381-393.

3. F. Forster and E. Schiel, "Acoustic Study of the Formation of Martensite Needles," Zeitschrift fur Metallkunde, **28 (9)** (September 1936) pp. 245-247.

4. J. Kaiser, "An Investigation into the Ocuurance of Noises in Tensile Tests or a Study of Acoustic Noises in Tensile Tests," UCRL-Trans-1082(L), English translation of Kaiser's Ph.D. dissertation, (1950), for Lawrence Radiation Laboratory, Livermore, CA, (June 1964).

5. H. Borshers and J. Kaiser, Zeitschrift fur Metallkunde, **49** (1958) p. 95.

6. R.G Liptai, "An Investigation of the Acoustic Emission Phenomenon," Michigan State Univ., Ph.D. Thesis, 1963, p2.

7. Y.H. Pao, "Theory of Acoustic Emission," Elastic Waves and Nondestructive Testing of Materials, ASME AMD-20, New York, N.Y., American Society of Mechanical Materials, (1978) pp. 107-128.

8. N.N. Hsu, J.A. Simmons and S.C. Hardy, "An Approach to Acoustic Emission Signal Analysis- Theory and Experiment," Materials Evaluation, **35 (10)**, Columbus, OH: The American Society for Nondestructive Testing, (1977) pp. 100-106.

9. H.L. Dunegan and D.O. Harris, "Acoustic Emission Techniques," Experimental Techniques in Fracture Mechanics, ed. A.S. Kobayashi, Iowa State University Press, (1973) p 39.

10. D. Egle, "A Comprehensive Analysis of an Acoustic Emission System, Ph.D. Thesis, New Orleans, LA, Tulane University (1965).

11. T.F. Droulliard, Acoustic Emission: A Bibliography with Abstracts, ed. F.J. Laner, IFI/Plenum Data Company, New York, (1979).

12. R.K. Miller and P. McIntire, editors, Acoustic Emission Testing-Nondestructive Testing Handbook Vol.5, 2nd Ed., (ASNT, Inc., 1987).

13. U. Feurer and R. Wunderlin, "Observation of Porosity Formation During Solidification of Aluminum Alloys by Acoustic Emission Measurements," [Proc. Conf.] Solidification and Casting of Metals, Sheffield, England, 1977, The Metals Society, London (1979) p340.

14. T.S. Kumar and O. Prabhakar, "Acoustic Emission During Solidification of Aluminum Alloys," AFS Transactions, Volume 93 (April 1985) pp 13-22.

15. D.G.R. Sharma, O. Prabhakar, and H.Md. Roshan, "Detection of Hot Tearing in Aluminum Alloys by Acoustic Emission Techniques," Aluminum, **59** (1983) pp 917-920.

16. B. Xiufang, C. Baohua and L. Musen, "Solidification and Acoustic Emission," Cast Metals, **2 (2)** (1989), pp. 103-109.

17. H.L. Dunegan, "Progress in Acoustic Emission II," Proc. of the 7th International Acoustic Emission Symposium, Tokyo, Japan, Japanese Society of Nondestructive Inspection, (1984) pp. 294-301.

18. I.G. Palmer and P.T. Heald, "The Application of Acoustic Emission to Fracture Mechanics," Materials Science and Engineering, **11 (4)** (1973) pp 181-184.

19. T.W. Rettig and M.J. Felsen, "Acoustic Emission Method for Monitoring Corrosion Reactions," Corrosion, **32 (4)** (1976) pp 121-126.

20. Y. Blanchette, J.I. Dickson and M.N. Bassim, "Detection of General Yielding in A516 Steel by Acoustic Emission," Engineering Fracture Mechanics, **17** (1982) p 227.

21. H.P. Bloch, "Machinery Monitoring with High Frequency Acoustic Emission Measurements," Hydrocarbon Processing, (May 1977).

22. H.R. Hardy, "Applications of Acoustic Emission Techniques to Rock and Rock Structures: A State-of-the -Art Review," Acoustic Emissions in Geotechnical Engineering Practice, ASTM STP 750, Philadelphia, PA, American Society for Testing and Materials, (1981) pp 4-92.

23. T.J. Fowler, " Acoustic Emission Monitoring of Chemical Process Industry Vessels," Proc. of the 7th Intl. Symposium on Acoustic Emission, Sendai, Japan (1984).

24. C.B. Scruby, C. Jones, J.M. Titchmarch, and H.N.G. Wadley, Metall. Sci. **15 241** (1981).

25. P.P. Gillis and M.A. Hamstead, Materials Science & Engineering, **14** (1974) pp 103-108.

26. M. Ohtsu and K. Ono, "A Generalized Theory of Acoustic Emission and Green's Function in a Half Space," Journal of Acoustic Emission, **3 (1)** (1985) pp 27-40.

27. D.O. Harris and R. Bell, " The Measurement and Significance of Energy in Acoustic Emission Testing," Experimental Mechanics, **17 (9)** (1977) pp 347-353.

28. C.B. Scruby, J.C. Collingwood, and H.N.G. Wadley, J. Phys. D **11** (1978) p. 3.

29. "ASYSTANT- GPIB," waveform processing software, ASYST Software Company, New York, N.Y., (1989).

30. C.B. Scruby, J.C. Collingwood, and H.N.G. Wadley, J. Phys. D **11** (1978) p 2359.

31. H.N.G. Wadley, C.B. Scruby and J.H. Speake, Int. Metals Reviews, **2** (1980).

32. B.H. Schofield, R.A. Barress and A.A. Kyrola, " Acoustic Emission Under Applied Stress," WADC Technical Report 58-194, ASTIA Document # AD 155674, 1958.

33. R.J. Kroll, "Stress Waves in Test Specimens Due to Simulated AE," Ph.D. Thesis, College of Engineering, Michigan State, 1962.

34. F. Fleischmann, D. Rouby, F. Lakestani and J.C. Baboux, "A Spectrum Analysis of Acoustic Emission," Non-Destructive Testing, **8** (Oct. 1975) pp 241-244.

35. L.J. Graham and G.A. Ahlers, " Spectrum Analysis of Acoustic Emission in A533-B Steel," Materials Evaluation, **32 (2)** Columbus, OH, The Society for nondestructive Testing (1974) pp 34-37.

36. T. Kishi, "Acoustic Emission Source Characterization and Its Application to Microcracking," Zeitschrift fur Metallkunde, pp. 512-518.

37. J.M. Park and H.C. Kim, "The Effects of Attenuation and Dispersion on the Waveform Analysis of Acoustic Emission," Mat. Eval. (May 1989) pp. 617-622.

38. R.A. Kline and S.S. Ali, "Methods of Calculating Attenuation and Dispersion Effects on Acoustic Emission Signals," J. of AE, **4(4)** (1985) pp. 107-114.

39. M. Ohtsu, "Source Kinematics of Acoustic Emission Based on a Moment Tensor," NDT Intl., **22 (1)** (February 1989) pp. 14-20.

40. Z. Yu and P.C. Clapp, "Quantitative Analysis of Acoustic Emission Signals," J. Appl. Phys., **62 (6)** (September 15, 1987) pp. 2212-2220.

41. T. Sato and T. Hirasawa, "Body Wave Spectra from Propagating Shear Cracks," J. Phys. Earth, **21** (1973) pp 415-431.

42. J.C. Savage, "Radiation from a Realistic Model of Faulting," Bull. Seism. Soc. Am., **56** (1966) pp. 577-592.

43. A.Md. Altaee, "Enhancement of AE Signals by Homomorphic Filtering," Ph.D. Dissertation, Univ. of Manitoba, Canada, (1985).

44. T.P. Harrington and P.G. Doctor, "Acoustic Emission Analysis Using Pattern Recognition," Proc. of the Fifth Joint Conference on Pattern Recognition, (December 1980) pp. 1204-1207.

45. Y. Miyata, T. Suzuki and J-I Uno, "Cellular and Dendritic Growth Part I: Experiment," Met. Trans. A, **16A** (October 1985) pp 1799-1814.

46. M.C. Flemings, " The Solidification of Castings," Scientific American, (1974) pp 88-95.

47. M.C. Flemings, Solidification Processing, (McGraw-Hill, NY, NY, 1974) pp 31-32.

48. R.E. Reed-Hill, Physical Metallurgy Principles, 2nd Ed., Brooks/Cole Enginnering Division, Monterey, CA, (1973).

49. S.E. Kisakurek, "An Experimental Investigation into the Formation of an Equi-axed Zone into Ingot Casting: Pb-Sb Alloy System," J. of Mat. Sci., (1984) pp 2289-2305.

50. D.P. Hill and D.N. Williams, "Relationship between Hydrogen Content and Low Ductility of Aluminum-Lithium Alloys," Battelle Columbus Contract N00019-81-C-0433 (October 19,1982).

51. D.P. Hill and D.N. Williams, "A Literature Survey of the Ductility and Fracture Toughness of High Modulus Low Density Al-Li-X Alloys," Intl. Report of the Battelle Lab. (September 10, 1980).

52. P.N. Analebechi, D.E.J. Talbot and D.A. Granger, "The Solubility of Hydrogen in Liquid Binary Al-Li Alloys," Met.Trans. B, **19B** (April 1988) pp 227-232.

53. C.E. Ransley and H. Neufeld, "The Solubility of Hydrogen in Liquid and Solid Aluminum," J. Inst. of Met., **74** (1947/1948) pp.599-620.

54. L.W. Eastwood, Gases in Non-Ferrous Metals and Alloys, (ASM Publications, Metals Park, OH, 1953).

55. J. E. Hatch, Aluminum Properties and Physical Metallurgy, (ASM Publications, Metals Park, OH, 1984) p 17.

56. G.J. Metcalfe, J. Inst. of Met., **71** (1945) p. 618.

57. R.A. Entwistle, J.E. Gruzleski and P.M. Thomas, "Development of Porosity in Al-Based Alloys," Solidification Processing, McGraw-Hill, NY, NY (1974) pp. 345-349.

58. E.W. Lee, C.E. New, and J. Kozol, "Al-Li Alloys and Ultra-High Strength Steels for U.S. Navy Aircraft, J. of Metals, (May 1990) pp 11-14.

59. J. Wadsworth, A. Joshi and A.E. Vidoz, "Microstructural Evaluation of Arc-Melted Al-Li-Be Alloys, "J. of Mat. Sci., **21** (1986) pp. 3843-3849.

60. J.R. Pickens, "Review: The Weldability of Lithium-Containing Aluminum Alloys," J. of Mat. Sci., **20** (1985) pp. 4247-4258.

61. D. Webster and C.G. Bennett, "Tough(er) Al-Li Alloys," Adv. Mat. and Procs., (October 1989) pp 49-54.

62. E.J. Lavernia and N.J. Grant, "Review: Aluminum-Lithium Alloys," J. of Mat. Sci., **22** (1987) pp 1521-1529.

63. D.P. Hill and D.N. Williams, Aluminum-Lithium III, [Conf. Proc.], (AIME Publ., N.Y., 1983) pp 201-218.

64. E.A. Starke , Jr., T.H. Sanders and I.G. Palmer, " New Approaches to Alloy Development In the Al-Li System, Aluminum-Lithium III [Conf. Proc.], AIME Publ., NY, NY (1983).

65. H.M. Flower and P.J. Gregson, "Solid State Phase Transformations in Aluminum Alloys Containing Lithium," Mat. Sci. and Tech, **3** (February 1987) pp 81-90.

66. P. Sainfort and P. Guyot, "Fundamental Aspects of Hardening in Al-Li and Al-Li-Cu Alloys," Aluminum-Lithium II, pp 420-426.

67. F.W. Gayle and B. Vandersande, "Phase Transformations in the Al-Li-Zr System," Acta Metall., **37 (4)** (1989) pp. 1033-1046.

68. ASYSTANT-GPIB software program, Asyst Software Technologies, Inc., N.Y., N.Y., (1989).

69. Y. Higo and H. Inaba, "The General Problems of AE Sensors," J. of AE, **8 (1&2)** (Jan.-Jun. 1989) pp. 25-26.

70. "Nondestructive Testing: ASTM E1106- Primary Calibration of Acoustic Emission Sensors," Annual Book of ASTM Standards, Section 3, Volume 03.03, Philadelphia, PA, American Society for Testing and Materials (1987).

71. Y.H. Pao, R. Gajewski and A. Ceranoglu, "AE and Transient Waves in an Elastic Plate," J. Acoust. Soc. Am., **65** pp 96-105.

72. W. Prosser, "The Propagation of Extensional and Flexural Mode Plate Waves in Aluminum and Graphite/Epoxy Plates," Ph.D. Dissertation, Johns Hopkins University, (1991).

73. "Nondestructive Testing: ASTM E976- Guide for Determining the Reproducibility of Acoustic Emission Sensor Response," 78. W. Oldfield, ASM Trans., **59** (1966) pp. 945-959.

74. P. Thevoz, S. Desbiole and M. Rappaz, Met. Trans A, **20A** (1989) pp. 311-322.

75. D. Stephanescu, G. Upadhya and D. Bandyopadhyay, "Heat Transfer - Solidification Kinetics Modelling of Solidification of Castings," Met. Trans. A, **21A** (April 1990) pp. 997-1005.

76. D.G. Eitzen and H.N.G. Wadley, "AE: Establishing the Fundamentals," J. of Research NBS, Vol. 89, No. 1, (Jan-Feb 1984) pp 75-100.

REPORT DOCUMENTATION PAGE

Form Approved
OMB No. 0704-0188

1. AGENCY USE ONLY (Leave blank)	2. REPORT DATE	3. REPORT TYPE AND DATES COVERED
	April 1992	Contractor Report

4. TITLE AND SUBTITLE
A Study of Aluminum-Lithium Alloy Solidification Using Acoustic Emission Techniques

5. FUNDING NUMBERS
G NGT-50417
WU 323-51-66-01

6. AUTHOR(S)
Daniel P. Henkel

7. PERFORMING ORGANIZATION NAME(S) AND ADDRESS(ES)
Lehigh University
Bethlehem, PA 18015

8. PERFORMING ORGANIZATION REPORT NUMBER

9. SPONSORING/MONITORING AGENCY NAME(S) AND ADDRESS(ES)
National Aeronautics and Space Administration
Langley Research Center
Hampton, VA 23665-5225

10. SPONSORING/MONITORING AGENCY REPORT NUMBER
NASA CR-4437

11. SUPPLEMENTARY NOTES
Langley Technical Monitor: John H. Cantrell, Jr.
Thesis submitted to Lehigh University in partial fulfillment of the degree of doctor of philosophy, October 1991.

12a. DISTRIBUTION/AVAILABILITY STATEMENT
Unclassified - Unlimited
Subject Category 70

12b. DISTRIBUTION CODE

13. ABSTRACT (Maximum 200 words)

Physical phenomena associated with the solidification of an aluminum-lithium alloy has been characterized using acoustic emission(AE) techniques.This study has shown that repeatable patterns of AE activity may be correlated to microstructural changes that occur during solidification.The influence of the experimental system on generated signals has been examined in the time and frequency domains.The analysis was used to show how an AE signalfrom solidifying aluminum is changed by each component in the detection system to produce a complex waveform. Conventional AE analysis has shown that a period of high AE activity occurs in pure aluminum, an Al-Cu alloy, and the Al-Li alloy as the last fraction of solid forms.A model attributes this to the internal stresses of grain boundary formation.An additional period of activity occurs as the last fraction of solid forms, but only in the two alloys. A model attributes this to the formation of interdendritic porosity which was not present in the pure aluminum.The AE waveforms were dominated by resonant effects of the waveguide and the transducer.

14. SUBJECT TERMS
Acoustic emission; aluminum-lithium alloys; solidification; casting porosity

15. NUMBER OF PAGES
208

16. PRICE CODE
A10

17. SECURITY CLASSIFICATION OF REPORT	18. SECURITY CLASSIFICATION OF THIS PAGE	19. SECURITY CLASSIFICATION OF ABSTRACT	20. LIMITATION OF ABSTRACT
Unclassified	Unclassified		

NSN 7540-01-280-5500

Standard Form 298 (Rev. 2-89)
Prescribed by ANSI Std. Z39-18
298-102